MOLECULAR ORIENTATION AND DYNAMICS OF FLEXIBLE POLYMERS IN STONGLY DEFORMING FLOW FIELDS

MARIA KILFOIL

Molecular Orientation and Dynamics of Flexible Polymers in Strongly Deforming Flow Fields

by

Maria Kilfoil

M.Sc. (Memorial University of Newfoundland, St. John's, Newfoundland, Canada) 1997
B.Sc. (University of New Brunswick, Fredericton, New Brunswick, Canada) 1995

A thesis submitted to the School of Graduate
Studies in partial fulfilment of the
requirements for the degree of
Doctor of Philosophy

Department of Physics and Physical Oceanography
Memorial University of Newfoundland

(August, 2001)

Abstract

A method of spatially resolved magnetic resonance spectroscopy has been developed to allow studies of order and dynamics in complex fluids having transverse relaxation times on the order of tens of milliseconds, studies which were otherwise not possible using existing techniques. The model of Doi and Edwards is a microscopic description for stress transmission in concentrated polymer solutions and melts under deformation. Central to the Doi-Edwards model is the dependence of the stress on bond orientational order of the chain segments. Different elements of the segmental alignment tensor for a polymer melt under strong shearing flow are measured here using localized deuterium NMR spectroscopy on a 610K molecular weight poly(dimethyl siloxane) melt in a concentric cylinder Couette rheometric cell. This approach provides a new means of testing the Doi-Edwards model and its refinements, in the important regime far from equilibrium where the entangled polymers exhibit nonlinear viscoelastic behaviour.

The same rheo-NMR methodology is also used to test predictions of the model of Leslie and Ericksen which describes director dynamics in semi-flexible rod-like polymers subjected to viscous stresses. Director dynamics are studied in a lyotropic liquid crystal polymer PBLG (300K) in a highly ordered, nematic phase in a planar extensional flow around a stagnation point. In addition, bulk ^{2}H NMR studies are carried out on PBLG under shear, in concentric cylinder Couette and cone and plate rheometric cells. Magnetic alignment (equivalent to the dynamic Fréedericksz transition) is investigated in all three cells following deformation. Values are obtained for the Leslie viscosity coefficients α_2 and α_3, scaled by the diamagnetic susceptibility. Possible development of mesoscale structure under shear is discussed.

Contents

List of Tables

List of Figures

---

1 Introduction: Viscoelastic fluids

Magnetic resonance imaging and spectroscopy can be combined with rheometric techniques as a sensitive probe of molecular organization of complex fluids in flows. In this dissertation the combination is used for testing microstructural theories of polymer melts in strong shearing flows and liquid crystal polymers in extensional flows around stagnation points. In both cases the complex fluids exhibit nonlinear behaviour far from equilibrium.

Solutions of entangled, flexible polymers and undiluted polymer melts are viscoelastic. Their sometimes solid-like character usually results in very short relaxation times and consequently very short NMR observation times, severely limiting the use of conventional volume-selective NMR spectroscopy. The NMR studies presented here of deformation and reorientation of polymer chains at well-defined sites within shearing and extensional flow fields were made possible by development of a novel method for spatially selective spectroscopy which is sensitive to weak ordering effects and which is robust under very short relaxation conditions.

Viscoelastic fluids, as the name suggests, exhibit both viscous (leading to energy dissipation) and elastic (corresponding to storage of energy) properties. The elastic nature of polymeric liquids derives from the tendency of the molecules to recover their equilibrium, isotropic distribution of bond vectors following a perturbation. The viscous component arises from the presence of other (polymer or solvent) molecules which delays the reorientation process [1]. "Normal" liquids have purely viscous behaviour and follow Newton's law of viscosity whereby the stress is proportional to the rate of deformation. The constant of proportionality is the viscosity η. In viscoelastic liquids the viscosity is not constant but itself depends on the deformation rate. Polymeric liquids usually have a viscosity which decreases with increasing shear rate, giving rise to so-called shear-thinning behaviour. Figure 1.1 shows an example of shear thinning in a polymer melt. In general the stress in polymers has a nonlinear dependence on velocity gradients, which under large deformations often results in unusual macroscopic flow phenomena, or a high degree of orientation of the polymer chains. The large normal stresses generated in entangled flexible polymers, and exceptional tensile strength and extensional viscosity in oriented fibers shown in figure 1.2, are examples of such effects. Study of the molecular basis for these behaviours is motivated

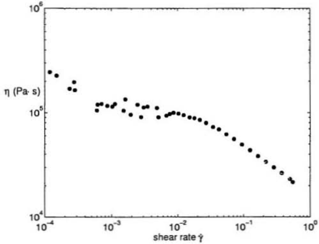

Figure 1.1: Representative flow curve, for 680K poly(dimethyl siloxane). The approximately constant viscosity at low shear rates (small deformations) but decreasing viscosity with shear rate at larger deformations is typical of polymeric liquids.

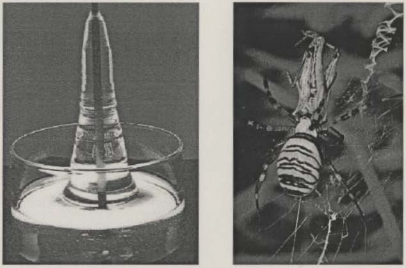

Figure 1.2: *At left,* a polyisobutane solution demonstrates rod-climbing, or the Weissenburg effect, due to normal stress generated by rotating the rod in the polymeric liquid (reproduced with permission from [1]). Large normal stresses are examples of nonlinear effects which occur in non-Newtonian liquids, and are particularly important in processing as they can affect quite dramatically the final mechanical properties of materials containing polymeric liquids. *At right,* a spider produces dragline silk, a biopolymer which is five times stronger than steel and can stretch up to 30% longer than its original length. The nonlinear dependence of stress on strain in this remarkable material allows the spider to support its own weight and capture insects without the silk breaking.

in part by the wish to predict molecular organization and reorganization in macroscopic flows during processing and by the drive for new materials capitalizing on these effects. In addition, the theories and models which describe them are based on fundamental physical ideas, and opportunities to test these ideas are exciting.

1.0.1 The nature and origin of stresses

Stress is always present in liquids. In equilibrium conditions the normal stress is simply the isotropic pressure acting on a fluid element, or on a polymer chain. When one speaks of stresses in the context of rheometry it is in terms of restoring forces generated in conditions of relative flow and deformation, and the isotropic stresses are ignored [1]. The

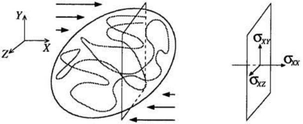

Figure 1.3: Stresses in a polymer molecule under deformation, depicted here for the case of a strong shearing flow. The components of stress on an imaginary plane normal to the velocity direction X are drawn at right.

shear stress σ_{XY} is the restoring force per unit area generated by a velocity gradient along Y on a surface perpendicular to the X-axis, while the normal stress σ_{XX} is the stress generated by a velocity gradient along X on a surface perpendicular to X[1]. For elastic liquids there is a simple relation between the stress and the velocity gradients,

$$\sigma_{\alpha\beta} = \eta\,(\boldsymbol{\kappa})\;(\kappa_{\alpha\beta} + \kappa_{\beta\alpha})$$

where $\boldsymbol{\kappa} = \nabla\vec{v}$ is the rate of strain or velocity gradient tensor

$$\kappa_{\alpha\beta} = \frac{\partial v_\alpha}{\partial\beta}, \quad \alpha, \beta = X, Y, Z \tag{1.1}$$

and the viscosity also depends on the velocity gradients. For example, for simple shear, $\boldsymbol{\kappa}$ reduces to the shear rate $\kappa_{XY} = \dot{\gamma}$ and the stress is simply the shear stress $\sigma_{XY} = \eta(\dot{\gamma})\,\dot{\gamma}$. For polymeric liquids and other viscoelastic fluids the stress will be a nonlinear function of the velocity gradients. Mathematical expressions for stress for different classes of fluids are developed either from phenomenological models or from theories based on the fluid microstructure. Expressions for stress are important because they contain in full the dependence of the stress on the velocity gradients for arbitrary flows.

---

[1] Here and throughout this dissertation, X, Y, Z are the hydrodynamic velocity, gradient and vorticity axes, as distinguished from laboratory frame coordinates x, y, z.

Under small amplitude perturbations the normal stresses are negligible. The origin of unequal normal stresses in polymeric liquids under larger amplitude deformations can be understood in the following way: deformation of the average shape of a polymer molecule (its envelope) is anisotropic, and so the restoring forces generated are anisotropic as well. In this case we expect the normal stresses to be unequal. In addition the off-diagonal elements of the stress tensor (the shear stresses) may also be non-zero, depending on the geometry of the deformation. In shear or extension one expects to find the largest component of the stress (corresponding to the largest restoring force generated) to be σ_{XX}, the component in the direction of the flow, unless some unusual microstructure is present. The first normal stress difference $N_1 = \sigma_{XX} - \sigma_{YY}$ and the second normal stress difference $N_2 = \sigma_{YY} - \sigma_{ZZ}$ are non-zero when nonlinear terms in the velocity gradients become important. As a result, non-zero normal stress differences are signatures of nonlinear viscoelastic behaviour.

1.1 Linear viscoelasticity

Polymer fluid dynamicists have developed appropriate ways to measure deformation under imposed stress; these studies are known collectively as *rheometry*. The relative importance of the viscous and elastic tendencies in the linear regime is measured by applying an oscillatory deformation of varying frequency and very small amplitude so as not to drive the molecules far from equilibrium. A time-dependent shear rate $\dot{\gamma}(t) = \dot{\gamma}\cos(\omega t)$ is applied, and the frequency response of the shear stress is measured in terms of the complex modulus $G^*(\omega)$. The real part $G'(\omega)$ and the imaginary part $G''(\omega)$, the storage and loss moduli, are measured over a wide range of frequency. Several orders of magnitude of time-scale of dynamical behaviour can be probed in this way.

These dynamic measurements are very useful in the linear regime, under equilibrium conditions and in dilute solutions where the polymer chains are not entangled and the perturbation under shear is small. The same principle has been applied recently to microrheological measurements of G' and G'' where Brownian motion of the molecules themselves provides the deformation, and this method has been used to uncover complex dynamics in biopolymers including DNA [2] and actin [3]. However, there is no immediate correlation between the linear viscoelasticity and the important nonlinear response which matters in most polymer processing situations. The nonlinear regime is not limited to synthetic processing: many naturally-occuring deformations involve nonequilibrium conditions and are of sufficient amplitude to cause microstructural rearrangement and a high degree of alignment. The spider producing silk is a prime example.

There are various models which have been successful in describing linear viscoelasticity in non-Newtonian fluids. These are discussed in many texts on the subject [1, 4]. Early molecular-based viscoelastic models for polymers treat the chains as beads connected by springs, with the viscoelasticity modeled by elastic force in the springs and viscous Stokes drag acting on the beads [5]. In the dumbbell model the polymer chain is approximated by two beads connected by a single spring. The dumbbell model successfully captures shear thinning behaviour in dilute polymer solutions and does predict molecular reorientation under large deformation in the form of a coil stretch transition at a critical shear rate, but like other simple molecular models has severe limitations which became apparent as rheometric experiments have become more sensitive, particularly to small but non-zero normal stress differences.

To uncover the complex nonlinear behaviour, tests on systems driven far from equilibrium must be carried out and the results interpreted in terms of a model for nonlinear viscoelastic behaviour which captures the essential physics.

1.2 Molecular models for nonlinear viscoelasticity

The emphasis in this thesis will be on two molecular based theories [6, 7]. The theory of Doi and Edwards [6] captures many of the nonlinear rheological properties of entangled flexible polymers in strong shearing flows. In their picture the lateral motions of the chains are assumed to be restricted by neighbouring chains, so that the hydrodynamic drag, Brownian motion, elastic and other forces occur mainly along the backbone direction and are grouped together into traction in the chains. In the Doi-Edwards framework there is a hierarchy of internal motions, and relaxation modes, associated with this back and forth wriggling or "reptation" within an imaginary tube. The longest relaxation time τ_d is the time for the polymer chain to completely reorient and define a new tube, and this time dominates any observation times exceeding milliseconds. The stress tensor accounts for the forces through an expression for bond orientational order calculated over the deformation history, and for relaxation through a relaxation function suitable for diffusion within the tube. Ultimately the elements of the Doi-Edwards stress tensor describe how forces are transmitted and how energy is redistributed in the molecules. The Doi-Edwards model is still being improved. In one refinement to the model [8], convective relative motion of the chains is considered to operate simultaneously with the diffusion within the tube, removing entanglements and providing an additional relaxation mechanism available to the chains.

Less flexible, rod-like polymers may have an inherent tendency to self-organize and align spontaneously along a common direction or director $\vec{n}$, thus exhibiting characteristics of nematic liquid crystals [9]. The anisotropy is usually 2-3 orders of magnitude smaller than in more familiar partially ordered systems. There is an emerging interest in their use in display technologies, nonlinear optical devices [10, 11] and other new applications, most of which hinge on the anisotropic material properties of oriented liquid crystal polymers.

Liquid crystal polymers also exhibit nonlinear viscoelastic effects when the velocity field is strong enough to perturb the director away from its equilibrium orientation. The theory developed by Leslie and Ericksen [12, 13] describes the dynamics of rigid rod-like polymers in flows. In this model the equation of dynamic equilibrium for director orientation arises from a balance of competing magnetic and hydrodynamic torques. Though nematics do not support stresses as solids and entangled polymers do, they can transmit torques. For the nematic liquid crystal polymer we do not evaluate the stress; the magnetic resonance experiments are sensitive to director orientation and we probe director reorientation under extension and under shear.

In chapter 2 of this thesis an overview of magnetic resonance techniques and the experimental rheo-NMR hardware used in these studies will be presented. Chapter 3 discusses the specially tailored method of performing spatially localized NMR in complex fluids. The results for a polymer melt in high shear will be presented in chapter 4 and discussed in the context of the Doi-Edwards model for concentrated polymer solutions and melts. The NMR results give direct information about the Doi-Edwards stress tensor for this melt, and further are used to investigate the convected constraint release refinement to the model. The model of Leslie and Ericksen is introduced in chapter 5 and applied to experiments on a nematic liquid crystal polymer. The director dynamics are studied during and following planar extension or shear flows, to determine the Leslie viscosity coefficients which describe the behaviour of nematic liquid crystal polymers subjected to competing magnetic and hydrodynamic viscous torques.

2 Magnetic resonance and Rheo-NMR

Magnetic resonance is a relative newcomer to the field of rheological investigations, and since the first "rheo-NMR" experiments by Nakatani *et al.* [14] in 1990 it has emerged as a valuable tool in rheometry. Unlike conventional bulk rheometric techniques, magnetic resonance is sensitive to molecular length-scale effects such as segmental alignment. Its strength lies in an ability to provide molecular-scale, as opposed to bulk, information about induced and often weak alignment of complex fluids under flow. Both the proton dipolar

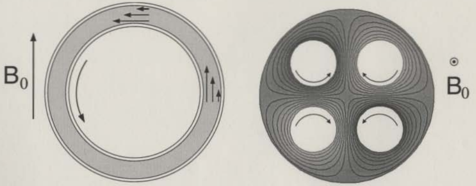

Figure 2.1: Cross-sectional views of rheometric devices. *Left:* horizontal Couette cell. *Right:* four-roll mill extensional flow cell. Shaded regions are occupied by the sample and in each case the cell is self-contained. Arrows indicate direction of mechanical driving, with fluid streamlines shown for the four-roll mill. The direction of the magnetic field, designated by B_0, with respect to the rheometric cells is indicated in the figure.

interaction and the deuterium quadrupolar interaction can provide information regarding local alignment, and since these are first order perturbations to the spin Hamiltonian, these are always projected along the polarizing field axis associated with the zeroth order Zeeman interaction. Spatially-localized NMR spectroscopy is used to measure local alignment in the two geometries shown in figure 2.1. The flow fields in these rheometric cells and the need for localized spectroscopy will be discussed in sections 2.2.1 and 2.2.2 later in this chapter.

2.1 Nuclear magnetic resonance

The fundamentals of nuclear magnetic resonance are discussed in many excellent texts on the subject [15, 16, 17, 18, 19]. A brief discussion of the NMR phenomenon and experimental NMR methods is presented here.

Elementary nuclear particles (protons, neutrons, and electrons) possess an intrinsic angular momentum, or *spin*, and associated with this, a magnetic moment. The density matrix ρ is an ensemble operator used to describe the probabilities for the quantum mechanical states of the spin system and for transitions between energy levels. The density matrix contains all of the information needed to calculate the value of any observable quantity of interest. Its evolution is determined by the Liouville equation

$$i\frac{\partial \rho}{\partial t} = [\mathcal{H}, \rho]\,,$$

where $\mathcal{H}$ is the Hamiltonian (or energy) operator.

The density operator can be expressed in a basis of single-particle angular momentum operators I_x, I_y and I_z defined with respect to the magnetic field fixed in the laboratory. In the magnetic field $\vec{B}_0$ oriented along the z-axis the Hamiltonian operator for interaction energy of the spin is

$$\mathcal{H}_z = -\mu\hbar B_0 = -\gamma\hbar B_0 I_z\,.$$

This is known as the Zeeman magnetic interaction, and determines the energy levels of the spin. For convenience, the factor of $\hbar$ is usually dropped, and the Hamiltonian written in units of angular frequency [19]. γ is the gyromagnetic ratio unique to each nucleus: for protons, $\gamma_{\mathrm{H}} = 2.675 \times 10^8\ \mathrm{T}^{-1}\mathrm{s}^{-1}$ and for deuterons $\gamma_{\mathrm{D}} = 4.11 \times 10^7\ \mathrm{T}^{-1}\mathrm{s}^{-1} \sim \gamma_{\mathrm{H}}/7$. The Zeeman interaction may be described by evolution operator $U(t) = e^{i\gamma B_0 I_z t}$ which corresponds to a (clockwise) precession of the spin about the z axis at Larmor frequency $\omega_0 = \gamma B_0$.

For spin-1/2 particles in thermal equilibrium the spins in the population may be oriented parallel to $\vec{B_0}$, corresponding to the slightly higher energy state, or antiparallel to $\vec{B_0}$, with an excess of spins oriented in the parallel, lower energy state. The population excess in the lower energy state is predicted by Boltzmann statistics, and results in a state of polarization of the spin ensemble with magnetization $\vec{M_0}$ directed along $\vec{B_0}$.

I_{x}, I_{y} and I_z are tensors. I_z contains only diagonal elements which contain information about the populations of the energy levels, and amplitude along I_z is designated longitudinal magnetization. The non-zero elements of I_{x} and I_{y} are off-diagonal, and contain the information about the phase coherence between the spin states. I_{x} and I_{y} constitute the observable, "transverse" magnetization. In thermal equilibrium there is only magnetization along I_z with no phase coherence between the spins and no observable transverse magnetization.

The phenomenon of magnetic resonance is achieved through application of a second field B_1 at a frequency $\omega = \omega_0$ for time t_{p}. The spins, being tiny magnetic moments, couple with the applied field and precess about the new transverse axis. The net magnetization is reoriented through an angle $\theta_\mathrm{p} = \gamma B_1 t_\mathrm{p}$. In the semi-classical interpretation, the net magnetization is tipped into the transverse plane. From the quantum mechanical viewpoint, there has been an evolution of the density matrix from I_z to I_x and I_y, creating observable transverse magnetization which is coherent. NMR experimentalists have developed an impressive variety of methods to manipulate spin populations, so as to report in different ways on their local environment.

Detection of the NMR signal is via a receiver antenna transverse to $\vec{B}_0$. The time domain acquisition, called the free induction decay or FID, is an interferogram of all of the signals contributing; that is, of the precessions which are superimposed on the precession at the Larmor frequency ω_0. The precession produces an emf in the coil and the signal is acquired using a receiver tuned to the Larmor frequency. The time domain signal is then Fourier transformed to yield a spectrum of frequencies centred at $\omega = \omega_0$. Most magnets currently in use for NMR are superconducting, and produce extremely stable, homogeneous static fields. Typical laboratory magnetic field strengths are in the range from 2 T to 22 T, so that the frequency of irradiation and detection $f_0 = \omega_0/2\pi$ is usually in the tens of MHz to 1 GHz range, corresponding to radio (RF) to microwave frequencies.

The RF pulse disturbs the spin system away from its equilibrium state and the system then returns to thermal equilibrium. The longitudinal magnetization is recovered as energy is given up by the spins to the lattice. T_1 is the time scale for this relaxation mechanism. Typically $T_1 \simeq$0.1 to 10 s for protons at room temperature. T_2 describes the decay of magnetization in the transverse plane, as the spins come to thermal equilibrium among themselves, by exchanging energy directly with spins as well as indirectly with the lattice. Since transverse magnetization represents a state of phase coherence, it is sensitive to terms in the spin Hamiltonian which cause the spins to dephase, and is very sensitive to slow motions. In general $T_2 < T_1$, and $T_2 \ll T_1$ for the slowly fluctuating interactions between spins which occur in solids and immobile macromolecules [19]. Phenomenologically, these relaxation processes are described by the Bloch equations which are used to predict means by which spin magnetization may be manipulated. These will be discussed in chapter 3.

2.1.1 Spin Hamiltonian

A nuclear spin communicates with its surroundings through various interactions. It is through these interactions that the spins relax. The interactions may be broadly classed as arising from external fields or from internal ones:

$$\mathcal{H} = \mathcal{H}_{\text{ext}} + \mathcal{H}_{\text{int}}$$

where $\mathcal{H}_{\text{ext}} = \mathcal{H}_0 + \mathcal{H}_1$ is the sum of the Zeeman interactions arising from external fields B_0 and B_1 and is sensitive to inhomogeneities in the external fields. The spin interactions with internal fields can be written as a sum of dipolar, quadrupolar, chemical shift anisotropy and scalar coupling interactions:

$$\mathcal{H}_{\text{int}} = \mathcal{H}_{\text{D}} + \mathcal{H}_{\text{Q}} + \mathcal{H}_{\text{CS}} + \mathcal{H}_{\text{scalar}}\,.$$

The first two terms are particularly important here as they are bilinear in the spin operator I_z. This means they are described by second rank tensors which transform under rotations as second rank spherical harmonics. They result in first-order spectra comprising two lines whose splitting is proportional to the strength of the interaction and to the direction cosines of internuclear vectors or bond angles. The splitting thus provides valuable orientation information. These terms in the spin Hamiltonian are due to dipole-dipole interactions between spins, especially strong for $I = 1/2$ spins, and the quadrupole interaction of a $I > 1/2$ spin with its electronic environment.

2.1.2 Proton dipolar interaction: ^{1}H NMR

Each nuclear spin dipole exerts a large influence on the dipole moments of remote spins through the dipolar interaction. The geometry of the interaction is shown in figure 2.2. The strength of the dipolar interaction is written

$$\mathcal{H}_{\mathrm{D}}(t) = \frac{\mu_0\gamma^2\hbar}{4\pi}\frac{1}{|\vec{r}_{12}|^3}(3\cos^2\theta_{12}(t)-1)\left[3I_{1z}I_{2z}-I^2\right], \tag{2.1}$$

for two spins separated by internuclear distance $|\vec{r}_{12}|$ (written simply as r_{12} below) and

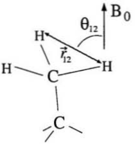

Figure 2.2: Dipole-dipole interaction between two spins whose relative positions are described by internuclear vector $\vec{r}_{12}$ and angle θ_{12} between $\vec{r}_{12}$ and $\vec{B}_0$.

angle θ_{12}. The angle $\theta_{12}(t)$ fluctuates as the segments of a polymer rotate and translate under Brownian motion. The dipolar Hamiltonian causes the spin magnetization to experience a precession $\omega_{\mathrm{D}}(t)$ and splits the proton resonance into a doublet. $(3\cos^2\theta_{12}-1)/2$ is the second Legendre polynomial $P_2(\cos\theta_{12})$ and contains the orientation information, and $\mu_0\gamma^2\hbar/(4\pi r_{12})$ is the dipolar coupling constant which defines the strength of the interaction. For protons separated by $r_{12} \simeq 1.5$Å, this corresponds to an interaction strength on the order of 100 kHz. In solids and motionally-hindered liquids having an internuclear vector which is fixed, the ^{1}H NMR lineshape is dominated by dipolar interactions.

2.1.3 Nuclear quadrupolar interaction: ^{2}H NMR

The quadrupolar interaction arises from the interaction between the nuclear quadrupole moment eQ and the surrounding electric field gradient (EFG). Figure 2.3 shows the geometry of this interaction, for a carbon-deuterium bond. For an electric field gradient which is axially symmetric, the quadrupolar interaction strength in the laboratory frame is

$$\mathcal{H}_Q(t) = \frac{eV_{zz}Q}{4I(2I-1)} P_2(\cos\theta(t)) \left[3I_z^2 - I(I+1)\right] , \tag{2.2}$$

where V_{zz} represents the principal field gradient component. As is the case for dipolar interactions, the strength of the quadrupolar interaction will be modulated by the local motions which cause $\theta(t)$ to fluctuate. The quadrupolar Hamiltonian causes the spin magnetization to experience a precession $\omega_Q(t)$ and splits the deuterium resonance into a doublet separated by

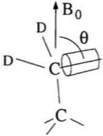

Figure 2.3: Geometry of the quadrupolar interaction arising from a static uniaxial electric field gradient tensor on a C-D bond, oriented at angle θ to the static magnetic field.

$$\Delta\nu_Q = \frac{3}{2}\frac{eV_{zz}Q}{h} P_2(\cos\theta(t)) , \tag{2.3}$$

expressed in terms of the Legendre polynomial $P_2(\cos\theta(t))$. $3eV_{zz}Q/2h$ is the quadrupolar coupling constant which defines the strength of the interaction. The spectrum will contain a doublet from each inequivalent deuteron. In protons the quadrupole moment, and hence $\mathcal{H}_Q$, is zero due to the symmetry of the nucleus. For spin $I > 1/2$ systems the quadrupolar interaction is significant and is usually the dominant interaction. Deuterium, or ^{2}H, has spin $I = 1$. The quadrupolar interaction has proven particularly useful in structural and dynamical studies of partially-ordered systems such as liquid crystals, where isotopically-labeled carbon-deuterium bonds typically yield quadrupole splittings of around 200 kHz.

The terms arising from internal fields are weak compared to the overwhelmingly larger Zeeman Hamiltonian $\mathcal{H}_z$. For this reason we often wish to suppress the unwanted Zeeman interaction, which is not a measure of anisotropy and which may otherwise mask the interesting dipolar and quadrupolar interactions arising from flow-induced anisotropy.

2.1.4 Motional averaging, and chain order via guest probe molecules

The molecular length scale accessed in NMR spectroscopy is determined by the type and strength of the interactions of the spins, and also by the degree and nature of motional averaging of the interactions experienced by the spin at its location. Let us consider the quadrupolar interaction, and the motions experienced by a deuteron located somewhere on the polymer chain. The static (before averaging) interaction strength is that arising

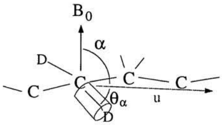

Figure 2.4: Static uniaxial EFG tensor on C-D bond projected onto the segmental axis by the local motions.

from the static uniaxial EFG tensor on a particular C-D bond. Rotation occurs about the local axis of symmetry, the local segment axis, which redefines the principal axis system of the electric field gradient. The EFG tensor is transformed to the segment axis, denoted by the local director $\vec{u}$. Figure 2.4 demonstrates this effect. The splitting of the doublet appearing in the spectrum is interpreted by decomposing the angle θ into θ_α, the angle of the C-D bond with respect to the segment axis, and α the angle between the segment axis and B_0. If θ_α fluctuates very rapidly and α very slowly compared to the strength of the interaction in the spectrum, then the spherical harmonic theorem may be used to obtain the averaged value of $P_2(\cos\theta(t))$ [16]:

$$\overline{P_2(\cos\theta(t))} = \overline{P_2(\cos\theta_\alpha(t))}\, P_2(\cos\alpha)\,.$$

Here the averaging is carried out over a time short enough that $\alpha \simeq$ constant but long on the time scale of the fluctuations of θ_α. Effectively the anisotropy is projected onto the chain backbone, the interaction strength is scaled down by $\overline{P_2(\cos\theta_\alpha(t))}$, and what remains is the residual segmental orientational order. The residual segmental order is not averaged to zero *if segmental reorientation is slow enough.* In the situations we are interested in, polymeric liquids are driven far from equilibrium and the flexible, entangled molecules experience weak, viscous stretching and elastic restoring forces such that the anisotropy is just large enough, and the segmental reorientation just slow enough to result in a non-zero residual segmental orientational order.

Use of deuterium as the NMR probe is particularly suitable for alignment studies and leads to a spectrum which is easy to interpret, however it is very difficult to isotopically label any but the simplest of molecules. It is also possible in NMR to use a simple isotopically-labeled guest probe molecule to inherit the order of the partially-ordered system of interest. If the signal is obtained from the guest probe molecule, then the issue of the size of the probe molecule, specifically its mobility, becomes important. Consider first the case of a small benzene probe molecule which is placed as a dilute species near a polymer segment whose orientation $\vec{u}$ defines the local director. The tumbling probe molecule will undergo steric interactions with that segment and experience an anisotropic mean orientation. The probe will exhibit a scaled down quadrupole splitting associated with that local site via a "pseudo-nematic" interaction [20]. This interaction is akin to the local anisotropic steric interaction experienced by small probe molecules placed in a nematic liquid crystalline environment. On average, the probe molecule samples an ensemble average value for $P_2(\cos\alpha)$ as it diffuses over the molecular dimensions. The ensemble average of $P_2(\cos\alpha)$ is equivalently written in terms of the direction cosines of the segment director $\vec{u}$: $S_{zz} = \langle \int_0^L ds\, u_z(s)\, u_z(s) - 1/3 \rangle$, averaged over the length L of the polymer chain. The quadrupole splitting may then be written

$$\Delta\nu = \left(\frac{3}{2}\frac{eV_{zz}Q}{h}\right) \overline{P_2(\cos\theta_\alpha)}\, S_{zz}\,. \tag{2.4}$$

For typical small molecules the diffusion time to cross the molecular length scale is sufficiently short to ensure that motional averaging occurs in the sampling of the distribution of $\vec{u}$ orientations. For larger guest probe molecules, the diffusion constant is smaller and the averaging incomplete: the probe samples fewer sites during the NMR experiment and does not report on the bulk average segment orientation but on a mesoscopic-length-scale average, and hence may reflect some microstructure.

2.1.5 Spin echoes

The most straightforward way to create coherence in the transverse plane is to apply a single excitation $(\pi/2)_x$ excitation pulse (recalling that $\theta_p = \gamma B_1 t$, this is a rotation of 90 degrees about the x-axis), and immediately begin acquiring the signal. However, the excitation pulses are high power and require sufficient time for the hardware to recover; acquisition in this fashion will not work for rapidly-decaying signals in solids and partially-ordered liquids having very short T_2. This issue is resolved by applying a second pulse at time τ, to cause the coherence to refocus at time 2τ. These echo sequences are extremely useful as they separate the signal from any spectrometer deadtime following a pulse and transients due to switched magnetic field gradients, and also allow the experimenter to select for different coherences.

The Hahn echo is a $90_x - \tau - 180_y$ pulse sequence which refocuses Zeeman interactions such as those associated with chemical shift or local field inhomogeneity while preserving the evolution due to bilinear interactions. The solid echo is a $90_x - \tau - 90_y$ sequence. In the presence of Zeeman broadening the solid echo will refocus interactions associated with terms in the Hamiltonian which are bilinear in the spin operator I_z, in particular proton dipolar and deuteron quadrupolar interactions. In most situations either the dipolar or the quadrupolar interaction, but not both, will be significant. The roles of these echo pulse combinations in the spectroscopy experiments used in this work are specific to the applications and will be discussed in section 3.3.

The acquired signal represents a superposition of spin interactions at all interaction frequencies which modulate the nuclear Larmor frequency, each weighted by the strength of the interaction. There are two main ways to extract the information. The first, implied in the preceding discussion, is spectroscopy: the signal from the entire sample is Fourier transformed to obtain a spectrum of the contributing frequencies. This has the advantage of being sensitive to molecular length-scale fluctuations in the interactions, information which is available in the spectrum. The response is averaged over the entire sample. There is no spatial resolution and spatial homogeneity in samples is usually a requirement.

The second broad category of applications is magnetic resonance imaging and velocimetry, which are discussed below.

2.1.6 Magnetic resonance imaging (MRI)

The spatial encoding of information required for magnetic resonance imaging is achieved by applying a magnetic field gradient during the radiofrequency irradiation. Spins in the sample along the direction of increasing gradient strength have increasing local field, and their precession frequency imparts an extra phase to the spins. The phase of the spins is then related to their position in real space during an encoding step as the signal is acquired. Details of the NMR imaging method can be found in reference [19], in chapter 3.

Clearly the advantage of magnetic resonance imaging is that one obtains intensity (as the sum of all interactions contributing to the signal, for the nucleus in question) as a function of position in the sample. Often, samples with spatial inhomogeneities are deliberately used to obtain spatially resolved information, and the ability to distinguish different tissue environments is the basis of the now-indispensible use of MRI in medical applications. Pixel intensity in the image is sensitive to T_1 and T_2, and can reveal mesoscale information, but molecular length-scale (sub-nanometer) information such as internuclear distances or bond orientation is lost. Large magnetic field gradients may be used used to achieve resolution of 40 μm to 100 μm per pixel, and then the method is referred to as magnetic resonance microscopy, or "microimaging".

2.1.7 Velocimetry

Dynamic NMR microscopy works on the same principle as microscopy, with the major difference that the intensity in the resulting image corresponds not to spin density but to the displacement of the spins during a known time interval between gradient events in the pulse sequence; in other words, to the velocity. Details of the velocity encoding method can be found in reference [19], in chapter 9. From velocity maps obtained in two perpendicular directions in the plane of the flow, a velocity magnitude, or speed map, is calculated. Again the resolution is less than 100 μm per pixel. Magnetic resonance velocimetry cannot approach the resolution of optical flow visualization techniques, but it has the significant advantage that it does not have the transparency criterion and it is a valuable technique for in situ velocity measurements.

2.2 Rheometric devices

2.2.1 Horizontal Couette cell

The horizontal Couette cell consists of two concentric cylinders. Between the cylinders a laminar shear flow is established, with the long cylinder axis situated perpendicular to the external, vertical (in the lab frame) magnetic field. This geometry is a greater design challenge than is a Couette cell with long axis colinear with the drive mechanism and magnetic field direction, but the horizontal version confers significant advantages, discussed below, which were crucial to obtaining the segmental orientation results in the polymer melt. Figure 2.5 shows a schematic representation of the horizontal Couette cell at left, and a photo of the apparatus at right. The outer, stationary cylinder of the Couette cell is made of glass, with a 6 mm inner diameter. The inner, rotating cylinder is 5 mm in diameter and is made from MACOR machinable ceramic. The gap is 10 mm long and holds ~ 0.3 cm^3. of fluid. Teflon end caps ensure that no sample escapes from the gap during the experiment and a constant rate of shear is maintained throughout the sample. The RF coils are coaxial with and surround the Couette cell for maximum signal. The cell itself is designed to be removed intact through one of the two vertical supports of the apparatus, allowing interchange of ^{1}H and ^{2}H RF coils without difficult reloading of the

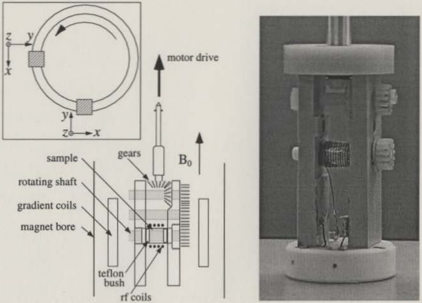

Figure 2.5: Horizontal Couette cell. The inset at left shows the hydrodynamic frame in the Couette cross-section. A photo of the assembled cell is shown at right, with one of the gears removed for the photo. The base of the apparatus fits directly onto the microimaging probe.

sample. The base of the apparatus fits directly onto the Bruker RF imaging probe, the set of magnetic field gradient coils is mounted on the outside and the entire apparatus fits up into the bore of the magnet such that the Couette cell is situated in the centre of the magnet bore where the field is homogeneous to better than one part per million.

The mechanical driving of the shear is performed via a drive shaft which runs from the top of the rheometer, up the bore of the magnet to a stepper motor. Five different gear boxes, as well as the direct drive of the motor, are used to achieve driving frequencies ranging from 0.0007 s^{-1} to 4 s^{-1}. With two turns of the inner cylinder for every three rotations of the drive shaft, this corresponds to shear rates $\dot{\gamma}$ covering the range 0.015 s^{-1}

to 83.8 s^{-1}, according to

$$\dot{\gamma} = \frac{dv_r}{dr} = \frac{2\pi r}{\text{gap}} \cdot f_r = 2\pi \frac{2.5\,\text{mm}}{0.5\,\text{mm}} \cdot f_r = 10\pi \frac{2}{3} \cdot f_d \tag{2.5}$$

where r is the inner cylinder radius, f_r is the rotation rate of the inner cylinder, and f_d is the frequency of the drive system.

The velocity field produced by the concentric cylinder Couette cell is a steady shear flow, with constant velocity gradient across the gap. The velocity in the tangential direction of the Couette cell, and the velocity gradient in the radial direction, define axes of the hydrodynamic frame. The third axis is colinear with the long axis of the Couette cell and is perpendicular to the magnetic field direction in these experiments. Within the gap the orientation of the velocity - velocity gradient axes varies with position around the Couette cell, as indicated in the inset of figure 2.5. Under shear, polymer chains experiencing anisotropy will align at some angle to these axes. Molecular alignment within the shear plane may be explored if each experiment is limited to a small arc of the flow field, in which the hydrodynamic axes lie at prescribed orientations with respect to the magnetic field (obervation) direction. Shear rates sufficiently high so as to perturb the polymer chains well into the nonlinear regime were achieved in the Couette melt experiments, and these results are used to test the Doi-Edwards model of viscoelasticity in melts.

2.2.2 Four roll mill

The four roll mill produces a more complicated macroscopic flow. A schematic of the four roll mill apparatus used for the extension experiments is shown in figure 2.6 at left, with a photo of the unassembled apparatus at right. Approximately 0.5 cm^3 of liquid is contained in the assembled sample cell.

Though several rheometric designs are able to achieve a perfectly homogeneous velocity

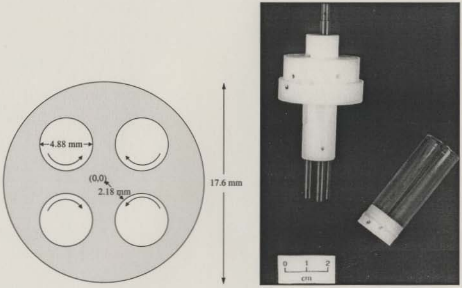

Figure 2.6: Left: dimensions of the four roll mill, drawn in cross-section, with arrows indicating direction of mechanical driving of the rollers. The distance from the stagnation point (labeled $(0,0)$) to each roller edge is $d = 2.18$ mm. The direction of the rollers can be reversed for flow in the opposite direction. Right: photo of the unassembled cell. Each of the four rollers is 4.9 mm in diameter, and the cell holds ~0.5 cc. of liquid.

field for the case of shear, it is nearly impossible to realize purely extensional flow fields in a self-contained apparatus in which the sample volumes involved can be kept small. Extension is a transient penomenon and requires continuous renewal of sample. In the four roll mill the flow is not homogeneous, and a fluid element will experience a mixture of shear and extensional velocity fields during its flow history. This is apparent from the streamlines calculated from the Navier Stokes equations for a Newtonian fluid, shown in figure 2.1, which provides a simplified picture of the ideal flow field in this apparatus. The four roll mill has the important characteristics that it is self-contained; the flow is two-dimensional — the velocity field is uniform in the vorticity direction (along the length of the roller), and so is fully described within a cross-sectional plane; and around the central, stagnation region of this device the flow is purely extensional. Because fluid elements experience long residence times in the stagnation region the extension is assumed to dominate the flow history.

2.2.2.1 Flow near a stagnation point

We are interested in the flow field in the region where the approximation of pure planar extension holds. The streamlines for a stagnation flow are the hyperbolae $\phi = \dot{\mathcal{E}}xy$ where $\dot{\mathcal{E}}$ is the velocity gradient or rate of strain. The flow is assumed to be two dimensional, and

$$v = (v_x, v_y, 0) = (-\dot{\mathcal{E}}x, \dot{\mathcal{E}}y, 0) \tag{2.6}$$

where the origin $x = 0 = y$ is taken to be the centre of the geometry. The magnitude of the velocity of a fluid element at distance r from the origin (see Fig. 2.6(a)) is $v = \sqrt{v_x^2 + v_y^2} = \dot{\mathcal{E}}r$. At $r = d$, where d is the distance from the stagnation point to each roller edge, v must match the tangential velocity at the edge of the roller and the velocity gradient $\dot{\mathcal{E}} = v/d = 2\pi f_r a/d$ is calculated directly from the mechanical driving frequency f_r. In our four roll mill cell the dimensions are roller radius $a = 2.44$ mm and distance $d = 2.18$ mm so that the ideal strain rate in the centre is $\dot{\mathcal{E}} = 7.03\, f_r$.

From $v_y = dy/dt = \dot{\mathcal{E}}y$ it follows that the stretching of the chains scales exponentially with residence time in the flow: $y = y_0 e^{\dot{\mathcal{E}}t}$, reflecting the fact that extension is a transient phenomenon. The issue of the length of time spent in the extensional flow is crucial to the total strain experienced by the molecules. The residence time diverges at the origin or stagnation point where $v_x = 0 = v_y$, and polymer molecules on streamlines which approach the origin encounter very long residence times and a high total strain.

Recently Leal *et al.* [21] have carried out detailed numerical simulations for dilute polymer solutions in a four roll mill, to find the relative amounts of shear and extension, and the resulting deformation expected, everywhere within the non-homogeneous flow field. Their results indicate that for shear rate above the critical value for coil-stretch transition, the stretched polymers modify the flow field quite dramatically and in ways which depend on parameters of the polymer solution. This means that even if the flow field can be calculated everywhere (with approximations), it is essential to have some *in situ* description of the flow field when interpreting experimental results. The flow field obtained using NMR velocimetry will be shown later in chapter 5. Despite the complexity of its flow field the four roll mill cell is a convenient rheometric apparatus for the reasons given above. It was used here to obtain data from only the stagnation region to determine director orientation during and following extension, and test predictions of the Leslie-Erickson theory for molecular orientation and dynamical behaviour of liquid crystal polymers in planar extensional flow.

2.2.3 Other rheometric devices

Other rheometric devices were used for shear experiments on liquid crystals. These will be treated only briefly since they are more standard rheometric devices. They were not specially designed for the experiments and spatially localized spectroscopy was not performed in these devices; all measurements were carried out in the bulk. Both are self-contained devices which required ≤ 1 cm^3 of sample fluid. The vertical Couette cell is a concentric cylinder apparatus, in this case with the long axis of the cylinder colinear with the magnet bore and with the drive shaft, allowing for uncomplicated coupling of the rotating inner cylinder with drive shaft extending down the bore of the magnet. The cone-and-plate cell also produces steady shear and is probably the most common rheometric geometry in use.

In this apparatus the sample is placed in the gap between a cone and a flat stationary plate. The rotation of the cone at mechanical driving frequency f_r produces a constant shear rate throughout the sample, provided the angle the cone makes with the plate is small. The shear rate is $\dot{\gamma} = 2\pi f_r/\theta_0$ for gap angle θ_0. Complete discussions of cone and plate and concentric cylinder Couette rheometers can be found in standard rheology texts [1, 4], and the particular locally-constructed cells used here are described in [22].

Rheo-NMR measurements were carried out in a 7 T magnetic field at a deuteron frequency of 42 MHz in a AMX300 spectrometer (Bruker). The commercial microimaging probehead was also built by Bruker. 20 mm and 25 mm diameter ^{2}H-tuned coils for imaging and spectroscopy were constructed specially for this work and are also suitable for more general use.

Most of the experimental results in this thesis refer to two quite different polymeric systems and are analyzed on the basis of two different molecular models. The background literature and important previous results are discussed, where helpful and appropriate, in the experimental chapters which follow.

3 Selective storage for imaging and spectroscopy

Simulations provide an opportunity to mimic experimental conditions and optimize parameters in advance without using up valuable spectrometer time. Simulated response of a spin system to RF pulses is used here to investigate selective storage of magnetization from different regions of sample in the rheometric cells in order to carry out studies of molecular ordering along different directions of the principal axis system of the molecule. The focus of application is in rheo-NMR [23, 24] studies of soft condensed matter such as polymers and liquid crystals, systems for which the intermediate motional narrowing leads to $T_2 \ll T_1$. The approach here is to selectively store magnetization from the desired regions so that it is then available for imaging or spectroscopy, at the same time destroying coherent signal from the regions we are not interested in. Both the stored signal and the incoherence induced elsewhere are temporary; the system will return to equilibrium, but on a timescale which is governed by the much longer T_1. We thus create a window in which to perform the desired measurement.

Localized NMR spectroscopy is extensively used in biomedical magnetic resonance, where a wide variety of selective excitation methods are successfully employed [25, 26, 27, 28, 29]. These methods depend on the use of a frequency-selective RF pulse applied in the presence of a magnetic field gradient, so that only spins from a desired region of the sample participate in the NMR spectrum. Because long pulses are needed to excite a narrow band of frequencies, the issue of spin relaxation during the excitation process can be important. Most sequences cause the spin magnetization of interest to execute a complex trajectory in Cartesian space, in which the respective durations of transverse and longitudinal components determine the degree of T_2 and T_1 relaxation. There are two motivating questions here. First, what happens to the spins during the excitation pulses and delays in existing selection schemes; that is, precisely how do they evolve before arriving at their final state? Second, can a selection scheme be devised, for our purposes, which is less sensitive to the critical intervals where T_2 decays enter? To address these questions, the spin response was simulated for a number of pulse sequences to determine magnetization trajectories and spatial profiles. The scheme which was found to be particularly robust against T_2 relaxation was then incorporated into a method of doing spatially resolved spectroscopy using the available NMR and rheo-NMR hardware.

3.1 Spatially localized NMR

There is an inverse Fourier relation between the pulse duration and the range of spins excited. Short, high power pulses are used to excite all spins in a sample and are called broadband or hard pulses. Frequency-selective or "soft" pulses excite only a portion of the spectrum and are much longer and of lower power. In spatial localization techniques the selective pulses are applied in the presence of a magnetic field gradient. The local frequency experienced by a nuclear spin under the action of a RF pulse and a magnetic field gradient, expressed as an offset from the Larmor frequency, is $\omega = \gamma G_z z$ where G_z is the field gradient at position z from the slice centre. The gradient in the magnetic field, by

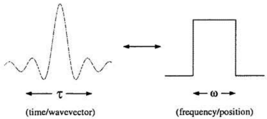

Figure 3.1: The inverse Fourier relation important in magnetic resonance. The Fourier transform of $\sin(x)/x$ is a rectangular or hat function, producing an approximately rectangular frequency profile across the sample. Usually three-lobe sinc RF pulses are used, and a very nearly rectangular spatial profile is realized.

associating each spin along the gradient direction with a unique field and hence a unique frequency ω, translates the frequency profile into a spatial profile. The larger the field gradient, the narrower the region represented by the frequency profile and the greater the spatial resolution.

The desired effect in applications is excitation or manipulation of the spins within a well-defined, rectangular spatial profile. By convention a pulse having a shape of $\sin(at)/at$, or $\mathrm{sinc}(at)$, is used, since the Fourier transform of $\mathrm{sinc}(at)$ is a hat function. This assumes that the response of the nuclear spins to the excitation, described by the Bloch equations, is linear when in fact this is only true for small excitation angles. It has been shown however that the experimental profile resulting from a modulated RF pulse is approximately proportional to the Fourier transform of the modulation [30, 31], and so for practical purposes the linear FT approximation holds. Other more complex ways to achieve a rectangular Fourier response can be imagined, and many have been shown to be quite effective [32, 33], but because of its simplicity the sinc pulse is the most widely used excitation pulse.

During the sinc pulse the excited spins are exposed to the negative effects of dephasing and transverse relaxation for part of the pulse duration, and this may lead to significant signal loss. These problems compound in situations that require that several selective pulses be applied in sequence, for example for selection in two or three orthogonal space directions leading to excitation of the region common to these slices. Ideally, the selection part of the pulse sequence must be fast enough to avoid excessive decays of the observable signal. In cases where T_2 is on the order of milliseconds to tens of milliseconds the decay can be severe.

The spatial localization method developed here, referred to as split-sinc selective storage, is based on a composite soft/hard pulse selective storage method proposed by Post *et al.* [34] and first implemented by Aue *et al.* [35]. It consists of a $\pi/2$ non-selective pulse sandwiched between the leading and trailing halves of a $\pi/2$ sinc selective pulse of opposite phase. Spins having local frequencies which fall within the bandwidth of the selective pulse experience a zero net tip angle, while spins outside the desired region are affected only by the non-selective pulse and are immediately subjected to a large (as large as possible) dephasing gradient. The method of using a large magnetic field gradient to dephase unwanted transverse magnetization is well known and has been employed in several volume localization techniques [26, 27, 35]. Since they destroy coherence between the spins for as long as the recovery time T_1, large dephasing gradients are avoided in biomedical applications involving multislice experiments wherein adjacent regions of space are excited in rapid succession. This is not the case here. The only interest in the extra-slice spins is in ensuring they do not contribute to the signal. Following the dephasing gradient the only coherent magnetization remaining lies within the pulse profile and is preserved along the z axis for later recall.

A comparative study of profiles resulting from several volume-selective pulse techniques [36] indicates that well-defined profiles may be achieved using the pulse cluster described above. The relevant magnetization trajectories for several selection techniques were investigated as part of this thesis project, and the split-sinc selective storage pulse scheme was found to be particularly suitable in the case of spin systems for which $T_2 \ll T_1$. Its associated magnetization trajectories and resulting profiles are compared here to those for another possible method of z-storage consisting of a standard refocused $\pi/2$ sinc selective pulse followed by a $-\pi/2$ non-selective storage pulse. This approach is taken simply to point out the significant advantage, in severe T_2 situations, of the split-sinc selective storage pulse over selective techniques employing conventional sinc excitation pulses. The focus will then be on the application of this approach in the rheo-NMR geometries shown in figure 2.1.

3.2 Numerical methods

The magnetization trajectories were investigated by solving the Bloch equations in the rotating frame of the RF pulse. The Bloch equations are the relations appropriate to NMR imaging for describing the response of the components M_x, M_y and M_z of the spin magnetization vector, to RF perturbation. For a static field B_0 along z and an RF field B_1 applied along x, these equations are

$$\begin{aligned}\frac{\mathrm{d}M_\mathrm{x}}{\mathrm{d}t} &= \gamma M_\mathrm{y}(B_0 - \omega/\gamma) - \frac{M_\mathrm{x}}{T_2}\\ \frac{\mathrm{d}M_\mathrm{y}}{\mathrm{d}t} &= \gamma M_z B_1 - \gamma M_\mathrm{x}(B_0 - \omega/\gamma) - \frac{M_\mathrm{y}}{T_2}\\ \frac{\mathrm{d}M_z}{\mathrm{d}t} &= -\gamma M_\mathrm{y} B_1 - \frac{M_z - M_0}{T_1} \qquad (3.1)\end{aligned}$$

in a frame of reference rotating with the spins at the Larmor frequency. Here M_0 is the equilibrium value of the polarization along z, and γ is the gyromagnetic ratio of the nucleus under study. The local frequency experienced by a nuclear spin under the action of the RF pulse and the magnetic field gradient is $\omega = \gamma G_z z$ at position z from the slice centre.

A fourth-order Runge-Kutta algorithm [37] was used to find numerical solutions to the coupled Bloch equations (Eq. (3.1)) and simulate the response of the spin system to an arbitrary RF excitation. Given known values for variables at some point x and the known functional form for their derivatives, this integration technique advances the solution over the interval h by first finding the derivatives at x, finding the derivatives twice at $x + h/2$, and finally at $x + h$. In the fourth-order Runge-Kutta method the error scales with the interval size h to the fourth power. One major benefit of the numerical versus analytical approach is that one does not need to know the form of the Fourier transform to determine the spatial response. Any arbitrary pulse shape can be handled in this way. Equations (3.1) were solved during the pulses and the subsequent dephasing gradient, to arrive at spatial profiles which could be compared with each other.

Typically 512 points were used to represent the spatial profile, and for each of these points the magnetization trajectory was calculated over 2048 time steps, covering all pulse, gradient and rephasing elements in the pulse sequence. For multiple applications of the pulses the number of time steps was increased accordingly. The calculations presented here are for 2 ms three-lobe sinc selective pulses, starting magnetization vector $\vec{M} = [0, 0, 1]$, and values for gradient strength and hard pulse duration appropriate for typical experimental hardware. For slice selection a gradient of 0.0176 T/m was used in the numerical solutions, corresponding to 5% of the maximum gradient available for the gradient power supplies. 25% gradient strength or 0.088 T/m was used for the 1 ms dephasing gradients. A value of B_1 of 0.3 mT was used, corresponding to a 20 μs non-selective $\pi/2$ pulse.

The time evolution of in-slice magnetization, during the preparation along z and the subsequent large dephasing gradient, is shown in figures 3.2(a) and 3.2(b). For the split-sinc selective storage pulse cluster, M_z is only momentarily tipped toward the transverse

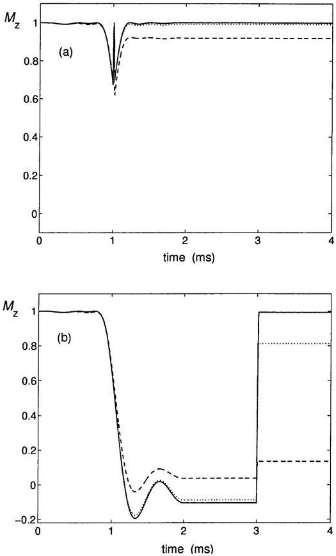

Figure 3.2: Simulated time evolution of in-slice magnetization M_z for (a) $(\pi/4)_{sel}$-$[-\pi/2]$-$(\pi/4)_{sel}$ and (b) $(\pi/2)_{sel}$-$[-\pi/2]$ z-storage for $T_2 = 1$ s (black solid lines), $T_2 = 10$ ms (dotted lines), and $T_2 = 1$ ms (dashed lines). The selective pulses are 2 ms three-lobe sinc pulses.

plane (fig. 3.2(a)) and is successfully prepared along z before the large spoiler gradient is applied. Consequently the signal in the spatial profile is almost entirely preserved even when T_2 conditions are severe. This is impressive when compared to sinc pulses (fig. 3.2(b)), for which the magnetization undergoes a large excursion into the transverse plane where it remains for almost the entire second half of the pulse. When T_2 is on the order of 1 ms, less than 20% of the in-slice magnetization is recoverable following the z-storage. For selection techniques employing sinc excitation pulses, the resulting loss of signal in the magnetization profile can be dramatic, especially when the nature of the experiment requires selection in more than one direction. Figure 3.3 compares the calculated profiles following two successive applications of the selection, for a typical total z- storage duration of 8 ms. For the calculations using $T_2 = 10$ ms shown in figure 3.3 (a), both profiles are well-defined. However the split-sinc selective z-storage preserves 98% of the in-slice magnetization, compared to 67% for the refocused sinc pulse. The comparison is much more dramatic for the extreme case of $T_2 = 1$ ms (fig. 3.3 (b)). The split-sinc pulse profile is now less sharply defined, yet a full 84% of the starting signal is preserved in the profile. In contrast the sinc profile has been reduced to 2% of its original signal.

Several other pulses which are shown to have excellent spatial profile characteristics [26, 27, 33] were also investigated. In normal liquids or tissue comprised mostly of water these schemes are very appropriate. None of the these were as robust as the split-sinc sequence against severe T_2 relaxation. Based on the excellent performance of the split-sinc selective storage method in terms of rectangular slice profile and short exposure of M_z to transverse dephasing, we incorporated it into a method of doing spatially selective spectroscopy. Using this selective storage precursor along with the appropriate NMR spectroscopy experiment, direct spatial information about flow-induced alignment is obtained.

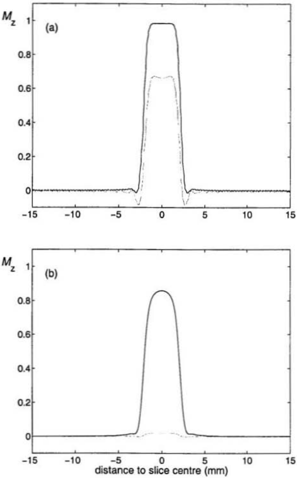

Figure 3.3: Profiles across the desired slice following two successive applications of the split-sinc (shown in black) and refocused sinc (gray) z-storage methods, representing selection in two orthogonal directions in strongly relaxing spin systems: (a) T_2 = 10 ms; (b) T_2 = 1 ms.

3.3 Spectroscopy

In solids and liquid crystals the quadrupolar interaction strengths are hundreds of kHz, and the splittings are easily resolved via quadrupolar echo experiments. In contrast, flow-

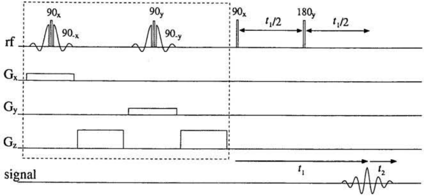

Figure 3.4: Pulse sequence showing two applications of the selective storage cluster (the portion outlined by the dashed line) followed by the two-dimensional spectroscopy experiment. The dephasing gradient shown here is applied along z, however it may equally be applied in any (or all) of the three orthogonal directions following the z-storage.

induced alignment of chain segments in entangled polymers is extremely weak. The probe molecule reports on the weakly ordered segments and the quadrupolar splittings are on the order of tens of Hz. If the design of the sample/probe is anything other than one which has a high degree of symmetry with the magnetic field, there will be inhomogeneities in the magnetic field across the sample. This results in inhomogeneous broadening of the spectral linewidth in the acquisition domain and a fundamental lower limit on the splittings which can be resolved in that sample via a straightforward quadrupolar echo experiment. In the horizontal Couette the intrinsic linewidth is approximately 100 Hz. Clearly, normal quadrupolar echo experiments in the acquisition domain will not be sufficient to pick out the weak ordering effects. Instead, in the Couette experiments, two-dimensional spectra were acquired. The pulse sequence used is pictured in figure 3.4. In this method a series of Hahn echoes were collected wherein the delay time t_1 was incremented to define the evolution domain. The Hahn echo refocuses all Zeeman effects, and the second rank tensorial interactions remain to modulate the echo. t_1 is chosen carefully to ensure the

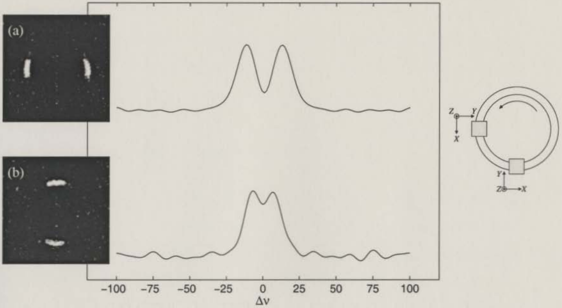

Figure 3.5: Representative ^{2}H NMR spectra obtained using the selective storage technique, for a deuterated benzene probe molecule in a polymer melt under shear in the horizontal Couette cell. The spectra were obtained at shear rate $\dot{\gamma} = 16.8\,\mathrm{s}^{-1}$ and using the spectroscopy sequence of figure 3.4. The corresponding images using the selective storage precursor were obtained with the fluid at rest. At top, signal is selectively obtained from the region of the gap where $\vec{v} \parallel \vec{B}_0$, and at bottom where $\nabla\vec{v} \parallel \vec{B}_0$. The orientations of the hydrodynamic frame in the selected regions, discussed in section 2.2.1, are indicated in the cartoon at right.

evolution domain is sufficiently wide or narrow to describe the spectrum, and with properly phased spectra, the amplitude of the echo peak undergoes a cosine modulation along the evolution domain. The frequency of the modulation corresponds to the strength of the remaining (here, quadrupolar) interaction, which appears as a splitting in the evolution domain Fourier transform. Figure 3.5 shows representative ^{2}H NMR spectra in the horizontal Couette cell, with corresponding images taken with the selective storage precursor to confirm its selectivity. For the upper spectrum the velocity is parallel to B_0 at the sides of the 0.5 mm gap region, and for the lower spectrum the velocity gradient is parallel to B_0 at the top and bottom of the Couette gap. The splittings differ because in the melt under shear, the normal stress induced in the polymer chain segments along the velocity direction is larger than the reduction in normal stress along the velocity gradient direction. We will return to these experiments in chapter 4 where the full results for the polymer melt are presented.

3.4 Remarks on implementation

Several difficulties were encountered when the selective storage technique was implemented. Of particular note are the switching times for the pulse phase and for the gradient power supplies. The frequency selective and broadband RF pulses are transmitted via low- and high-power amplifiers, respectively. These pulses must also be of opposite phase. While switching between the amplifiers is very fast on the AMX-300 spectrometer, the phase of the pulse could not be switched within an acceptable length of time. To avoid this, the leading and trailing halves of the selective pulse are provided to the spectrometer as negative waveforms. The effect of switching the phase is thus achieved without experiencing the associated hardware delays.

The simulated profiles in Fig. 3.3 show the ideal situation in which the magnetic field gradient can be removed during the application of the hard pulse in the middle of the pulse cluster. This also presented a hardware challenge, as the time needed for the gradients to be reliably turned on or off and for eddy currents within the magnet structure to die out, increases with the strength of the gradients. For these applications resolution is key, gradients are always high, and the switching time required is hundreds of μs. During this time there will be irreversible dephasing of the spins of interest and consequently loss of signal. Alternatively, the gradient is not allowed to fall until the desired magnetization has been prepared along z. The delivery of the broadband pulse in the presence of the

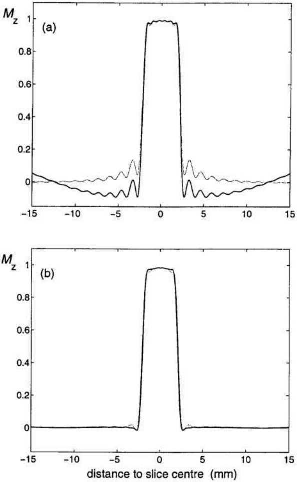

Figure 3.6: (a) Numerical results for distorted slice profile (shown in black) corresponding to application of the non-selective pulse in the presence of the magnetic field gradient. The profile is compared to that obtained with magnetic field gradient removed during the application of the broadband pulse (gray). The simulated profiles obtained for two applications of the z-storage precursor are shown in (b). T_2 = 10 ms in these calculations.

gradient imparts a sinc modulation to the desired profile. The slice remains sharply bounded but the baseline suffers a distortion as shown in figure 3.6 (a). This corresponds closely to what we observe in experimental profiles. According to the numerical results, shown in fig. 3.6 (b), a second application of the selection along the same direction should eliminate the distortion. In practice it is not always possible to completely eliminate extra-slice signal in this way. The severity of the sinc distortion scales with the gradient strength and with the duration of the broadband pulse, which in turn depends on the quality factor of the resonator or coil used to deliver the RF power. For a given desired slice width and broadband pulse duration, a shorter selective pulse requires a larger field gradient, leading to narrowing of the unwelcome wings toward the desired slice. This trade-off, and not the upper limit of the gradient strength itself, determines the selective resolution obtainable on our spectrometer.

The limitations imposed by these conditions are highlighted in Fig. 3.7. In this case the selective storage method is used to obtain critical alignment information for a polymer liquid crystal, poly(γ-benzyl-L-glutamate) (PBLG) in dioxane/nitrobenzene, in the four-roll mill apparatus. The region of interest is in the centre of this device where the flow closely approximates a stagnation flow and can produce large extension of the polymer chains. We are able to achieve signal exclusively from a very well defined region of 4 mm × 4 mm (Fig. 3.7 (b)). At still larger gradient, for a selected region of side length 2.5 mm, the desired region remains well defined but the contribution to the spectrum from the wings (Fig. 3.7 (c)) becomes unacceptable.

One alternative is to apply a single selection in each orthogonal direction, using half the desired gradient strength (storing signal from twice the desired region), followed by a second round of selection using the full desired gradient strength. This proved effective in

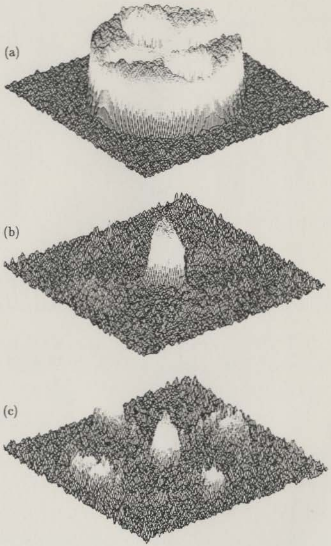

Figure 3.7: Experimentally determined spatial profiles of polymer liquid crystal in deuterated solvent, in the four-roll mill: (a) a 2 mm layer of fluid; (b) selection in two orthogonal directions to obtain signal from a 4 mm square region in the centre of the 18 mm diameter cell; (c) selection of 2.5 mm square region results in significant signal from the extra-slice wings. The images were obtained using a locally constructed 20 mm ^{2}H Helmholtz coil.

later extension experiments around the stagnation point in the four roll mill.

In each of a series of acquisitions, we normally use large dephasing gradients and more than one application of the storage precursor, either to select in two or three dimensions or to minimize the unwanted signal from the sinc wings. Used in this way the method is very demanding of the field gradient coils. Care must be taken to monitor their temperature and to allow sufficient time between acquisitions. If possible, air cooling should be used to prevent damage to the gradients and also to avoid temperature variations in the sample during the experiment.

The split-sinc selective storage method developed here is a very useful implementation of earlier suggestions. It is well-suited to studies of complex fluids which have dynamics intermediate between those of liquids and solids. Its utility is limited by the particular hardware available, however switching delay times can be avoided by using a constant gradient and constant phase setting during the RF excitation process. Compensation techniques to improve the slice profile, as suggested by Müller *et al.* [38], have not been attempted in these experiments but might be incorporated in the future. While this method has been tailored to suit rheo-NMR methods, it can easily be extended to a wide range of applications. For example the selective storage precursor has also been used in velocity imaging, and it has proven particularly valuable as a slice selection tool in Echo Planar Imaging experiments. It is not designed for solids which have T_2 much shorter than a millisecond as well as very short T_1. Its distinguishing features are that it may be added as a slice selection precursor to any pulse sequence consisting entirely of hard pulses, that its effect may be easily ascertained by subsequent imaging, and that it is found to be extraordinarily robust against T_2 relaxation.

We turn now to the motivation for developing this technique and the core of the thesis work: shear and extensional flow studies of complex fluids.

4 Polymer melt under shear

Having established the method of extracting spatially-localized NMR spectral information in complex fluids, we turn now to polymer conformation in high shear. The experiments described here combine the use of shear flow in the Couette cell to drive a system of entangled, flexible polymers away from equilibrium, with the deuterium quadrupolar interaction as a sensitive probe of the nonlinear viscoelastic response. The observations of orientation and dynamics at the length scale of the polymer chain segments provide a means of testing predictions of the most widely accepted microstructural theory for concentrated solutions and melts, with fascinating results. Suggested corrections to the theory are also evaluated in relation to the NMR data.

4.1 Reptation dynamics

We imagine a single polymer chain in a melt or concentrated solution wriggling about via thermal motions through a matrix of other polymers, exploring possible conformations in a random fashion. This is de Gennes' idea of "reptation" [39]. A model to describe the many entanglements of a chain with its neighbours, incorporating reptation, was first suggested by Edwards [40] and developed in full by Doi and Edwards in 1978 [41, 42, 43, 44]. The motions of polymer chains are largely directed along a tube defined by constraining

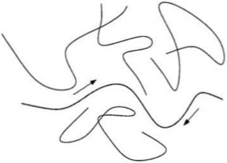

Figure 4.1: Tube model: in concentrated solutions and melts chains are restricted by neighbouring chains to motions along the contour length of the tube. The stress tensor is calculated through traction in the chains.

entanglements with the neighbouring chains (Fig. 4.1). There is a hierarchy of relaxational motions which the chain will undergo in this model. Roughly, the dynamics can be grouped into motions which are

(i) characterized by τ_e, corresponding to crossover dynamics between a chain in free space and one which feels the tube of constraints from neighbouring chains. Dynamics faster than τ_e are short length scale, fast motions parameterized by a, an effective radius of the tube.

(ii) intermediate motions characterized by time τ_R for the fluctuations in the ends of the tube; these fluctuations are called Rouse modes and take place as the deformed chain retracts along the tube, restoring the tube's contour length.

(iii) comparable to the longest relaxation time (corresponding to slowest dynamics) τ_d, the time for the chain to define a new tube. τ_d is called the reptation time or alternatively the tube disengagement time and roughly scales with the cube of the molecular weight. In general, $\tau_d \gg \tau_R$ for long polymer chains.

Under equilibrium conditions polymer solutions and melts are isotropic. Under deformation, a competition arises which is wholly a matter of timescales. Shear response is characterized by the Deborah number $De = \dot{\gamma}\tau_d$, the ratio between the timescale for the polymer segments to relax back to equilibrium and the time scale for the deformation. The shear field perturbs the microstructure only slightly when $De < 1$ and in nonlinear fashion when $De > 1$. Put another way, if $\dot{\gamma} < 1/\tau_d$ the molecule wins the competition and can reorient faster than it is being deformed, and the polymer chain remains on average roughly spherical. The segments can sample all possible orientations during the experiment. The resulting ^{2}H NMR spectrum will contain a single isotropic line. If the deformation is faster than the reorientation, there will be an anisotropic distribution of segment orientations. This is manifested in the NMR spectrum as a dipolar or quadrupolar broadening of the line, or a splitting into two lines (see Sec. 2.1.3). This splitting is not just a signature of anisotropy; it is a direct measure of elements of the stress tensor. This is because (1) in the Doi Edwards model the segmental distribution tensor is directly related to the stress tensor; and (2) we can manipulate the geometry of the rheometry experiment to access in turn each of the principal components S_{XX}, S_{YY} and S_{ZZ} of the segmental alignment tensor. These two assertions form the basis of the studies of molecular origin of stress in entangled, strongly sheared polymers presented in this chapter.

4.2 The model of Doi and Edwards

The Doi-Edwards model for polymer dynamics is a kinetic theory. It follows the basic steps outlined for microscopic theories for viscoelastic behaviour in section 1.2. The authors begin with a treatment of polymers as point particles which undergo Brownian dynamics and experience negligible hydrodynamic drag [6]. The conformational distribution function

Ψ obeys the Smoluchowski equation, which reads [6]

$$\frac{\partial \Psi}{\partial t} = \frac{\partial}{\partial x}\frac{1}{\zeta}\left(k_B T \frac{\partial \Psi}{\partial x} + \frac{\partial U}{\partial x}\Psi\right) \tag{4.1}$$

where U is an external potential exerting a force and imparting some average flux velocity to the particles, and ζ is the friction constant or resistance to the external force. Eq. (4.1) is analogous to Fick's law for diffusion with an added term (the second term on the right) corresponding to a driving force. It can be thought of as the diffusion equation in phase space for the probability $\Psi(x,t)$, for dilute polymer solutions and suspensions where the polymers are treated as non-interacting Brownian particles. For concentrated solutions and melts where the entanglement situation prevails, the sought-after conformational distribution must be that of the chain segments. The extension of the foregoing to this more realistic situation becomes much more involved since there are many more degrees of freedom (for each chain segment of each polymer molecule), the polymers have finite size (and thus no longer negligible hydrodynamic interactions), and the topological considerations must be taken into account (the chains cannot cross each other). The Smoluchowski equation for the evolution of Ψ does still apply, but becomes considerably more involved [6].

As an alternative, more tractable approach Doi and Edwards elect to start with concentrated polymer solutions and melts as networks [45, 46]. The treatment which follows is valid so long as the timescale of the deformation is longer than the Rouse relaxation time τ_{R}. This means that while the average alignment of tube segments is changing, the tubes remain unstretched. For high molecular weight polymers the condition $\dot{\gamma} < 1/\tau_{\mathrm{R}}$ is easily met for a wide range of shear rates, up to $\dot{\gamma} \sim 100/\tau_{\mathrm{d}}$.

The distribution function $\psi(s,t)$ is the probability that an original segment s of a re-forming tube remains as a segment of the new tube at time t. Only those segments remaining in the tube keep the same entanglement configuration, are oriented by the flow and contribute to the stress. $\psi(s,t)$ is the integral over the tube length L of the probability Ψ that the original chain moves distance ξ while its ends have not yet reached the segment s. Ψ is required to satisfy the much simpler one-dimensional diffusion equation

$$\frac{\partial \Psi}{\partial t} = D_c \frac{\partial^2 \Psi}{\partial \xi^2} \tag{4.2}$$

as the chain diffuses length ξ along the tube. The diffusion coefficient D_c is directly related to the reptation time by $D_c = L^2/(\tau_{\rm d}\,\pi^2)$. With boundary conditions specified in [6], Doi and Edwards solve Eq. (4.2) with the result

$$\psi(s,t) = \sum_{p\,\mathrm{odd}} \frac{4}{p\pi} \sin\left(\frac{p\pi s}{L}\right) e^{-p^2 t/\tau_{\rm d}}$$

and

$$\psi(t) = \frac{1}{L}\int_0^L ds\,\psi(s,t) = \sum_{p\,\mathrm{odd}} \frac{8}{p^2\pi^2} e^{-p^2 t/\tau_{\rm d}}. \tag{4.3}$$

$\psi(t)$ is a relaxation function for tube disengagement. It has the behaviour shown in Fig. 4.2, plotted against $t/\tau_{\rm d}$ and normalized to $\int dt\,\psi(t) = 1$. In a time less than $\tau_{\rm d}$, $\psi(t)$ has dropped to half the $\psi(0)$ value. For times longer than $4 \times \tau_{\rm d}$ there is essentially zero probability of an original tube segment remaining *because of thermally-driven diffusive motion of the segments.*

The non-thermal, reorientational motions of the chain segments driven by the applied macroscopic velocity field are accounted for in the expression for the stress tensor [6]:

$$\sigma_{\alpha\beta}(t) = \frac{c}{N}\frac{3k_BT}{Nb^2}\left\langle \int_0^{L(t)} ds L(t) u_\alpha(s,t) u_\beta(s,t) - \frac{1}{3}\delta_{\alpha\beta} \right\rangle. \tag{4.4}$$

The stress depends on the angle between the direction of flow and the unit vector $\vec{u}(s,t)$ tangent to the chain at segment s, and on $L(t)$ the (changing) contour length of the tube along which the tensile force acts. The stress tensor depends directly on bond orientational order.

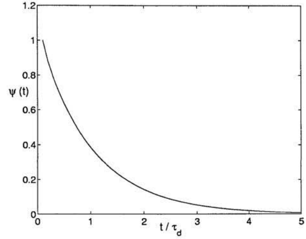

Figure 4.2: Probability distribution function in the tube, $\psi(t)$, as calculated by Doi and Edwards. The calculation here is for the first five terms in the sum in Eq. (4.3), for times ranging from $t = \frac{1}{5}\tau_{\mathrm{d}}$ to $t = 5\,\tau_{\mathrm{d}}$.

By this result, the expression for the stress tensor in Eq. (4.4) is very closely related to that for the orientation tensor, defined as

$$S_{\alpha\beta}(s,t) = \left\langle u_\alpha(s,t)u_\beta(s,t) - \frac{1}{3}\delta_{\alpha\beta}\right\rangle \tag{4.5}$$

in Sec. 2.1.4. In fact, in the NMR experiment the observation is over all segment orientations, so that the observed segmental alignment is

$$S_{\alpha\beta}(t) = \frac{1}{L}\int_0^L ds \left\langle u_\alpha(s,t)u_\beta(s,t) - \frac{1}{3}\delta_{\alpha\beta}\right\rangle . \tag{4.6}$$

$\sigma_{\alpha\beta}(t)$ is directly proportional to $S_{\alpha\beta}(t)$ for our shear flow. It is therefore sufficient to find an expression for the (shear rate-dependent) segmental alignment tensor in order to evaluate the response functions such as shear stress, normal stresses and viscosity.

The segmental alignment depends entirely on the history of the deformation and of the relaxation, obtained as an integral over past time and averaged over the chain segments:

$$\langle S_{\alpha\beta}(t)\rangle = \int_{-\infty}^{t} dt' \left(\frac{\partial}{\partial t'}\psi(t-t')\right) Q_{\alpha\beta}^{(IA)}\left(\boldsymbol{E}(t,t')\right). \tag{4.7}$$

$\psi(t-t')$ describes the relaxation of the segments and $Q_{\alpha\beta}$ is the distribution of segment orientations as a function of the deformation gradient history tensor $\boldsymbol{E}(t,t')$. $Q_{\alpha\beta}^{(IA)}$ is the "independent alignment" (IA) approximation for the tube orientation distribution. The IA approximation is employed in the model to simplify the way the averaging over the solid angle is carried out, and will be discussed further in section 4.7. The stress tensor is written

$$\sigma_{\alpha\beta}(t) = G_e \int_{-\infty}^{t} dt' \left(\frac{\partial}{\partial t'}\psi(t-t')\right) Q_{\alpha\beta}^{(IA)}\left(\boldsymbol{E}(t,t')\right) \tag{4.8}$$

where $G_e = 3k_{\mathrm{B}}Tcb^2/a^2$ is the relaxation modulus (the term is carried over from linear viscoelastic models which use a purely elastic relaxation of the stress) and depends on the properties of the material. b is the statistical segment length and c the number of segments per volume. Thermodynamic dependence is explicit in G_e, and is implicit in the thermal modes of relaxation which contribute to $\psi(t)$. The above expression for $\sigma_{\alpha\beta}$ (Eq. (4.8)) and an appropriate probability function $\psi(t)$ together form the constitutive equation for concentrated solutions and melts.

4.2.1 Predictions of the Doi Edwards model

At this point the problem is one of solving for $Q_{\alpha\beta}(\boldsymbol{E})$, incorporating the alignment vector $\vec{u}$ and the tensor $\boldsymbol{E}$ which describes the history of the velocity gradient tensor $\boldsymbol{\kappa}$ (defined previously in equation 1.1). In steady shear,

$$\boldsymbol{E} = \begin{bmatrix} 1 & \gamma(t,t') & 0 \\ 0 & 1 & 0 \\ 0 & 0 & 1 \end{bmatrix}. \tag{4.9}$$

The strain is γ, and the strain history is explicitly accounted for by $\gamma(t,t') = \int_{t'}^{t} dt''\kappa(t'') = (t-t')\dot{\gamma}$. Then the solution for $S_{\alpha\beta}$ can be found.

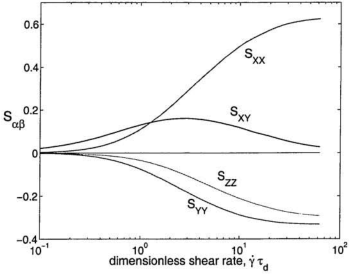

Figure 4.3: Predictions of the Doi Edwards model for elements of the segmental alignment tensor $S_{\alpha\beta}$, as functions of shear rate made dimensionless by the reptation time τ_d. The stress tensor $\sigma_{\alpha\beta}$ is directly proportional to $S_{\alpha\beta}$. All of the calculations presented here were performed in Matlab [47].

$S_{\alpha\beta}$ in Eq. (4.7) has been evaluated by Callaghan *et al.* [48] using the exact reptation expression for $\psi(t)$, namely $\psi(t) = \sum_{p\ \mathrm{odd}} \frac{8}{\pi^2 p^2} \exp(-p^2 t/\tau_d)$ (from Eq. (4.3)). Figure 4.3 shows the full predictions for $\langle S_{\alpha\beta}\rangle$ under steady shear. Recall that $\sigma_{\alpha\beta} \propto S_{\alpha\beta}$; in essence, these are the stress tensor curves. Consequences of the DE model evident from the computed curves are:

1. $S_{YY} \neq S_{ZZ}$, in other words $\sigma_{YY} \neq \sigma_{ZZ}$; the deformation in steady shear is not uniaxial.

2. σ_{XX}, σ_{YY} and σ_{ZZ} sum to zero, as they must.

3. with increasing shear rate, the shear stress σ_{XY} increases up to $\dot{\gamma}\tau_d \sim$ unity, then begins to decrease slowly towards zero. The model thus predicts unstable flow in shear regimes where, experimentally, only stable flow has been observed. Rheologists can measure shear stress vs. shear rate (the flow curve) in the bulk, and in melts and concentrated solutions σ_{XY} always reaches a plateau above $De \sim 1$ and is never seen to approach zero [49, 50, 51]. The bare DE model underpredicts the shear stress for $De > 1$. This is a serious flaw of the original DE model.

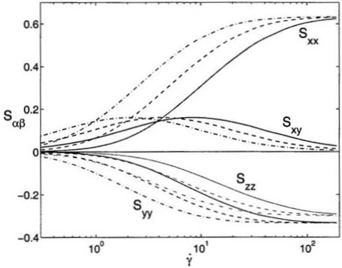

Figure 4.4: Predicted shear-rate dependence of $S_{\alpha\beta}$, for reptation time τ_d = 330 ms (solid lines); τ_d = 660 ms (dashed lines); τ_d = 1.32 s (dot—dashed lines).

Plotting $S_{\alpha\beta}$ versus shear rate $\dot{\gamma}$ (as opposed to vs. reduced shear rate $\dot{\gamma}\tau_d$) reveals another important feature of the model (see Fig. 4.4):

4. for increasing shear rate $\dot{\gamma}$, while the asymptotic plateau values of $S_{\alpha\beta}$ do not change, the rate at which the plateaus are reached depends on τ_d. The longer the polymer chain, the smaller the shear rate at which $\dot{\gamma}\tau_d \sim 1$ and nonlinear behaviour sets in.

4.2.2 Extinction angle

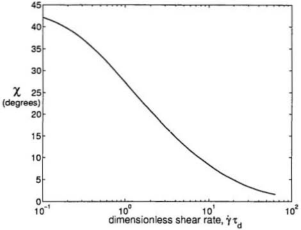

Figure 4.5: Prediction of the Doi Edwards model for the extinction angle χ as a function of reduced shear rate $\dot\gamma\tau_d$.

In the DE model,

$$\chi = \frac{1}{2}\tan^{-1}\left(\frac{2\,\sigma_{XY}}{\sigma_{XX}-\sigma_{YY}}\right)$$

is the alignment angle which the principal axes of $S_{\alpha\beta}$ make with X. Physically, χ defines the degree of orientation of the long axis of the molecule with the velocity direction. As defined, χ exactly corresponds to the extinction angle in birefringence studies, where $\chi = \frac{1}{2}\tan^{-1}\left(\frac{2\,n_{12}}{n_{11}-n_{22}}\right)$ is defined in terms of the intrinsic birefringence $n_{\alpha\beta}$ of the polymer. The correspondence between the two is via the stress-optical rule $n_{\alpha\beta} = C\sigma_{\alpha\beta}$ [52] where C is the stress-optical coefficient. $\sigma_{\alpha\beta}$ and $n_{\alpha\beta}$ are both strongly influenced by anisotropy, ultimately through bond orientational order, and the stress-optical rule has been shown to hold well into the nonlinear regime in melts and concentrated polymer solutions. Fig. 4.5 shows the calculated shear rate-dependence of the extinction angle χ in the DE model. As $\dot\gamma$ increases, $\chi(\dot\gamma\tau_d)$ decreases from its quiescent state value of 45 degrees (having no preferred orientation) to an asymptotic value near zero, indicating increasing polymer orientation along X.

4.3 Previous studies

Samulski and co-workers first observed weak segmental alignment via ^{2}H NMR in a poly(isobutane) fluid under shear, with the signal obtained from a small deuterated probe molecule [53], and also in affinely deformed networks of isotopically labeled polyisoprene [20]. In the stretched network, broadening of the single isotropic line caused by the quadrupolar interaction was seen to increase with the degree of stretching, as predicted by a simple uniaxial elongation. Birefringence measurements of the extinction angle χ are in fairly good agreement with the prediction of the Doi-Edwards model [52]. Information regarding molecular ordering in polymers has also been obtained from neutron scattering, where the radius of gyration tensor is calculated as a correlation of displacements of segments from the centre of mass, averaged over a length scale which depends on the wave vector in the experiment. The radius of gyration tensor is a measure of an alignment angle in shear. Sekiya and Doi [54] have calculated the theoretical radius of gyration tensor as a function of shear rate and find a functional form for the alignment angle similar to that of the Doi-Edwards model. Experimentally, for large wave vectors (corresponding to short length scales) the alignment angle observed in neutron scattering is similar to the extinction angle χ, however for small wave vectors the angle appears to be close to zero [55, 56]. This suggests that the deformation of the polymer, when examined at larger length scales, is different from that seen in birefringence.

4.4 The experiments

The shear experiments described below were performed on high molecular weight ($M =$ 610 000) poly(dimethyl siloxane) (PDMS) obtained from Polysciences (Warrington, PA). Its polydispersity is $M/M_n = 2.0$. M_0, the molecular weight per monomer, is 74, and the molecular weight between chain entanglements M_e is estimated to be 10 000 for this PDMS melt [23]. The ^{2}H signal is obtained from either an oligomer of PDMS which should sample the same local environment as neighbouring host polymer chains, or from a benzene probe molecule which diffuses over many chain segments on the timescale of the NMR experiment so that overall segment orientation is probed [57]. The results presented here were obtained in the horizontal Couette cell described in section 2.2.1 and in [22], using the two dimensional quadrupole spectroscopy sequence shown in figure 3.4. The relative orientation of the lab frame, the hydrodynamic frame in which the Doi-Edwards description applies, and the molecular frame, are shown in Fig. 4.7. Φ is the angle which the velocity direction X makes with the magnetic field[1]. The interaction strength in the NMR spectrum is proportional to $\left\langle u_z u_z - \frac{1}{3} \right\rangle$ (see section 2.1.4) and hence also to the diagonal elements of alignment tensor, and we access the different elements by choice of the geometry of the experiment. For example in the horizontal Couette cell, for a small region of fluid at $\Phi = 0$ the velocity direction X is coincident with $\vec{B_0} = B_0\hat{z}$ and the NMR interaction strength is proportional to S_{XX}. Because of the use of an indirect probe, and

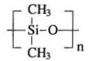

Figure 4.6: Momomeric unit of poly(dimethyl siloxane).

---

[1] As distinguished from χ, which is the orientation of S_{XX} with respect to X.

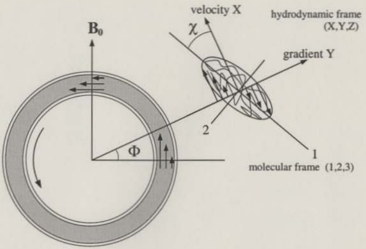

Figure 4.7: The relevant frames of reference in the horizontal Couette cell experiment.

the motional averaging issues discussed in Sec. 2.1.4, the observed quadrupolar interaction is scaled with respect to the absolute alignment. However, the relative values of the quadrupolar interaction strength follow precisely the defined tensor elements.

4.5 Shear rate-dependence of alignment, ^{2}H oligomer in PDMS melt

The first attempts at observing nonlinear viscoelastic effects in the Couette cell using the selective storage method on several entangled polymer systems were unsuccessful. In poly(ethylene oxide) (PEO) at 20 wt % in D_2O, which did show evidence of orientational ordering under extension in the four-roll mill in prelimiary experiments, neither a splitting nor a broadening of the isotropic line was observed in the horizontal Couette cell. The deuterated water probe molecule did not reveal any shear-induced microstructural changes in the host chains. High molecular weight polystyrene in dioctyl phthalate (essentially a benzene ring with two side groups, in which polystyrene is soluble), was the next candidate. Since the polystyrene could be obtained in deuterated form it was hoped that flow-induced anisotropy might be observed with the signal directly from the chains rather than via a reporter molecule. This concentrated polymer solution (8 wt % ^{2}H PS in DOP) also proved to be unsuitable for the horizontal Couette cell experiment, because of its NMR characteristics: its short (~ 2 ms) T_2 relaxation time could be dealt with using the selective storage technique, however its T_1 of less than 10 ms was too short to allow for acquisition of the signal. This system had very short reorientational relaxation times and was simply too elastic for these experiments.

A deuterated PDMS oligomer probe of 10 000 molecular weight was provided by Professor Ed Samulski (UNC, Chapel Hill, USA), and the experiment was attempted on a high molecular weight ($M = 610\,000$, or 610K) PDMS melt in which the oligomer was introduced at 10 wt % concentration. The melt has a consistency between petroleum jelly and silicone sealant; it is difficult to load into the Couette gap, can be driven out of the gap during shear, and has viscosity large enough to initially cause the teflon end caps, and with them the outer cylinder with which the end caps establish a seal, to rotate with the melt as a solid body. The horizontal Couette cell had to be modified to ensure the sample was properly sheared. After these technical problems were resolved the melt showed a small splitting under shear, with signal selectively obtained from the region in which the velocity X is parallel with the magnetic field.

Spectra were directly acquired for several shear rates at this orientation (which we designated to be 0°) up to $\dot{\gamma} = 16.8\,\mathrm{s}^{-1}$, and also with the velocity gradient Y parallel to $\vec{B}_0$ ($\Phi = 90°$). Following the latter series of experiments the $\Phi = 0°$ orientation was selected again under shear to check the results for consistency, and the splitting for that shear

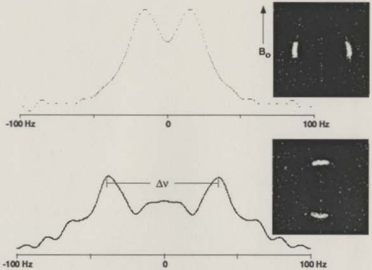

Figure 4.8: ^{2}H spectra for 610K PDMS melt containing the ^{2}H oligomer at 10% in the horizontal Couette cell at $\dot{\gamma} = 12.6\ \mathrm{s}^{-1}$, obtained using the two-dimensional spectroscopy method for selected regions having velocity direction (top) and velocity gradient direction (bottom) parallel to the magnetic field. The quadrupolar splitting $\Delta\nu$ was obtained from the doublet peaks. Corresponding images obtained using the selective storage precursor, shown to the right of each spectrum, demonstrate the selectivity of the experiment.

rate was recovered. The splittings were reproducible for all of the shear results presented here, so long as the sample did not begin to escape from the gap (thus destroying the shear field). In fact, disappearance of the splitting was a sure indication that the sample required reloading. Sample spectra are shown in Fig. 4.8. The interaction strength $\Delta\nu$ was obtained from each spectrum, as described in the next section, and is plotted in figure 4.9 as a function of reduced shear rate. The shear rates were calculated from the known inner cylinder rotation speed (see sec. 2.2.1) and confirmed by velocity microimaging. τ_d was taken from Ref. [58] to be 200 ms for 610K PDMS. Remarkably the ratios of $\Delta\nu$ for the X and Y directions are *precisely the opposite of those expected from the Doi-Edwards curves of Fig. 4.3.*

A possible explanation for these paradoxical results is that the oligomer probe does not

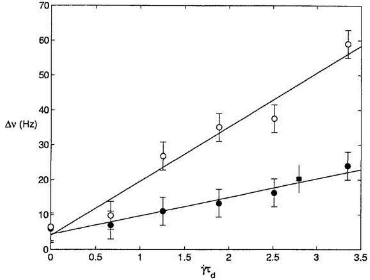

Figure 4.9: Quadrupole splittings $\Delta\nu$ versus reduced shear rate for 610K PDMS melt containing the ^{2}H oligomer at 10%, obtained with velocity direction (solid circles) and velocity gradient direction (open circles) parallel to the magnetic field. Also shown is the single data point from the neutral, vorticity direction (S_{ZZ}) experiment (solid square). The lines drawn through the data indicate that S_{YY} increases with De roughly twice as fast as S_{XX}, which is opposite to the result expected. The S_{ZZ} data point is consistent with the velocity direction data.

sample segmental alignment in the host matrix homogeneously, and the assumption that it reports a scaled order parameter averaged over all possible segmental orientations breaks down [48]. Furthermore the oligomer senses some inhomogeneous spatial distribution under shear, apparently concentration fluctuations in the velocity gradient direction, and on a length scale not significantly different from the host polymer average size. This suggests a smectic-like organization of polymer molecules into layers with a director along the velocity gradient direction, normal to the layers. There is little to support this suggestion, but it is consistent with neutron scattering experiments which yield, also paradoxically, a dependence on wave vector of the extinction angle χ [55, 56, 59]. If as this suggests the degree of alignment depends on the length scale being accessed, anomalous results would not show up in birefringence experiments which, in polymeric liquids, always measure spatially averaged segmental orientational order.

These unexpected results prompted a more complete study in the same melt using the now proven experimental methods and using a smaller guest probe molecule in which the nature of the motional averaging is not ambiguous.

4.6 Segmental alignment, C_6D_6 in the melt

Per-deuterated benzene (Aldrich, Steinheim, Germany) was dissolved in a volume of 610K PDMS melt at low concentration, approximately 10 wt %, in preparation for shear rate-dependence experiments. The melt was from the same batch as that used in the oligomer experiments. The probe is influenced by local steric effects, and is thus sensitive to local polymer segment orientation. It inherits some of the orientation present in the polymer when the matrix material is aligned in deformational flow. Because the probe molecule diffuses rapidly, it samples an ensemble-averaged order according to Eq. (2.4). This averaging is performed over a characteristic diffusion length determined by the benzene diffusion coefficient and the timescale associated with the quadrupolar interaction strength (a few tens of Hz). This distance, at several microns, is much larger than the molecular scale, so that the ensemble average of segmental alignment is indeed performed over a large number of polymer molecules.

Figure 4.10 shows a series of ^{2}H spectra acquired for a range of $\dot{\gamma}$ as indicated, in the region of the Couette cell in which the velocity axis X is aligned with the magnetic field direction. The different spectral widths reflect the particular values chosen for evolution time t_1 in the NMR experiment. The spectral width is 100 Hz for $t_1 = 5$ ms and 200 Hz for $t_1 = 2.5$ ms. As the shear rate is increased from zero the spectra exhibit a characteristic

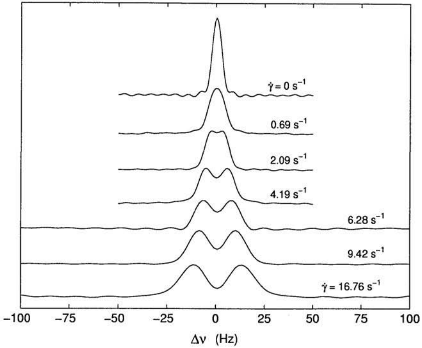

Figure 4.10: Spectra for S_{XX}, acquired using the pulse sequence described in section 3.3, at a range of shear rates for 610K PDMS melt containing the C_6D_6 probe at 10%, obtained with velocity direction parallel to the magnetic field. The width of the spectrum is determined by the evolution time t_1 in each NMR experiment.

broadening, and with further increase of $\dot{\gamma}$, a splitting into two distinct lines. The split peaks themselves have increasing width as the shear rate increases, an effect which we attribute to slight heterogeneity in the shear field leading to a distribution of splittings whose width is proportional to the average shear rate. Values for $\Delta\nu$ were extracted as follows. For the spectra with an observable splitting, $\Delta\nu$ was determined by estimating the position in frequency units of the peaks, as in Fig. 4.11, with an uncertainty of ±1 data point for each of the two maxima. With 128 points in the spectrum this corresponds to error of ±1.5 Hz for 100 Hz spectral width (0.78 Hz per point) and ±3 Hz for 200

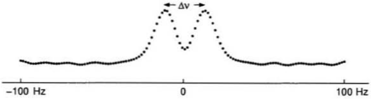

Figure 4.11: Determination of the quadrupolar splitting from two-dimensional spectra in the melt experiments.

Hz spectral width (1.56 Hz per point). Where clear broadening of the isotropic line was observed but not two distinguishable peaks, $\Delta\nu$ was taken to be the FWHM of the broadened line, minus FWHM of the zero shear, isotropic line. The uncertainty in the linewidth was assumed to be ±2 data points, or ±3 Hz for 100 Hz spectral width and ±6 Hz for 200 Hz spectral width. A corresponding set of data was acquired for the Couette cell region in which the velocity gradient direction Y was coincident with the magnetic field axis. The resulting spectra are shown in figure 4.12.

Typically, dynamical functions are plotted on logarithmic axes across several decades of time scale and the theory curves as presented in section 4.2.1 are in keeping with this. Since the experiments here do not cover several orders of magnitude, for comparison to experimental data it is also appropriate to plot the alignment tensor curves on a linear axis. Figure 4.13 shows the shear rate-dependence of the splittings obtained from the spectra shown in figures 4.10 and 4.12, for shear rates up to $\dot{\gamma} = 17\ \mathrm{s}^{-1}$. Each data point represents a single experiment. On the same graph are plotted the corresponding Doi-Edwards alignment tensor curves (equation (4.7)), fit to the data. The fits were carried out using nonlinear least-squares data fitting by the Gauss-Newton method, in Matlab and with two fitted parameters: (i) the scaling factor to match $\dot{\gamma}$ with reduced shear rate

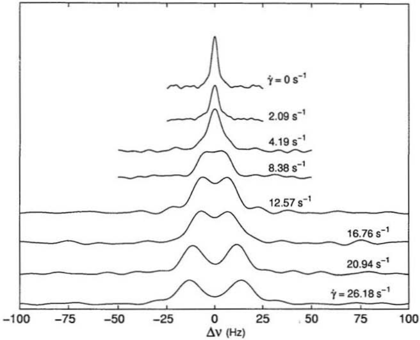

Figure 4.12: Spectra for S_{YY}, obtained with velocity gradient direction parallel to the magnetic field, at a range of shear rates for 610K PDMS melt containing the C_6D_6 probe at 10%.

$\dot{\gamma}\tau_d$, and (ii) scaling of the effective quadrupole interaction strength $\Delta\nu$ to the absolute alignment $S_{\alpha\alpha}$. The dashed lines are best fits for the individual S_{XX} (yielding $\tau_d = 412$ ms) and S_{YY} ($\tau_d = 204$ ms) data sets. While these fits do represent the data better than the single combined fit, the latter is the proper result since the model must apply to elements of the stress tensor simultaneously; the reptation time and the scaled order parameter are properties of the material and should not change between the two sets of experiments. The only two parameters which appear in the fits can be independently estimated, at least in order of magnitude.

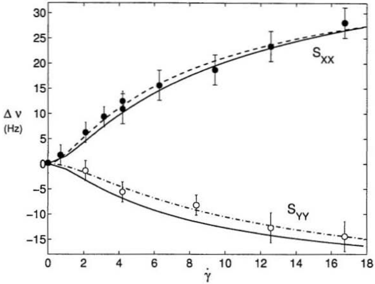

Figure 4.13: Quadrupole splittings $\Delta\nu$ vs. shear rate for C_6D_6 in 610K PDMS melt, for Couette cell regions corresponding to velocity (solid circles) and velocity gradient (open circles) parallel with $\vec{B_0}$. The lines are fits using the Doi-Edwards model in which the absolute splitting (vertical axis) is scaled to yield the pseudo-nematic order parameter and the horizontal axis is scaled to yield the tube disengagement time τ_d. The best compromise fit corresponds to $\tau_d = 330$ ms.

4.7 A closer look at the independent alignment approximation

The IA approximation is effectively a decoupling of the average over the isotropic distribution of unit vectors $\vec{u}$ (the average being indicated by $\langle\cdots\rangle_0$) in the following [6]:

$$Q_{\alpha\beta}(\boldsymbol{E}) = \left\langle \frac{(\boldsymbol{E}\cdot\vec{u})_\alpha\,(\boldsymbol{E}\cdot\vec{u})_\beta}{|\boldsymbol{E}\cdot\vec{u}|} \right\rangle_0 \frac{1}{\langle|\boldsymbol{E}\cdot\vec{u}|\rangle_0} - \frac{1}{3}\delta_{\alpha\beta} \simeq \left\langle \frac{(\boldsymbol{E}\cdot\vec{u})_\alpha\,(\boldsymbol{E}\cdot\vec{u})_\beta}{|\boldsymbol{E}\cdot\vec{u}|^2} - \frac{1}{3}\delta_{\alpha\beta} \right\rangle_0 \equiv Q^{(IA)}_{\alpha\beta}(\boldsymbol{E}) \tag{4.10}$$

Many theorists seeking to improve on the Doi-Edwards model have taken issue with this approximation [60, 61]. The DE model with independent alignment leads to a ratio (in limit as the stress goes to zero) of second to first normal stress difference $-N_2/N_1$ of $-2/7$, compared to $-1/7$ without the approximation. The value of $-1/7$ is more in keeping

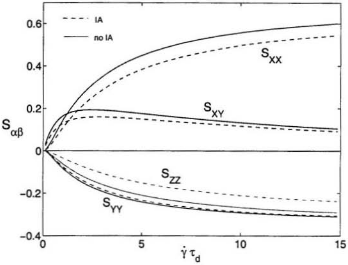

Figure 4.14: Solid lines are the $S_{\alpha\beta}$ in the DE model without the independent alignment approximation. Dashed lines are curves calculated using IA.

with available data, although recent measurements of normal stresses using more accurate optical methods indicate that the actual ratio may be larger in magnitude than 1/7 [62]. In any case, the approximation was introduced in the original Doi-Edwards model for mathematical convenience and has no physical basis. To investigate the consequences of the approximation the Doi-Edwards predictions were recalculated, this time without using IA, that is using the left hand side in equation (4.10) and not the right hand side. The next section describes specifically how this is carried out in the computation of $Q_{\alpha\beta}$. Discussion of the rest of the details of the numerical evaluation of the Doi-Edwards $S_{\alpha\beta}$ is deferred to section 4.9.1, where a correction to the theory is implemented.

4.7.1 Removal of IA approximation

In the model predictions presented thus far, the deformation tensor $Q^{(IA)}_{\alpha\beta}(\boldsymbol{E})$ appearing in Eq. (4.7) is that calculated according to the right hand side of Eq. (4.10). For example, $(\boldsymbol{E}\cdot\vec{u})_x = x + (t-t')\dot{\gamma}y$ using $\boldsymbol{E}$ from Eq. (4.9) for steady shear, and

$$Q^{(IA)}_{\mathrm{XX}}(\dot{\gamma}, t-t', x, y, z) = \left\langle \frac{(x+\dot{\gamma}(t-t')y)^2}{(x+\dot{\gamma}(t-t')y)^2 + y^2 + z^2} - \frac{1}{3} \right\rangle_0$$

is calculated as a function of the x, y and z Cartesian projections of the unit vector $\vec{u}(\theta,\phi)$. The isotropic distribution over the solid angle, $\langle\cdots\rangle_0$, is obtained by summing over the contributions to Q as the polar angle is varied in 20 steps over $0 < \theta \leq \pi$ and the azimuth in 20 increments over $0 < \phi \leq 2\pi$. The result is $Q^{(IA)}_{\mathrm{XX}}(\dot{\gamma}, t-t') \equiv Q^{(IA)}_{\mathrm{XX}}(\boldsymbol{E})$.

The independent alignment approximation is removed by performing the sum over the solid angle separately for $\dfrac{(\boldsymbol{E}\cdot\vec{u})_\alpha(\boldsymbol{E}\cdot\vec{u})_\beta}{|\boldsymbol{E}\cdot\vec{u}|}$ and $\dfrac{1}{|\boldsymbol{E}\cdot\vec{u}|}$, as indicated in Eq. (4.10), to arrive at $Q_{\alpha\beta}(\boldsymbol{E})$. For the Q_{XX} example,

$$Q_{\mathrm{XX}}(\dot{\gamma}, t-t', x, y, z) = \left\langle \frac{(x+(t-t')\dot{\gamma}y)^2}{\sqrt{(x+(t-t')\dot{\gamma}y)^2 + y^2 + z^2}} \right\rangle_0 \frac{1}{\left\langle \sqrt{(x+(t-t')\dot{\gamma}y)^2 + y^2 + z^2} \right\rangle_0} - \frac{1}{3}.$$

The results of the computations show that the approximation indeed matters. Figure 4.14 compares the "true" curves with those from Fig. 4.13 determined using the approximation. The difference without IA is mainly the enhancement of S_{XX} and S_{ZZ}, and a more pronounced maximum in the shear stress around $De \sim 1$. Whereas the simultaneous fits to S_{XX} and S_{YY} with IA consistently fall below S_{XX} and above (in magnitude) S_{YY} (see Fig. 4.14), the fit *without* the independent alignment approximation fits the data beautifully. The fit yields $\tau_{\mathrm{d}} = 260$ ms, and 64 Hz for the scaling of the splitting to S_{XX} and S_{YY}. The analysis in the rest of this chapter will be carried out using the DE model without the independent alignment approximation.

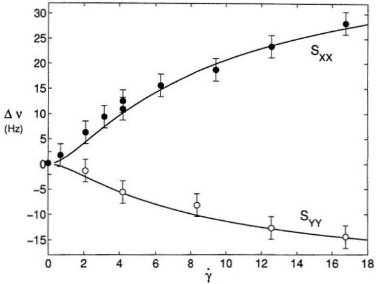

Figure 4.15: Fit of Doi-Edwards model without the independent alignment approximation to the S_{XX} and S_{YY} NMR data in the 610K PDMS melt. The fit without IA yields $\tau_d = 260$ ms.

4.7.2 Discussion of shear rate-dependence results

The value for $\tau_d = 260$ ms extracted from the best overall fit in figure 4.15 agrees within the uncertainties in the molecular parameters with that for uncross-linked polymers of high molecular weight, calculated according to [63]

$$\tau_d = \frac{a^2 \zeta_0 M^3}{M_e M_0^2 \pi^2 k_B T}. \tag{4.11}$$

Using the literature values [63] for the tube diameter a and the monomeric frictional coefficient ζ_0, Eq. (4.11) yields $\tau_d = 350$ ms. The fit also yields the pseudo-nematic order parameter, $\overline{P_2(\cos\theta_\alpha)}$, via

$$\Delta\nu = \left(\frac{3}{2}\frac{eV_{zz}Q}{h}\right)\overline{P_2(\cos\theta_\alpha)}S_{zz}. \tag{4.12}$$

The static quadrupolar coupling constant $\frac{eV_{zz}Q}{h} = 190$ kHz for C-D bonds in hexadeuteriobenzene [20], giving $\overline{P_2(\cos\theta_\alpha)}$ of 2.25×10^{-4}. This value is more than two orders of magnitude smaller than the scaled order parameter for deuterated benzene in liquid crystal polymers [64]. The flow-induced order in entangled polymers is much weaker than even the weakest equilibrium-state partially ordered systems.

4.8 Results: Angle dependence of segmental alignment tensor

In the Doi-Edwards description of the alignment tensor $S_{\alpha\beta}$, the relevant axis system is the hydrodynamic frame described respectively by the velocity (X), velocity gradient (Y) and vorticity (Z) axes. In order to relate Doi-Edwards theory to the case of the NMR quadrupole interaction experiment, this tensor must be transformed into the frame of the magnetic field,

$$R(\Theta, \Phi) \begin{pmatrix} S_{XX} & S_{XY} & 0 \\ S_{XY} & S_{YY} & 0 \\ 0 & 0 & S_{ZZ} \end{pmatrix} R^{-1}(\Theta, \Phi) \tag{4.13}$$

where the polar angle Θ defines the direction of the vorticity axis Z relative to $\vec{B}_0$, and the azimuth Φ defines the orientations of X and Y. In the horizontal Couette cell the vorticity (cylinder) axis is situated perpendicular to $\vec{B}_0$ and the projection along $\vec{B}_0$ is in the X-Y (velocity-velocity gradient) plane. The result is

$$S_{zz} = S_{XX}\cos^2\Phi - 2S_{XY}\sin\Phi\cos\Phi + S_{YY}\sin^2\Phi \tag{4.14}$$

for the diagonal tensor element representing the interaction strength measured in the NMR experiment. Note that this expression reduces to $P_2(\cos\Phi)S_{XX}$ for $S_{XY} = 0$, $S_{YY} = S_{ZZ} = -\frac{1}{2}S_{XX}$, i.e., when the deformation is uniaxial.

With the success of the shear-rate dependence experiments, an angle dependence study was undertaken immediately. The rate of shear was kept constant at $\dot{\gamma} = 12.6\,\mathrm{s}^{-1}$ while the

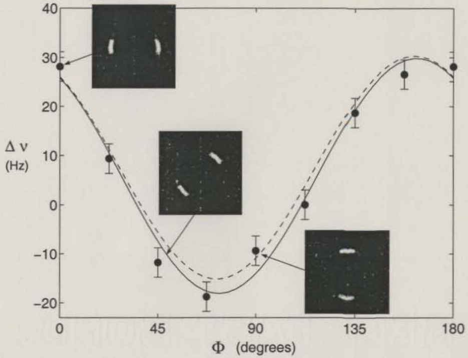

Figure 4.16: Quadrupole splittings $\Delta\nu$ versus orientation angle Φ at a fixed Deborah number of $\dot{\gamma}\tau_d = 4.15$. 0° corresponds to the velocity axis aligned with $\vec{B_0}$ and 90° to the velocity gradient axis aligned with $\vec{B_0}$. The solid line shows the predictions of the Doi-Edwards model, with the angular dependence as given by equation (4.2.2). The dashed line corresponds to a simple uniaxial transformation $P_2(\cos(\Phi - \chi))$. χ is the obtained extinction angle in each case. The images show the selected regions used to obtain $\Phi = 0°$, 45° and 90°.

orientation of the hydrodynamic frame with respect to the observation frame was varied through a number of prescribed angles. This was achieved by manipulating the relative strengths of the orthogonal gradients in the spatial selection technique. Effectively this comprised a "rheo-goniometer". The applied shear rate is nearly on the plateau for S_{XX} and S_{YY} (see Fig. 4.13) and corresponds to $De = 4.1$ so the conditions are just into the nonlinear region. The orientation angle is a severe test of the theory, and we set out in this set of experiments to determine χ via NMR.

The angular dependence of the splitting is shown in figure 4.16, along with the Doi-

Edwards curve calculated using equation (4.14). The agreement is very good, especially given that the value for χ is not fitted but is inherent in the model values of S_{XX}, S_{XY} and S_{YY} calculated for that shear rate. At this particular value of the reduced shear rate the extinction angle χ is predicted to be 16.9 degrees. This agrees well with optical measurements of extinction angle [60] χ where an angle of 17 degrees was observed at the equivalent Deborah number in a concentrated polystyrene solution. In order to gain some intuitive insight regarding the orientation of the polymer in the flow, we have shown plotted on figure 4.16 the fit for $P_2(\cos(\Phi - \chi))$ with $\chi = 17.7$ degrees from the fit. This theoretical curve also yields a quite reasonable value for the extinction angle but does not capture the depth of the data for the negative part of the curve. The $P_2(\cos(\Phi - \chi))$ curve is naively based on the assumption of an axially symmetric polymer deformation, whereas the Doi-Edwards formulation predicts a non-zero second normal stress difference $\sigma_{YY} - \sigma_{ZZ}$. The better fit to the data given by the Doi-Edwards model provides independent confirmation of the biaxial nature of the deformation and further support for the theory.

4.9 Modified DE: Convected constraint release

That it is formulated on the level of the polymer molecules, succeeds in the linear regime, correctly predicts nonzero N_1 and N_2 in the nonlinear regime which recommends it over previous viscoelastic models, and describes very well the nonlinear response following step shear, all lend credence to the Doi-Edwards theory. Still, in addition to the underprediction of the shear stress in the nonlinear regime, the model fails to correctly predict the ratio of second to first normal stress difference in shear [61]. The agreement of the predicted orientation angle χ [60] with the NMR data is very good here, for reduced shear rate $\dot{\gamma}\tau_d =$ 4 which is not yet into the plateau regime for the normal stresses. However the agreement is not as good for more complete birefingence data at shear rates which extend further into the nonlinear range. Several sophisticated modifications have been suggested to improve the model to achieve a more complete theory, including contour length fluctuations [65, 66], convected constraint release [8, 67, 68, 61] and non-affine tube deformation [61]. We chose to incorporate the convected constraint release modification first suggested by Marrucci [8], because the effect it accounts for should be important in the range $1/\tau_{\rm d} < \dot{\gamma} < 1/\tau_{\rm R}$ covered by our melt experiments.

The basic idea underlying convected constraint release is that the constraints to thermal motion, which arise from topological interactions with similar chains, are removed through non-thermal relative motion of the chains. The entanglements are themselves being convected away on the timescale of the flow. The constraints become released, providing an additional relaxation mechanism available to the chain.

CCR is incorporated into the Doi-Edwards model by assuming the thermal and convective relaxation processes act in parallel. This means that in Eqs. (4.7) and (4.3), the relaxation times τ are replaced with $\tau_{\rm CCR}$ where

$$\frac{1}{\tau_{\rm CCR}} = \frac{1}{\tau} + \dot{\gamma}\,\langle u_x u_y \rangle \tag{4.15}$$

for shear rate $\dot{\gamma}$ in the plane (x, y) [69]. The first term on the right in Eq. (4.15) is the relaxation rate for thermal motions (mainly reptation) through τ, and the second term on the right accounts for CCR through the rate of relative motion $\dot{\gamma}\,\langle u_x u_y \rangle$. $\langle u_x u_y \rangle$ is simply $S_{\rm XY}$ which we already calculate in the bare DE model. In slow flows where $\dot{\gamma} < 1/\tau_{\rm d}$ the convective term can be neglected and $\tau_{\rm CCR} = \tau$. The stress tensor will then be the same as that obtained using the bare DE. Where $\dot{\gamma}$ is comparable to $1/\tau_{\rm d}$ the convective term will be significant and the Doi-Edwards curves will be modified. At high shear rates $\dot{\gamma}$ will dominate, i.e. $\tau_{\rm CCR} \sim 1/\dot{\gamma} S_{\rm XY}$. In the latter case the relaxation rate becomes independent of even the longest relaxation time τ_d and is simply the rate of relative motion of neighbouring chains.

4.9.1 Details of the CCR implementation

The incorporation of CCR is subtle, and an understanding of exactly how the Doi-Edwards stress tensor is numerically evaluated is crucial. In our numerical evaluation, the reduced shear rate $\dot{\gamma}\tau_\mathrm{d}$ is stepped through a series of values and the $S_{\alpha\beta}$ are calculated for each value. Time dependence appears in both $\psi(t-t')$ and $Q_{\alpha\beta}(\boldsymbol{E})$ in the integral $\int_{-\infty}^{t} dt' \, \dfrac{\partial\psi(t-t')}{\partial t'} \, Q_{\alpha\beta}(\boldsymbol{E})$. The relaxation function

$$\frac{\partial\psi(t-t')}{\partial t'} = \frac{8}{\pi^2\tau_\mathrm{d}}\left(e^{-(t-t')/\tau_\mathrm{d}} + e^{-9(t-t')/\tau_\mathrm{d}} + \dots + e^{-81(t-t')/\tau_\mathrm{d}}\right)$$

is calculated over 50 points corresponding to a spectrum of relaxation times $\tau = (t-t')$ ranging from $\frac{1}{5}\tau_\mathrm{d}$ to $10 \times \tau_\mathrm{d}$. These are the discrete times over which $\psi(t-t')$ (or more precisely, its time derivative) is evaluated in the integral. The alignment tensor $Q_{\alpha\beta}$ also depends on history, through $\boldsymbol{E}$, and for each value of $\dot{\gamma}\tau_\mathrm{d}$ the strain history is evaluated over these same times,

$$\gamma = \int_{t'}^{t} dt'' \, \kappa(t'') = \dot{\gamma}\int_{t'}^{t} dt'' = (t-t')\dot{\gamma} = \dot{\gamma}\tau \,,$$

where the velocity gradient κ is just the shear rate $\dot{\gamma}$ and is constant for each step. In CCR the relaxation times are shortened depending on $\dot{\gamma}$ and on the current S_XY orientation state, according to Eq. (4.15). This effectively reduces the time over which the integral is taken. τ is changed to τ_CCR in both ψ and $Q_{\alpha\beta}$, and for each value of $\dot{\gamma}\tau_\mathrm{d}$ a new spectrum of relaxation times τ_CCR is calculated using S_XY from the previous step, with $S_\mathrm{XY} = 0$ for the first step. The multi-exponential function $\psi(t-t')$ now describes both thermal and convective relaxation. Note that τ_d remains implicit in the model and is still obtained from fitting to the alignment data.

The Doi-Edwards stress tensor elements calculated using this modification are plotted

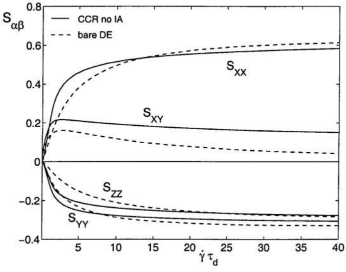

Figure 4.17: Predictions of the modified DE model (solid curves), incorporating CCR, for elements of the segmental alignment tensor $S_{\alpha\beta}$ as a function of reduced shear rate. Dashed curves indicate predictions of the bare DE model.

in figure 4.17. The bare DE curves are also shown for comparison. The most striking consequence of adding the additional, convective relaxation mechanism to the bare DE model is that above $\dot{\gamma} \sim 1/\tau_d$, the shear stress does not go to zero and instead heads towards a non-zero plateau. The plateau is still reached from above, and there remains a maximum in the shear stress near $\dot{\gamma} = 1/\tau_d$, but this maximum is very shallow. The calculated extinction angle χ is plotted in Fig. 4.18. In the convected constraint extension to the model the deformed polymer approaches alignment of ~ 10 degrees with the velocity direction at high shear. This is dramatically different from the asymptotic zero degree alignment for the bare DE model, and is much more in agreement with χ observed in the NMR experiments here and in birefringence.

The physical explanation for the recovery, in CCR, of the experimentally well-documented behaviour of the shear stress is the following [61]. Without CCR, for $De > 1$ the tubes become aligned along the shear direction faster than they can reform, an individual chain feels less traction from neighbouring chains, and the shear stress decreases towards zero. The reptation relaxation mechanism is "frozen out" at high shear rates [61]. Conversely, the convective relaxation is itself proportional to $\dot{\gamma}$, and so it does not saturate at high shear rates. Tubes are convected away by the same flow which aligns them, full alignment is suppressed and the shear stress remains high. The external deformation can never completely align the molecules. The quite different asymptotic values for χ in Fig. 4.18 emphasize this point.

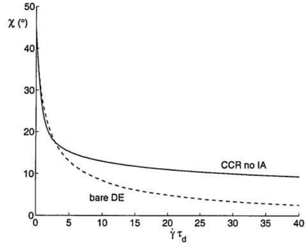

Figure 4.18: Prediction of extinction angle $\chi(\dot{\gamma}\tau_d)$ for the modified DE model with convected constraint release (solid curve). The dashed line indicates the theoretical χ for the bare DE model.

With CCR incorporated into the model there is very little difference qualitatively in the fit to the data. Figure 4.19 shows the same S_{XX} and S_{YY} data for the deuterated benzene in the melt presented earlier, with fits for both the CCR-modified theory and the original DE theory for comparison. Over this range of shear rates the effect of convected

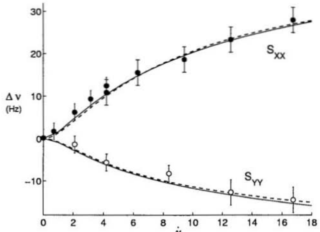

Figure 4.19: Solid line represents the fit using CCR-modified theory, while the dashed line is the fit using the original DE theory. Over this shear range the curves represent the data equally well, the difference being the scaling in the absolute alignment.

constraint on the alignment is mainly quantitative, increasing the scaling of the NMR interaction strength to the absolute alignment. This scaling is 100 Hz with CCR, and 64 Hz without.

4.10 Very high shear in the melt

The shear rate-dependent alignment experiments were carried out in the melt up to the highest shear rate attainable. Figure 4.20 shows the S_{XX} and S_{YY} data over all $\dot{\gamma}\tau_d$ values accessed. There appears to be some perturbation in in the data occuring above $\dot{\gamma} \sim 20\ \mathrm{s}^{-1}$. These higher rates also correspond to shear driven directly by the motor as opposed to via one of the gear boxes, and so the nominal driving frequencies were checked and found to be correct. In any case an error in calibration of the motor speed would be expected to affect the absolute alignment data similarly; such an error would be equivalent to a shift along the $\dot{\gamma}$ axis, and since both S_{XX} and S_{YY} are monotonically increasing curves one expects enhancement or suppression of both. Instead the S_{XX} data appear to show the absolute alignment suppressed slightly, while the S_{YY} data reflect enhanced NMR interaction strengths.

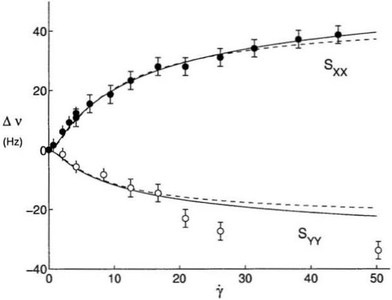

Figure 4.20: S_{XX} and S_{YY} NMR data over the full shear range. Also shown are curves for DE theory with CCR (solid line) and without (dashed line), calculated using the parameters for the fits to $\dot{\gamma} < 20\ \mathrm{s}^{-1}$ data and extended to $\dot{\gamma} = 50\ \mathrm{s}^{-1}$.

Extending the fitted curves appearing in Fig. 4.19 to $\dot{\gamma} = 50\ \mathrm{s}^{-1}$ and plotting them through the full shear data at first appears to remove half of the mystery. The theoretical curve for S_{XX} with convected constraint release (solid curve) falls squarely through the high shear data. The corresponding curve from the original DE model (dashed curve) deviates from the data above $De \sim 5$, that is, well into the plateau region where convected constraint release modifies the theory significantly. However, the apparent better fit with

CCR incorporated should be interpreted with caution, and cannot be said to reinforce the CCR-modified Doi-Edwards theory. Clearly there is some puzzling behaviour in S_{YY} at $\dot{\gamma} \gg 1/\tau_{\rm d}$, where the system is far from equilibrium. The theory must agree for all elements of $S_{\alpha\beta}$ simultaneously, and it was intended that the high shear behaviour in this melt would be revisited. Unfortunately the remaining volume of the 610K PDMS on which the results of this chapter were obtained was accidentally destroyed. The question of whether the anomaly in the high shear S_{YY} data is of physical origin, for example a large length scale perturbation arising from supra-molecular structure, or contour length fluctuations which are thought to become important once $\dot{\gamma} \sim 1/\tau_{\rm R}$; or reflects a systematic problem in the shear experiment, could not be pursued in this sample. How far the theory applies into $\dot{\gamma} \gg 1/\tau_{\rm d}$ remains an open question.

Another doctoral student, Ryan Cormier, is currently using the methods and analysis developed here to investigate further the predictions of the Doi-Edwards theory, in particular extended to several molecular weights of PDMS melts and obtaining the complete segmental alignment over the full shear range, addressing the important issue of molecular weight-dependence of dynamics in entangled polymers.

Before closing this chapter it is worth noting that the real success of these results is that they reproduce the broad characteristics of the predicted Doi-Edwards stress tensor, and do so more successfully when the independent alignment approximation is removed from the model and convected constraint release incorporated. The theoretical extinction angle is then in excellent agreement with that determined experimentally. While the agreement of the modified Doi-Edwards theory with the NMR data is convincing, the story is by no means complete. No account has been made here for possible effects of polydispersity. The results from the oligomer in the melt, and the S_{YY} (alignment along velocity gradient) data from the benzene probe at very high shear rates, are curious and certainly invite further study.

The following chapter will again see the spatially selective rheo-NMR technique, with a different molecular model and different analysis, applied to the problem of a less flexible, rod-like liquid crystal polymer in extensional flow.

5 Director dynamics in liquid crystal polymers under extension

The discussion until now has been focused on polymeric liquids which, like almost all liquids, are isotropic in the equilibrium state. This chapter will present results for an anisotropic liquid under extensional and shearing flow fields. Linear, semi-rigid polymer molecules have an elongated rod-like shape, and in the right conditions may align spontaneously along a common direction, exhibiting characteristics of nematic liquid crystals [9]. They have long range one-dimensional orientational order, but positional disorder with no long range order in their centres of mass so that they flow like liquids. This class of molecules is called liquid crystalline polymers.

Both isotropic, flexible polymers and liquid crystalline polymers (LCPs) exhibit fast chain isomerizations. They differ in the nature of the slower dynamics which determine the degree of residual orientational order: rigid body tumbling (rotational diffusivity) in the case of rod-like polymers, compared to segmental reorientation in melts of flexible polymers.

This chapter of the thesis will present results of extensional flow experiments on a main-chain liquid crystal polymer, PBLG, interpreted on the basis of the Leslie and Ericksen molecular model [12, 13, 70]. The Leslie-Ericksen theory describes the dynamics of liquid crystal rod-like polymers in terms of evolution of the director due to viscous torques. Viscous torques arise from body forces associated with magnetic or electric fields, or from coupling with the flow field; each of these effects will be described in turn in section 5.1 below. Elastic torques are not accounted for in this model. The approach here was to use the selective storage method described in chapter 3 to perform localized spectroscopy, sensitive to molecular orientation, to monitor the development of the director orientation for a lyotropic liquid crystal polymer in pure planar extension; and to compare the results to predictions arising from the torque balance equation solved for this geometry. Additionally, bulk shear experiments were carried out in the cone and plate and vertical Couette geometries, to explore further the director dynamics and the consequences of the theory. These studies reveal some key information about the dynamics of this model liquid crystal polymer, and by extension of rod-like polymers in general.

5.1 Liquid crystal polymers

A liquid crystal may be thermotropic, in which case the nematic-isotropic transition is thermally driven, or it may lyotropic, where the concentration of the LCP in solution determines its phase character and degree of anisotropy. The critical temperature or concentration depends on the aspect ratio (ratio of length to diameter) of the polymer molecules and hence on molar mass. The degree of alignment in a magnetic field also depends on concentration. Once established, the anisotropy in lyotropics increases with the concentration, as the rods become more closely packed and their rotational diffusional motions further hindered.

The anisotropy of the nematic phase is characterized locally by a director $\vec{n}$ about which the time-averaged motion of the long axis of the molecule is cylindrically symmetric. While the shape of the molecule and the concentration determine the existence of the director in lyotropic liquid crystals, external fields and long range interactions determine its orientation. The macroscopic order parameter $S = \langle \vec{n} \cdot \vec{n} - 1/3 \rangle$ describes the degree of alignment of the director orientations about a common direction. Locally, a molecule has interactions with neighbouring rods, so that there is some domain over which a local director $\vec{n}$ is defined. The domain size can be thought of as correlation length for local director orientation. In polymer liquid crystals this is usually 1-10 μm [71]. The local director $\vec{n}$ assumes random orientations throughout a bulk sample and has no preferred orientation with respect to length scales much larger than the molecular length. In a sample size of millimeter dimensions one expects a random, isotropic distribution of local directors. The result is a poly(liquid crystalline) sample, with net order parameter $S = 0$. A single-crystal, monodomain state can be induced by magnetic, electric or hydrodynamic fields, or strong elastic effects tending to align the director orientation at surfaces.

Where a magnetic interaction is present the magnitude of the body force is given by

$$\vec{h} = \frac{\chi_a (\vec{n} \cdot \vec{B_0}) \vec{B_0}}{\mu_0} \tag{5.1}$$

where $\vec{B_0}$ represents the magnetic field and $\mu_0 = 4\pi \times 10^{-7}$ T·m/A is the permeability of free space. $\chi_a = \chi_\perp - \chi_\parallel$ is the anistropy of the magnetic susceptibility of the liquid crystal polymer, and is dimensionless. A non-zero value for χ_a results from a non-spherical distribution of atoms in the molecule. In nematics χ_a is usually positive, resulting from slightly prolate rods, and the local directors tend to align with $\vec{B_0}$. In PBLG χ_a is positive but not large: it is usually $\sim 10^{-7}$ for flexible, long chain molecules [72], however the tendency to align is strong because of the number of polymers present and because of long range cooperativity.

The director tends strongly to match its alignment with the orientation of the surface, and there will exist spatial gradients in the director over a region extending $\xi = (K/\chi_a)^{1/2}\mu_0/B_0$ from the wall into the liquid [72]. K is the Frank elasticity constant, and here the approximation is made that the splay, bend and twist elastic constants are approximately equal ($K_1 \simeq K_2 \simeq K_3 = K$) [72]. For $K \sim 10^{-11}$ N and $\chi_a \sim 10^{-7}$, the magnetic correlation length ξ is less than 1 micron in a 7 T magnetic field. Thus surface-induced orientational order does not penetrate very far into the sample in the rheo-NMR cells, which have millimeter to centimeter scale dimensions. Surface elastic effects are negligible in these studies, particularly since the signal is obtained from the stagnation region of the four roll mill, away from the roller surfaces.

The walls separating domains of uniform alignment also have width roughly equal to the magnetic correlation length ξ. Over this length the director changes orientation abruptly, from its orientation in one domain to that in a neighbouring one, and elastic effects are important here. Such regions of large spatial gradients in $\vec{n}$ are called orientational defects, and a high density of orientational defects results in a *textured* sample.

5.1.1 Viscous torques and the Leslie-Ericksen theory

When a polydomain sample is placed in an external field, each of the rod-like molecules experiences a body force as a result of coupling with the field. The local director experiences a viscous torque per unit volume $\tau = \vec{n} \times \vec{g}$ where $\vec{g}$ is the field-induced body force. If the external field is small, those domains having magnetizations nearly along the applied field will have their domain sizes grow. A stronger field causes rods in all domains to rotate coherently and align together with the applied field. Moderate ($B_0 \sim 0.2$ T) magnetic field strengths can transform random liquid crystalline textures into uniform, monodomain samples [73]. The molecules can also be aligned by surface interaction in thin samples contained between parallel plates. In a monodomain sample the director orientation is also the optic axis.

The molecules comprising the domain walls reorient more slowly. Optical studies, sensitive to mesoscopic length scales, have shown that equilibrium alignment along the magnetic field is restored within ~ 1 s for main chain LCPs such as PBLG, while disappearance of the domain walls and full recovery of the monodomain state may take minutes [7].

The coupling to an applied velocity field leads to another, competing body force, and hence another source of director reorientation [7]. Leslie and Ericksen account for the competing magnetic and hydrodynamic torques by writing the total body force as [9, 12, 13]

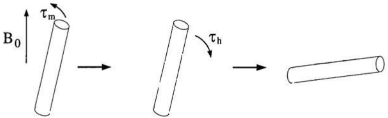

Figure 5.1: Competing magnetic and hydrodynamic torques experienced by a rod-like liquid crystal polymer, illustrated for the example of planar extensional flow.

$$\vec{g}_{\mathrm{tot}} = \vec{h} - (\alpha_3 - \alpha_2)\,\vec{N} - (\alpha_5 - \alpha_6)\,\boldsymbol{D}\cdot\vec{n} \tag{5.2}$$

where $\vec{N} = \dot{\vec{n}} - \boldsymbol{\omega} \times \vec{n}$ is the rate of change of the director with respect to the background fluid, and $\boldsymbol{D}$ and $\boldsymbol{\omega}$ are the symmetric and antisymmetric parts of the deformation tensor and are specific to the geometry of the flow field. They are also called the strain-rate and vorticity tensors, respectively, and are written in terms of the velocity gradient tensor from

Eq. (1.1):

$$\boldsymbol{D} = \frac{1}{2}\left(\kappa_{\alpha\beta} + \kappa_{\beta\alpha}\right), \quad \boldsymbol{\omega} = \frac{1}{2}\left(\kappa_{\alpha\beta} - \kappa_{\beta\alpha}\right).$$

The theory contains the parameters α_i, which have dimensions of viscosity (Pa·s) and are generally called the *Leslie viscosity coefficients.* The first term in Eq. 5.2 is the magnetic orienting term, the second term represents stress due to dissipation by rotation of the director in the background fluid, and the last term represents stress due to dissipative losses by conventional viscous effects. In an extension to the theory, Parodi showed that $\alpha_6 = \alpha_2 + \alpha_3 + \alpha_5$ [74], so that $(\alpha_5 - \alpha_6)$ may be replaced with $(\alpha_2 + \alpha_3)$ in Eq. 5.2.

Dynamic equilibrium requires a balance of bulk torques applied to the director, leading to the torque balance equation:

$$\vec{n} \times \left[\vec{h} - (\alpha_3 - \alpha_2)\vec{N} - (\alpha_3 + \alpha_2)\boldsymbol{D}\cdot\vec{n}\right] = 0. \tag{5.3}$$

Each of the x, y and z components of the cross product in Eq. (5.3) must be identically zero. The solutions provide information about the conditions for stable director orientation, as a function of the macroscopic flow parameter $\dot{\mathcal{E}}$ or $\dot{\gamma}$, and will depend on the geometry of the experiment.

What do the Leslie viscosity coefficients mean? In the Leslie-Ericksen framework, nematics are classified in terms of their aligning characteristics in flows. The viscosity coefficients important for director alignment are α_2, α_3 and α_4 [7]. α_2 corresponds to the hydrodynamic torque transmitted to the director via the surrounding fluid; it is always negative corresponding to clockwise rotation, for the standard description of velocity positive along the x direction. α_3 describes the torque transmitted by the background fluid to a director aligned in the flow direction, and α_4 is responsible for the viscous drag when the director is aligned along the vorticity direction. The sign of α_3/α_2 determines the behaviour of the nematic director in shear flow. The director will have no steady state

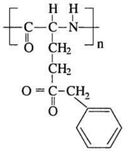

Figure 5.2: Mesogenic unit of γ-benzyl-L-glutamate, or PBLG.

solution and will be tumbling if $\alpha_3/\alpha_2 < 0$, i.e. if α_3 is positive. Since in preliminary experiments the PBLG nematic solutions displayed flow alignment, we assume here that α_2 and α_3 are both negative. It is also assumed that $|\alpha_2| > |\alpha_3|$, and in fact $|\alpha_2| \gg |\alpha_3|$ for LCPs in general [7].

5.2 Liquid crystal polymer: PBLG

PBLG is poly(γ-benzyl-L-glutamate). This main chain liquid crystal polymer was first synthesized over fifty years ago, in an effort to produce synthetic fibers with the desirable characteristics of natural fibers such as wool. There is special interest in this polypeptide because it was the first synthetic polymer to exhibit a liquid crystalline phase [75]. It has seen extensive use as a model lyotropic LCP because of its availability, stability and good solubility properties. PBLG is a long chain polymer whose mesogenic unit, shown in Fig. 5.2, is a derivative of the amino acid *glutamic acid*. The L indicates left-handed chirality and the side chains contain terminating benzyl groups. The aromatic rings hanging off the chain in PBLG are stiff and lend rigidity to the very flexible chain backbone. The benzene side rings have a tendency to stack one on top of another in solution, and this feature is thought to be important to the molecule's self-organizing ability.

PBLG and its chiral analogue, PBDG, are left- and right-handed enantiomers of the same molecule. In solution, PBLG and PBDG molecules form helices of opposite sense, and if one or the other is present in sufficient concentration a cholesteric liquid crystal results. In a racemic mixture of both enantiomers, generally called PBG, the cholesteric effects cancel and the mixture behaves as a nematic. In other solvent configurations PBLG alone is known to be rod-like [76]. It was shown early in the history of PBLG that in a magnetic field of moderate strength the cholesteric mesophase transforms to a nematic mesophase as a result of the positive diamagnetic anisotropy of the molecules [77]. The ability to align the mesophase by B_0 is field strength dependent, scaling with the square of the field strength, as will be shown in Sec. 5.5.1. Electric fields are also capable of producing a nematic state from a cholesteric one [78], with the large dipole moment rather than the magnetic anisotropy providing the mechanism for aligning the optic axis with the field. As well, in rheological experiments there seems to be only nematic character exhibited under shear, with no evidence of the cholesteric behaviour [79, 80]. Evidently in strongly orienting fields, the PBLG helix unwinds and behaves like a semi-rigid molecule.

The physical properties of PBLG in solution, such as elastic constants and rotational viscosity, depend very strongly on molecular weight, concentration, and the particular solvent(s) used [76, 81]. Because of this complex dependence it is difficult to make absolute comparisons among the many published results on the liquid crystalline nature of PBLG.

5.3 Previous studies

As stated earlier, PBLG has been used extensively as a model lyotropic LCP, and for this polymer nematic alone there is a large body of experimental results, which reveal the very subtle and complex behaviour of these systems at rest and under deformation. Early studies of magnetic orientation [82] and diffusion [83] in PBLG solutions in the quiescent state reported their anisotropic, nematic character. The director reorientation which occurs when a uniformly-aligned sample is subjected to a magnetic field aligned perpendicular to the director $\vec{n}$ is known as the dynamic Fréedericksz transition [84]. A similar situation results under an applied electric field if the nematogens have non-zero dielectric anisotropy, and the Fréedericksz transition has been studied extensively, usually to gain information about rotational viscosity $(\alpha_3 - \alpha_2)$ and (where the magnetic or electric fields are small) twist elastic constants.

In mechanical rheometry studies, domains are seen to appear and disappear under shear and this effect is well-documented. Kiss and Porter [79] found the unusual result of negative first normal stress difference, over a range of intermediate shear rates. The shear region of negative first normal stress difference N_1, corresponded to the apparent development of banded textures normal to the shear direction. In highly-concentrated (35 wt %) solutions of PBG in m-cresol, a hexagonal phase has appeared in magnetically oriented films [85] and, in recent x-ray scattering studies, under shear [86]. *In situ* small angle neutron scattering studies of a side-chain liquid crystal polymer in cone and plate shear showed the development of smectic layers oriented parallel to the shear plane [87]. The evolution of shear-induced texture in a tumbling nematic starting from a surface-aligned monodomain has been studied by Yan and Labes [88] via optical microscopy, and explained by the balance of elastic forces in the liquid crystal with the viscous forces generated under shear. In studies of the dynamic Fréedericksz transition carried out in the overwhelmingly larger magnetic field, the reorienting director is never seen to rotate out of the plane containing the initial director orientation and the magnetic field [89, 90]. In the analysis here it is assumed the director is confined to the plane containing the primary direction of deformation ($\dot{\mathcal{E}}$ or $\dot{\gamma}$) and $\vec{B}_0$.

There is a consensus among rheologists that texture does develop in liquid crystal polymer solutions under shear [79, 86, 87, 88], and also that there is refinement of the texture from the mesoscopic to the molecular length scale at very high shear rates [71]. The effects are often erratic and are probably extremely sensitive to initial orientation conditions and to the solution properties in lyotropics. The textured, sometimes periodic instabilities have been observed under a broad range of circumstances, and have important consequences for the final orientation state in processing. Significant progress has been made in modeling the observed patterns, treating them as nonlinear, dissipative structures [89, 91, 92], and this line of investigation continues to generate a great deal of interest [93]. Several years ago Meyer and coworkers [92] were the first to recognize that the apparent periodic distortions observed under director reorientation could be treated as examples of dynamic periodic order which often arises in systems driven far from equilibrium. They derived a relationship between the growth rate and the wavelength of the spatial modulation. Using this analysis, Schwenk *et al.* [89, 90] have investigated director reorientation in a deuterated side chain liquid crystalline polymer. They obtained ^{2}H NMR spectra under continuous sample rotation in the magnetic field, as well as complementary optical microscopy pictures by quenching the sample at the angles corresponding to the NMR spectra, thus gaining access to both mesoscopic and molecular length scales. Their results show that even after initial director reorientation with the magnetic field, indicated by NMR spectra, there remain walls separating the oriented domains which the authors treat as convective, dissipative structures amenable to the wavevector analysis.

Burghardt [71] presents a microstructural tumbling model for nematic liquid crystals, based on the polydomain model of Larson and Doi [94], to describe rigid rod polymers in shear flow. Their model was developed for situations where the polydomain state prevails: when a starting monodomain state is difficult to achieve experimentally, or during processing stages where a starting monodomain state is simply not possible. Thus elastic effects must be important in this model; they provide the restoring torque needed to suppress tumbling under flow conditions. This model has been successful in capturing flow-induced orientation effects in these situations. In the present case, the Leslie-Ericksen model is appropriate for several reasons. First, unlike optical microscopy studies in which sample cells are necessarily thin and wall effects are important, magnetic resonance studies do not have the optical transparency criterion and our rheometric cells contain bulk samples in which wall effects may be safely neglected. Second, the ever-present, strongly orienting magnetic field in NMR experiments overwhelms the much smaller elastic torques generated. Elastic effects that complicate liquid crystal hydrodynamics are much less important here than magnetic and hydrodynamic orienting fields, and the magnetic orienting field provides the restoring torque to suppress tumbling in flow. Third, the torque balance equation in the Leslie-Ericksen model is essentially an equation for dynamic equilibrium of the director $\vec{n}$, and our NMR experiments are directly sensitive to director orientation. The Leslie-Ericksen model contains the basic elements appropriate for situations where large magnetic and hydrodynamic viscous torques dominate elastic torques, and we use it in this work. In doing so we limit study of the viscosity coefficients to those which appear in the torque balance equation, α_2 and α_3, and we measure them indirectly in several different NMR experiments. Specifically, we study director orientation as a function of:

·extension or shear rate, at steady state

·time following onset of shear/extension ("start-up" experiments)

·time following cessation of $\dot{\mathcal{E}}$ or $\dot{\gamma}$ (relaxation experiments).

The viscosity coefficients for a side-chain lyotropic liquid crystal polymer under shear have been measured in a cone and plate apparatus by Grabowski *et al.* [24, 95], with the results obtained via NMR spectroscopy and analyzed in the framework of the Leslie-Ericksen theory. These studies showed a change in director orientation with shear rate, in agreement with the model for flow-aligning nematics, and established that rheo-NMR experiments could be used to obtain the viscosity coefficients which appear in the model. The theory has been applied by Callaghan in [96] to the interesting case of extensional flow around a stagnation point in the plane perpendicular to $\vec{B}_0$, where instead of a continuous change in director orientation with shear rate the model predicts a sudden flip in director orientation at a critical velocity gradient or extension rate $\dot{\mathcal{E}}_c$. Flows in which there is a stagnation point are important because as the molecular trajectories approach the stagnation point, the residence time of the polymer chains in the velocity gradient diverges and the chains may be stretched far from equilibrium [97]. The motivation for these experiments was initially to test this prediction of a critical extension rate. Other physically important consequences of the model are explored as the rheo-NMR results on PBLG are presented in the following sections.

5.4 Quiescent state experiments

All PBLG and PBDG materials were obtained from Sigma Chemical Co., St. Louis, MO. Because of the volumes involved in the rheometric cells, three different sample preparations were used to complete these experiments. This was a practical matter of availability and all samples were of similar molecular weight. From the standpoint of the rheometric experiments, all carried out in the presence of the large magnetic field, there is essentially no difference between PBDG and PBLG solutions of sufficient concentration since both will behave as nematics. All samples for the rheometric experiments were prepared at 20 wt %. They are listed in table 5.1. High purity solvents were obtained from Fisher Scientific, Pittsburgh, PA, and were used without further purification. PBLG polymers were dissolved in a 52/48 w/w mixture of dioxane and nitrobenzene, following the preparation of Yan and Labes [88]. The magnetic and flow fields considered here are large, and the spectra observed under extension and in the quiescent state reflect a purely nematic state for the molecules.

PBLG308	Cat. P-5136	MW 296 100 (vis)	308 000 (LALLS)
PBDG222	Cat. P-3388	MW 200 200 (vis)	222 200 (LALLS)
PBLG277	Cat. P-5136	MW 296 000 (vis)	277 700 (LALLS)

Table 5.1: Poly(γ-benzyl-glutamate) molecular weights used in sample preparations.

Initially, deuterated versions of both solvents were used in the samples to act as reporter molecules in the NMR experiments. These two solvent molecules are both single-ring structures which will have dynamics and mobility very similar to that of the benzene probe molecule used in the melt experiments. They sample a large number of polymer rods on the time scale of the NMR experiment, so that they report on the averaged local director orientation, with the order parameter very much reduced by their motions. The deuterons of dioxane-d_8 are equivalent, and the doublet corresponding to the dioxane deuterons was

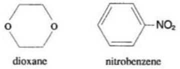

Figure 5.3: Solvents used in the PBLG solutions for liquid crystal polymer studies.

well-resolved in early extension experiments. To simplify interpretation of the spectrum all subsequent experiments were carried out with only the dioxane solvent deuterated.

For all NMR spectroscopy experiments on the liquid crystal polymer, the samples were allowed to reach the magnetically aligned, single crystal state before beginning experiments. The signal was obtained following a quadrupole echo sequence to obtain the director orientation via the strength of the deuterium quadrupole interaction.

The lyotropic character of PBLG was examined by studying the concentration dependence of the degree of order measured in the NMR spectrum. The 300 μL samples were prepared by increasing the concentration of the polymer powder in a beginning stock solution of 4% w/w PBLG in the dioxane / nitrobenzene mixture. There is an estimated uncertainty of ± 1 wt % associated with each concentration due to the difficulty of controlling evaporation of the solvents during sample preparation. The spectra obtained are shown in figure 5.4. At lower concentrations the spectra are characteristic of an isotropic liquid state, exhibiting a single Lorenzian-shaped line.

The temperature and concentration characterization experiments were conducted using a spectrometer specialized for wide line NMR studies, which is not equipped for online adjustment of shim coils to correct minor spatial inhomogeneities in the B_0 magnetic field, essential for obtaining a high resolution spectrum. The rest of the experiments presented in this chapter were carried out on the AMX300 spectrometer which was used for all of the melt experiments and which is equipped with adjustable shim coils. The linewidth and line shape of the PBLG spectra will be discussed below in relation to those more highly resolved, higher quality spectra.

The spectra at 7% and 10% concentrations show two peaks. This is not a quadrupolar doublet but two isotropic lines corresponding to the two solvents which have different chemical shifts, and their separation scales with the strength of the magnetic field. The two lines should also appear in the 4% spectrum but are not well-resolved there. Solutions at 15% w/w or greater exhibit splittings of the isotropic lines into doublets. Figure 5.4 shows that in PBLG at this molar mass the isotropic-to-nematic transition occurs between 10% and 15%. For the rheo-NMR experiments to follow, the concentration of samples was always above 15% to ensure the nematic state.

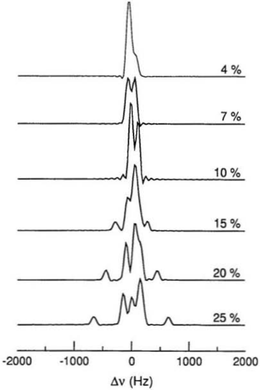

Figure 5.4: Spectra for different concentrations of PBLG in dioxane-d_8, nitrobenzene-d_5 at 25°C in the quiescent state. The nematic phase is seen to set in at between 10% and 15%.

Temperature effects can also be important in lyotropics. The temperature dependence of PBLG at 30% concentration (well above the isotropic-nematic transition) is shown

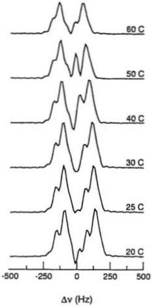

Figure 5.5: Spectra for different temperatures of PBLG at 30% concentration in dioxane-d_8 / nitrobenzene, in the quiescent state. Over this temperature range there is no observable dependence on temperature of the nematic state at rest.

in figure 5.5. The nematic ordering is insensitive to temperature over this range. A thermotropic nematic-to-isotropic transition is expected in PBLG solutions, somewhere above 60° [98], depending on the concentration and molecular weight. Fig. 5.5 indicates that the static behaviour of this LCP is insensitive to temperature over this range; however it tells us nothing about possible temperature dependence of the dynamics. For example the viscosity will almost certainly decrease due to increased thermal motions at elevated temperatures. It is important to control the temperature during experiments on lyotropics, and all of the shear and extension experiments discussed below were carried out at 25°C.

The selective spectroscopy technique outlined in chapter 3 was used to perform ^{2}H NMR experiments under planar extension in the four roll mill. Observations were limited

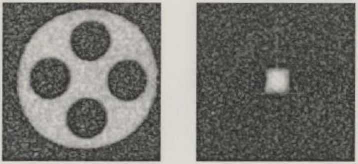

Figure 5.6: ^{2}H NMR images in the four roll mill, obtained on 20% PBLG solution. An image of the entire sample at left shows the four roll mill on cross-section. At right, the selection technique is used to define within the cross-section a (4 mm)^2 region around the stagnation point, on which ^{2}H NMR spectroscopy experiments are performed.

to the stagnation zone, away from the roller surfaces, with the underlying assumption that in this region the description of section 2.2.2.1 applies and the velocity gradient is uniform. For the first sets of experiments a square region of side length 4 mm was selected, oriented at 45° to the extension axis.

5.5 Experiments measuring the Leslie coefficients in planar extension

5.5.1 Analysis: nematic LCP in four roll mill

The director for four roll mill planar extension in the plane perpendicular to B_0 is represented in figure 5.7, in polar coordinates. The body force $\vec{h}$ is

$$\vec{h} = \frac{\chi_a(\vec{n} \cdot \vec{B_0})\vec{B_0}}{\mu_0} = \left[0,\ 0,\ \frac{\chi_a B_0^2 \cos\theta}{\mu_0}\right]$$

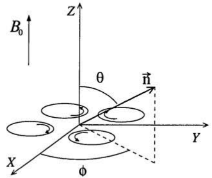

Figure 5.7: Geometry of the director reorientation in the four-roll mill extensional flow field, for extension along the x axis and compression in the y direction. The shaded region represents the nematic liquid crystal polymer solution. The (exaggerated) local director is represented in spherical polar coordinates.

where $\vec{B_0} = [0,\ 0,\ B_0]$ and $\vec{n} \cdot \vec{B_0} = B_0 \cos\theta$ have been used.

The symmetric and anti-symmetric parts of the deformation tensor are

$$\boldsymbol{D} = \begin{bmatrix} \dot{\mathcal{E}} & 0 & 0 \\ 0 & -\dot{\mathcal{E}} & 0 \\ 0 & 0 & 0 \end{bmatrix}, \quad \boldsymbol{\omega} = 0.$$

The sign of $\dot{\mathcal{E}}$ depends on the sense of rotation of the rollers, and here $\dot{\mathcal{E}} > 0$ is arbitrarily taken to correspond to extension $\dot{\mathcal{E}}$ along the x axis and compression in the y direction. For opposite sense of rotation the hydrodynamic frame is merely rotated by 90 degrees in the (x, y) plane and the same description applies.

The solution of the torque balance equation for the z-component leads to [22]

$$(\alpha_3 - \alpha_2)\,\dot{\phi}\sin^2\theta = \dot{\mathcal{E}}\,(\alpha_3 + \alpha_2)\sin^2\theta\sin\phi\cos\phi$$

and therefore

$$\dot{\phi} = \dot{\mathcal{E}}\left(\frac{\alpha_3 + \alpha_2}{\alpha_3 - \alpha_2}\right)\sin\phi\cos\phi = \frac{\dot{\mathcal{E}}}{2}\left(\frac{\alpha_3 + \alpha_2}{\alpha_3 - \alpha_2}\right)\sin 2\phi \tag{5.4}$$

for rate of change of azimuthal angle ϕ. The stable orientation requires $\dot{\phi} = 0$, which occurs for $\dot{\mathcal{E}} = 0$ (the trival case of no extension) and for $\phi = 0$, $\phi = \pi/2$. The stability conditions depend on the sign and magnitude of the viscosity coefficients. For α_2 negative and $|\alpha_2| \gg |\alpha_3|$, $\left(\frac{\alpha_3+\alpha_2}{\alpha_3-\alpha_2}\right) < 0$ and it follows that the $\phi = 0$ solution is stable. The $\phi = \pi/2$ solution is unstable with respect to the flow, and any thermally-activated director fluctuations will cause perturbation of $\vec{n}$ and reorientation away from $\phi = \pi/2$ and towards $\phi = 0$. Thus the azimuthal angle of the director will lie along the extension axis.

The polar angle for stable director orientation follows from the y-component of the torque balance equation whose solution, using $\dot{\phi} = 0$, is

$$\dot{\theta} = \frac{1}{(\alpha_3-\alpha_2)}\left[-\frac{(\alpha_3+\alpha_2)}{2}\dot{\mathcal{E}} - \frac{\chi_a B_0^2}{\mu_0}\right]\sin\theta\cos\theta \tag{5.5}$$

Though both α_2 and α_3 are negative, the factor $(\alpha_3 - \alpha_2)$ will be positive and is written from this point as $|\alpha_3 - \alpha_2|$ to indicate this. The stability condition satisfying $\dot{\theta} = 0$ depends on the relative strengths of the two terms in square brackets in Eq. (5.5), arising from the competing hydrodynamic and magnetic torques. If $\dot{\mathcal{E}} < \dot{\mathcal{E}}_c$, where

$$\dot{\mathcal{E}}_c = \frac{2\chi_a B_0^2}{\mu_0|\alpha_3+\alpha_2|}, \tag{5.6}$$

then the right hand side of Eq. (5.5) is negative and $\theta = 0$ is the stable solution. The magnetic orienting term dominates and the director is oriented along $\vec{B}_0$. If instead $\dot{\mathcal{E}} > \dot{\mathcal{E}}_c$, then the extension term is greater than the magnetic orienting term and the director is stable at $\theta = \pi/2$; that is, the molecular long axis is oriented in the plane of the flow and along the extension axis. The theory applied to this geometry, for increasing rate of extension, predicts a sudden transition in director orientation at $\dot{\mathcal{E}} = \dot{\mathcal{E}}_c$.

Equation 5.5 also leads to a description of the director dynamics, via

$$\frac{d\theta}{\sin\theta\cos\theta} = \frac{1}{|\alpha_3-\alpha_2|}\left[\frac{|\alpha_3+\alpha_2|}{2}\dot{\mathcal{E}} - \frac{\chi_a B_0^2}{\mu_0}\right] dt$$

which on integration gives

$$\tan\theta = \exp\left(\frac{1}{|\alpha_3-\alpha_2|}\left[\frac{|\alpha_3+\alpha_2|}{2}\dot{\mathcal{E}} - \frac{\chi_a B_0^2}{\mu_0}\right] t\right). \tag{5.7}$$

This tells us the predicted time evolution of the director in arriving at its final orientation state under competing magnetic and hydrodynamic torques. The time evolution of the LCP in planar extension is tested here in two types of experiments: first, spectra were obtained at timed intervals during combined magnetic field- and flow-induced reorientation, at some value of $\dot{\mathcal{E}}$ and starting from the time extension is just applied. These are referred to here as "start-up" experiments. Secondly, for $\dot{\mathcal{E}} = 0$ the director whose orientation has been perturbed away from $\vec{B}_0$, will regain the magnetically aligned state according to

$$\tan\theta = \exp\left(-\frac{\chi_a B_0^2}{\mu_0|\alpha_3 - \alpha_2|}t\right). \tag{5.8}$$

This is precisely the dynamic Fréedericksz transition. In the second class of experiments we apply an extension $\dot{\mathcal{E}} > \dot{\mathcal{E}}_c$ for a period of time sufficient that θ is aligned by the flow, and then remove it, tracking the director orientation from the time of removal of flow-induced reorientation by collecting spectra at timed intervals. Since the large, static magnetic field is always present in the rheo-NMR experiments, we consider the magnetic orienting term as tending to restore the system to its quiescent, magnetically aligned state and we refer to these as "relaxation" experiments. These tests are to be distinguished from the experiments in which spectra are collected at a given extension or shear rate, after steady state has been reached or a set time has elapsed.

5.5.2 Results: nematic LCP in four roll mill

In the four roll mill the extension rates are calculated directly from the rate of mechanical driving of the rollers, via $\dot{\mathcal{E}} = 2\pi f_r a/d$, where a is the roller radius, f_r the mechanical driving frequency and d the distance from the stagnation point to the roller edge, with reference to Fig. 2.6(a). For this cell $\dot{\mathcal{E}} = 7.033\, f_r$.

The spectra for the 20% concentration sample as a function of extension rate $\dot{\mathcal{E}}$ are

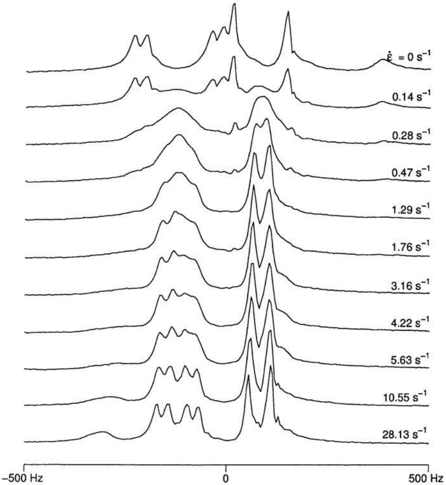

Figure 5.8: ^{2}H NMR spectra for 20% PBLG under different rates of extension. The spectra exhibit four distinct doublets from the two deuterated solvents, as explained in the text, and display a collapse followed by reappearance of the doublets with increasing $\dot{\mathcal{E}}$. The spectral width in the figure is 1000 Hz.

shown in figure 5.8, with $\dot{\mathcal{E}}$ indicated to the right of each spectrum. Several distinguishable doublets can be seen in the spectra. The spectral features are assigned to the deuterated solvent reporter molecules as follows. The doublet of highest intensity, upfield of the resonance frequency (towards positive offset frequency, to the right), corresponds to the eight equivalent deuterons on the dioxane. The very wide, weak doublet of ~ 1 kHz at 20% concentration, and the two higher intensity doublets of similar splittings, all centred downfield of the resonance frequency, correspond to deuterons on the nitrobenzene molecule. The deuterons of nitrobenzene-d_5 are not equivalent as their chemical shift depends on their proximity to the nitro group on the ring.

With increasing rate of extension, the doublet splittings in figure 5.8 first collapse and then increase again, to roughly one-half their zero extension values. This is characteristic of a director orientation along the extension axis for extension rates exceeding the critical extension rate $\dot{\mathcal{E}}_c$, compared to the quiescent state orientation along B_0. From the collapse of the splittings in the spectra, $\dot{\mathcal{E}}_c$ is estimated to be 0.28 s^{-1} for 20% PBLG.

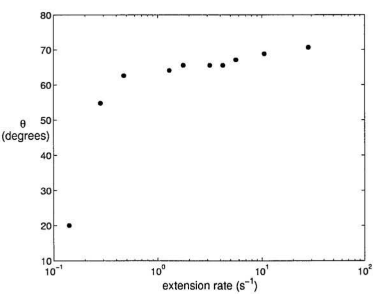

Figure 5.9: Director orientation θ of 20% PBLG under extension in the four roll mill, plotted as a function of $\dot{\mathcal{E}}$. The critical extension rate $\dot{\mathcal{E}}_c$ is estimated to be between 0.14 and 0.28 s^{-1}.

The quadrupolar splitting $\Delta\nu$ of the dioxane doublet was measured for each spectrum, and from each splitting the orientation angle was calculated. The method by which θ is obtained from $\Delta\nu$ is described in section 5.5.4 below. In figure 5.9 the orientation angle is plotted as a function of extension rate for the 20% PBLG. From the disappearance of the larger doublet splitting and appearance of the smaller one characteristic of flow-alignment, $\dot{\mathcal{E}}_c$ may be estimated to be between 0.14 and 0.28 s^{-1}.

After this set of experiments the 20% PBLG sample was diluted a small amount with the deuterated solvent mixture, in order to increase the volume to completely fill the four roll mill and exclude any air from the cell. The new concentration was estimated to be 17%, and another series of extension experiments were carried out on the diluted sample. Figure 5.10 shows the spectra of the 17% PBLG. The spectra are qualitatively very similar to those for the 20% concentration, with the quadrupolar splittings for the 17% concentration sample less well-resolved since the degree of orientation is reduced and the order parameter is smaller.

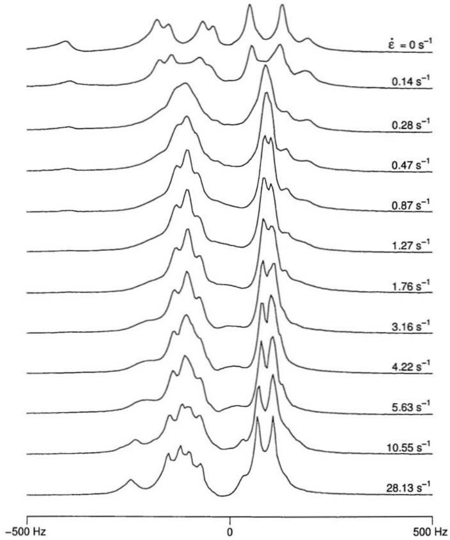

Figure 5.10: ^{2}H NMR spectra for PBLG at 17% concentration in the two deuterated solvents. The spectral width in the figure is 1 kHz. At this lower concentration the quadrupolar splittings in the spectra are smaller than those observed in the 20% sample. Again the splittings decrease to zero and then reappear with increasing rate of extension, as the director becomes oriented along the extension axis for $\dot{\mathcal{E}} > \dot{\mathcal{E}}_c$.

The orientation angle was calculated from the quadrupolar splittings of the dioxane doublet for the 17% PBLG, and is plotted versus rate of extension in figure 5.11. From the extension experiments with the 17% sample, $\dot{\mathcal{E}}$ may be estimated to again be between 0.14 and 0.28 s^{-1}. While the magnitude of the splittings is different in the two samples, indicating increased chain flexibility in the less concentrated solution, the critical extension rate does not appear to be significantly different. This implies that the viscosity is quite similar in the two samples. It should be noted that these early extension experiments covered a broad range of $\dot{\mathcal{E}}$, and it is possible that the actual $\dot{\mathcal{E}}_c$ for the two concentrations shown here is significantly different. Further extension rate dependence experiments were undertaken, on a smaller, $(2\ \text{mm})^2$ zone around the stagnation point.

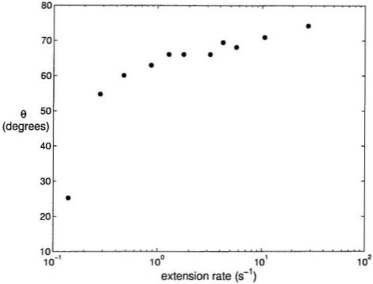

Figure 5.11: Director orientation θ for 17% PBLG under extension in the four roll mill, plotted versus $\dot{\mathcal{E}}$. The data indicates a critical extension rate between 0.14 and 0.28 s^{-1}.

A relaxation experiment was also carried out on the 17% sample to follow the reorientation of the director from the flow-aligned to the magnetically-aligned state in the four roll mill. Spectra collected at a series of times following removal of extension at $\dot{\mathcal{E}} = 4.2\,\mathrm{s}^{-1}$ were analyzed to obtain the splittings of each of the three well-resolved doublets (the dioxane and the two inner nitrobenzene doublets) as a function of time. The splittings were then converted to average angle of director orientation, and the data fit to the relation for the dynamic Fréedericksz transition, Eq. (5.8). Figure 5.12 shows the results. The fits yield

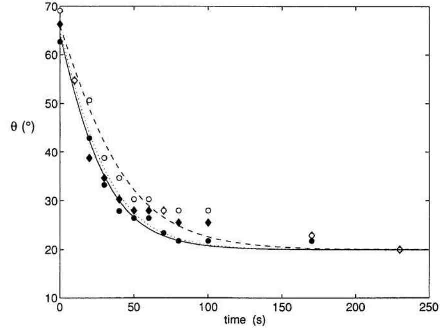

Figure 5.12: Results for relaxation following extension at $\dot{\mathcal{E}} = 4.2\ \mathrm{s}^{-1}$, with both deuterated solvents reporting on the time-dependent LCP reorientation. Filled circles and open circles are the data obtained from the splittings corresponding to the two well-resolved nitrobenzene doublets, with the lines of best fit to Eq. 5.8 indicated by solid and dashed lines, respectively. The diamond symbols refer to the data from the dioxane doublet, with the dotted line indicating the fit. The data point at 230 s is the same for all three data sets.

$\chi_a B_0^2/\mu_0|\alpha_3 - \alpha_2| = 0.039\,\mathrm{s}^{-1} \pm 8\%$ (indicated by the solid line in Fig. 5.12) for the dioxane doublet, and $0.036\,\mathrm{s}^{-1} \pm 7\%$, $0.0402\,\mathrm{s}^{-1} \pm 4\%$ for the inner and outer nitrobenzene doublets, respectively. The relaxation results show that the three inequivalent solvent deuterons on the two different reporter molecules report very similarly on the liquid crystal polymer dynamics. Taking the average from the three fits, $\chi_a B_0^2/\mu_0|\alpha_3 - \alpha_2| = 0.039\ \mathrm{s}^{-1} \pm 7\%$, and $|\alpha_3 - \alpha_2|/\chi_a = (100 \pm 7) \times 10^7$ Pa·s.

Since there did not appear to be extra information gained from keeping both solvents deuterated, all subsequent experiments were carried out on samples prepared with the same solvent configuration, but with only the dioxane solvent deuterated to yield an uncomplicated, higher resolution spectrum and focus on the one resulting doublet.

The extension experiments were taken up again on a new sample, PBLG of 277K molecular weight, prepared at 20% w/w in a 52/48 w/w mixture of dioxane-d_8 and nitrobenzene. Each spectrum was acquired during extension at the designated rate $\dot{\mathcal{E}}$, one minute after start-up. The sample was allowed to relax to the magnetically aligned, single-crystal state between experiments, and this was verified in each case by acquiring a rapid spectrum. The spectra at different extension rates for a $(2\ \mathrm{mm})^2$ square region are shown in figure 5.13.

The single splitting of the quiescent $\dot{\mathcal{E}} = 0$ spectrum in Fig. 5.13 is characteristic of ordered phases and indicates a magnetically-aligned monodomain. The motionally narrowed, Lorentzian lines are characteristic of liquids. From the doublet splittings in the spectra, The angle θ of director orientation was derived from the doublet splittings in the spectra and is shown plotted versus extension rate in figure 5.14. The critical applied extension rate cannot be determined exactly, and more experiments at extension rates near the critical extension rate would have been beneficial; however $\dot{\mathcal{E}}_c$ appears to be just above $0.17\ \mathrm{s}^{-1}$ in this set of experiments. Some reorientation is barely evident at $\dot{\mathcal{E}} = 0.17\ \mathrm{s}^{-1}$ from the slight growth in intensity at the centre of the spectrum arising from isotropic

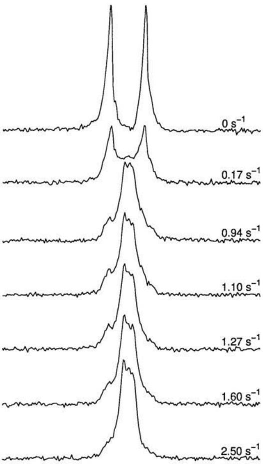

Figure 5.13: ^{2}H NMR spectra of PBLG as a function of rate of extension in the fourroll mill. The width of each spectrum here is 1 kHz. The maximum splitting, exhibited in the zero extension spectrum, is 136.7 Hz.

contributions. This value for the critical extension rate is not significantly different from the $\dot{\mathcal{E}}_c$ of just under 0.28 s^{-1} observed in the earlier experiments. The main difference in the experiments is the spatial extent of the zone reported on: the 2 mm square region centred at the stagnation point for the spectra of Fig. 5.13 compared to 4 mm square region for

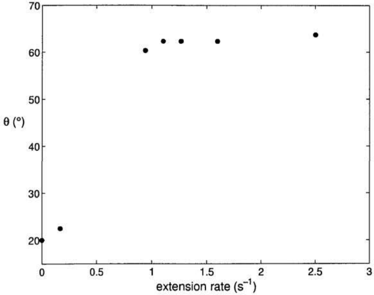

Figure 5.14: Director orientation θ of liquid crystal polymer under extension in the four roll mill, plotted as a function of $\dot{\mathcal{E}}$. The critical extension rate $\dot{\mathcal{E}}$ probably just exceeds 0.17 s^{-1}.

the results presented in Figs. 5.8 and 5.10. For the larger region (with four times the area), one might expect that much of the sample contributing to the NMR signal resides further from the stagnation point, where a fluid element experiences shorter residence times in the extensional strain field. In the smaller region one expects a larger proportion of the polymer chains to faithfully report on the stagnation flow, experience longer residence times and hence undergo flow-alignment at smaller $\dot{\mathcal{E}}_c$. In these experiments the smaller region did not exhibit a lower $\dot{\mathcal{E}}_c$.

5.5.3 Flow characterization: NMR velocimetry in extensional flow

Using the dynamic NMR microscopy technique, flow visualization experiments were performed to characterize the velocity field in the four roll mill. For Newtonian fluids in this cell the velocity gradient via NMR velocimetry has been found, reproducibly, to be linear across the stagnation region. The flow image resulting for $\dot{\mathcal{E}} = 1.13\ \mathrm{s}^{-1}$ is shown in figure 5.15. A contour map calculated from the NMR velocimetry image is also shown. The spacing of the contours is proportional to the gradient in the velocity. The contour

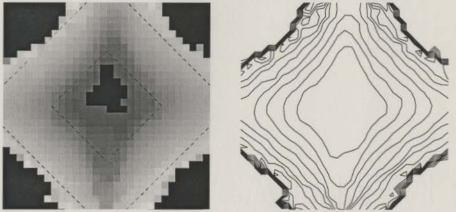

Figure 5.15: Velocity field of 20% PBLG around the stagnation point in the four roll mill, obtained via NMR velocimetry. The extension rate for this experiment is $\dot{\mathcal{E}} = 1.13\ \mathrm{s}^{-1}$. *At left*: speed map calculated from images aquired in two orthogonal directions in the plane of extension in the apparatus, at resolution of 0.156 μm per pixel. The region of interest at the centre of the four roll mill is shown here, 30 × 30 pixels corresponding to $(4.7\ \mathrm{mm})^2$. The zero-intensity corners correspond to the rollers where no fluid is located. Highest intensity in white indicates the highest speeds near the roller edges, while very low speeds are apparent in the centre. *At right*: contour map calculated from the speed map, showing lines of equal velocity magnitude. The spacing of the contours reveals non-ideal features of the flow field of the liquid crystal polymer in this rheometric cell: the sharp rise in velocity gradient close to the roller surfaces, and the reduced velocity gradient in a small region around the stagnation point. The selected region for the spectroscopy experiments was oriented at 45° in the plane with respect to the velocity image shown here. Dashed lines are superimposed on the image to indicate the $(2\ \mathrm{mm})^2$ and $(4\ \mathrm{mm})^2$ regions.

map shows that the velocity gradient rises sharply close the the roller surfaces, that the outer part of the stagnation region has a linear velocity gradient and nearly hyperbolic streamlines, and that in a small region around the stagnation point the velocity gradient is reduced. The selected region for the spectroscopy experiments was oriented at 45° in the plane with respect to the velocity image shown here. The $(4\ \mathrm{mm})^2$ region will encompass most of the region with constant velocity gradient in addition to the diamond-shaped central region with lower velocity gradient, while the (2 mm)^2 region will contain mostly fluid with reduced velocity gradient.

The nominal values of $\dot{\mathcal{E}}$ calculated according to the geometry and shown with the extension rate dependence spectra are the maximum extension rates expected in the four roll mill, for the idealized two-dimensional hyperbolic flow. The NMR velocimetry data

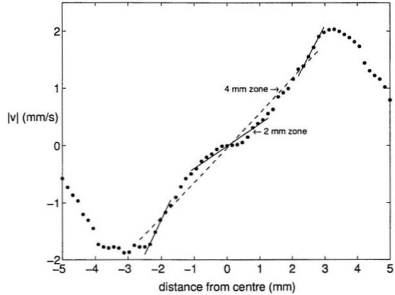

Figure 5.16: One-dimensional velocity profile along the extension axis in the four roll mill. The data corresponds to the middle row of the full NMR velocimetry image whose central region is shown in Fig. 5.15, for which the applied extension rate was 1.13 s^{-1}. The solid line near the centre is the velocity gradient or slope averaged over the data points corresponding to the 2 mm region, from which the average local $\dot{\mathcal{E}}$ is calculated to be 0.39 s^{-1}. The dashed line indicates the slope over the 4 mm region, where $\dot{\mathcal{E}} = 0.6$ s^{-1}. Also shown are straight line fits to the regions where the PBLG solution just emerges from between the rollers, where the calculated $\dot{\mathcal{E}}$ is 1.1 s^{-1}, much truer to the applied rate of extension.

for the polymer liquid crystal shown in Fig. 5.15 indicates that close to the stagnation point the true flow field varies significantly from the idealized two-dimensional hyperbolic flow, particularly in the central region where the actual extension rate is much reduced and the nominal extension rates will be larger than the actual local $\dot{\mathcal{E}}$.

Figure 5.16 shows the velocity profile obtained along the extension axis, for the $\dot{\mathcal{E}} = 1.13\ \mathrm{s}^{-1}$ data of Fig. 5.15. Across the $(4\ \mathrm{mm})^2$ zone the average velocity gradient is seen to be $0.6\ \mathrm{s}^{-1}$ or approximately one-half the applied extension rate, while the average $\dot{\mathcal{E}}$ across the (2 mm) region is $0.4\ \mathrm{s}^{-1}$, one-third of the nominal extension rate. With this evidence it is concluded that the actual critical extension rate is one-third of the value of $\sim 0.20\ \mathrm{s}^{-1}$ obtained (on average) from the three sets of extension rate experiments, or $\dot{\mathcal{E}}_\mathrm{c} \sim 0.07\ \mathrm{s}^{-1}$. From Eq. 5.6, the predicted critical extension rate is $\dot{\mathcal{E}}_\mathrm{c} = 2\chi_\mathrm{a} B_0^2/(\mu_0|\alpha_3 + \alpha_2|)$. The extension results give $|\alpha_2 + \alpha_3|/\chi_\mathrm{a} \simeq 110 \times 10^7$ Pa·s for PBLG at 20% in solution.

The average strain rates derived above from the velocity profile are an improvement, however they do not capture the local variation in the velocity gradient. An important parameter in determining the net effect of deformation is the total strain over the deformation history: $\mathcal{E} = \int \dot{\mathcal{E}}\, dt = \dot{\mathcal{E}}\, t_\mathrm{res}$, where t_res is the residence time of a fluid element in the flow. Clearly the total extensional strain in practice will not match predictions based on the assumption of linear velocity gradient and hyperbolic streamlines everywhere in the stagnation region. This can be addressed, at least in part, by considering the residence time along the extension axis in the following simplified approach. The residence time is calculated by assuming that the length of time a fluid element resides at position p of the velocity profile along the extension axis (that is, in any pixel along this axis in the NMR velocity image) is equivalent to the time to travel a distance of one pixel width, or roughly $t_\mathrm{res} = 0.156\ \mathrm{mm}/|\vec{v}_\mathrm{p}|$ where $|\vec{v}_\mathrm{p}|$ is the fluid speed at p. This analysis ignores the orientation of the flow, and closer to the stagnation point a fluid element will traverse the "pixel" at some angle, but the magnitude and not the direction of $\vec{v}$ is important so that the error in the distance traversed is no greater than a factor of $\sqrt{2}$.

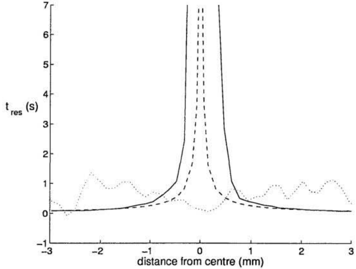

Figure 5.17: Profile of the actual residence time experienced by the liquid crystal polymers along the extension axis in the stagnation region of the four roll mill, shown by the black solid line. The calculation is approximate, and based on the velocity profile data. The dashed line is the ideal profile, for linear velocity gradient throughout the stagnation region. The local velocity gradient calculated from the velocities in the profile is shown by the dotted line.

The residence time calculated in this way is shown in figure 5.17, plotted as the solid line. The ideal situation for linear velocity gradient across the gap is shown by the dashed line. The residence time diverges at the stagnation point where the velocity is zero. The result shows that the actual residence time is long over a wider region than for the ideal case, specifically over approximately 0.5 mm to either side of the centre where the strain dominates. The actual local velocity gradient calculated for each point, using

$$\dot{\mathcal{E}}_{\mathrm{p}} = \frac{\Delta v}{\Delta d} = \frac{|\vec{v}_{\mathrm{p}+1}| - |\vec{v}_{\mathrm{p}-1}|}{2 \times 0.156 \text{ mm}},$$

is also shown in figure 5.17, as the dotted line. Interestingly, in spite of the much suppressed velocity gradient near the stagnation point, the total strain $\mathcal{E} = \sum_p \dot{\mathcal{E}}_{\mathrm{p}} t_{\mathrm{res}}(p)$ over this path is not very different from the ideal case because of the slower flow and the enhancement in the residence time in the real situation. The other significant point is that the total strain along the extension axis is not very different for the 4 mm and 2 mm square selected regions; both contain this zone of long residence time which dominates the flow history over this path.

5.5.4 Orientation angle obtained from the quadrupolar splittings

The quadrupolar splitting written in equation 2.4 is a function of the orientation angle and the order parameter:

$$\Delta\nu = k\, P_2(\cos\theta) S_{zz}\,.$$

In principle the angle may be established from the splitting $\Delta\nu$ in a straightforward way, by assuming the maximum splitting observed corresponds to the magnetically-aligned state and hence to zero degrees. This assumption turns out to make the analysis of the data very difficult, since $P_2(\cos\theta)$ is extremely sensitive to small changes in θ for angles near zero, so that a small change in the observed splitting is magnified in the change in angle. The orientations very near the magnetically aligned state are important here since much of the predicted time-dependent behaviour in the model involves logarithmic approach to the final orientation state. This zero-degree assumption is also almost certainly incorrect: the rods have been reported to have some non-zero angle of inclination with the magnetic field, in their fully aligned state [85]. For a 17.5% PBLG (molecular weight 310K) solution in dichloromethane, Orwoll and Vold [99] found that only approximately 87% of the molecular long axes were within 20° of the field direction, at field strength 14.1 T.

Hence to obtain θ from $\Delta\nu$ we proceeded in the following way. Assuming the quiescent-state director is aligned at some non-zero angle θ_0 with respect to B_0, then the maximum splitting observed in a given set of experiments corresponds to

$$\Delta\nu_{\mathrm{max}} = k\, P_2(\cos\theta_0) S_{zz}$$

and the splitting observed in any given spectrum in that set is related to $\Delta\nu_{\mathrm{max}}$ by

$$\frac{\Delta\nu}{\Delta\nu_{\mathrm{max}}} = \frac{P_2(\cos\theta)}{P_2(\cos\theta_0)} = \frac{1}{2\,P_2(\cos\theta_0)}\left(3\cos^2\theta - 1\right).$$

The average director orientation θ then follows via

$$\cos\theta = \sqrt{\frac{1}{3}\left(\frac{2\Delta\nu P_2(\cos\theta_0)}{\Delta\nu_{\mathrm{max}}} + 1\right)}.$$

This approach was used for all of the results in this chapter, extracting the director orientation from the observed splittings using $\theta_0 = 20°$ throughout. This value of θ_0 was chosen based on the quality of fits to all of the relaxation data using 20°, 25° and 30°, which were consistently best for 20°. It also helps explain why usually the splitting did not quite reach minus one-half the maximum "zero-degree" splitting in even the most strongly orienting flows. For the $\theta_0 = 20°$ case, a similar degree of alignment with the flow corresponds to $\theta_0 = 70°$ or, in other words, 20° to the velocity direction, for which angle the splitting would be $-0.4\Delta\nu_{\mathrm{max}}$.

5.6 Experiments measuring the Leslie coefficients in shear flows

Two additional rheometric cells, both shearing, were used to gain further insight into the nematodynamics of our model liquid crystal polymer. As in the melt experiments, a concentric cylinder Couette cell was used to produce laminar shear. In this case the long axis of the cell was colinear with the magnetic field direction. The cell has 16.9 mm inner cylinder radius and 0.5 mm gap width, and is directly driven by the drive mechanism so that $\dot{\gamma} = \frac{2\pi r}{\mathrm{gap}} f_r = 212\, f_r$. Non-spatially localized experiments were performed to monitor

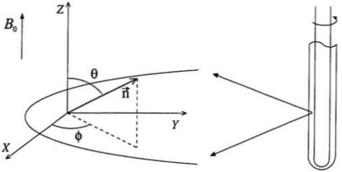

Figure 5.18: Geometry of the director reorientation in the vertical Couette shear field. Velocity X is tangential to the rotating inner cylinder, the velocity gradient Y is radial across the gap, and the third, vorticity axis is in the magnetic field direction. As in figure 5.7, the shaded region represents the sample in the Couette gap.

the shear rate dependence and time evolution of the director orientation for PBLG in the vertical Couette cell. All of the vertical Couette experiments were carried out on 20 wt % PBDG of molecular weight 220K.

5.6.1 Analysis: nematic LCP in vertical Couette cell

The torque balance analysis is extended here to the vertical Couette cell. The vertical Couette cell produces shear in the (X, Y) plane, perpendicular to $\vec{B_0}$. The director in spherical polar coordinates is

$$\vec{n} = [\sin\theta\cos\phi,\ \sin\theta\sin\phi,\ \cos\theta]$$

(see figure 5.18), and the symmetric and anti-symmetric parts of the deformation tensor are

$$\boldsymbol{D} = \frac{1}{2}\begin{bmatrix} 0 & \dot\gamma & 0 \\ \dot\gamma & 0 & 0 \\ 0 & 0 & 0 \end{bmatrix}, \quad \boldsymbol{\omega} = \frac{1}{2}\begin{bmatrix} 0 & \dot\gamma & 0 \\ -\dot\gamma & 0 & 0 \\ 0 & 0 & 0 \end{bmatrix}.$$

This time the z-component of the torque balance equation 5.3 results in:

$$|\alpha_3 - \alpha_2|\,\dot\phi = \dot\gamma\left(\alpha_2\sin^2\phi - \alpha_3\cos^2\phi\right)$$

so that the stability condition for the azimuthal angle, $\dot{\phi} = 0$, occurs for $\dot{\gamma} = 0$ (the trival case of no shear) or for $\tan\phi = \sqrt{\alpha_3/\alpha_2}$. For general shear, then, the rod-like molecules assume an azimuthal orientation in this geometry which depends on the ratio of the Leslie coefficients α_2 and α_3. For $|\alpha_2| \gg |\alpha_3|$ one expects ϕ close to zero.

From the y-component of the torque balance equation,

$$|\alpha_3 - \alpha_2|\,\dot{\theta} = -\alpha_2\,\dot{\gamma}\,\sin\theta\cos\theta\tan\phi - \frac{\chi_a B_0^2}{\mu_0}\sin\theta\cos\theta \tag{5.9}$$

with the x-component yielding the same result. Equation 5.9 can be solved for $\dot{\theta}$,

$$\dot{\theta} = \frac{1}{|\alpha_3 - \alpha_2|}\left(-\alpha_2\sqrt{\frac{\alpha_3}{\alpha_2}}\dot{\gamma} - \frac{\chi_a B_0^2}{\mu_0}\right)\sin\theta\cos\theta$$

and one of two possible scenarios will prevail here:

1. $\dot{\gamma} = 0$:

$$\frac{d\theta}{\sin\theta\cos\theta} = -\frac{\chi_a B_0^2}{\mu_0\,|\alpha_3 - \alpha_2|}dt$$

which on integration gives

$$\tan\theta = \exp\left(-\frac{\chi_a B_0^2}{\mu_0\,|\alpha_3 - \alpha_2|}\,t\right). \tag{5.10}$$

In the absence of shear, for any starting configuration the rods will always evolve to $\theta = 0$ (alignment along the field), given enough time. The rate at which they evolve scales with the diamagnetic susceptibility and the square of the magnetic field strength, and inversely with the magnitude of viscosity coefficient α_2 (assuming $|\alpha_2| \gg |\alpha_3|$), as expected. Note that this is precisely the result obtained earlier for director reorientation in the four roll mill following removal of extension. The Fréedericksz transition result is recovered.

2. $\dot{\gamma} \neq 0$:

$$\dot{\theta} = \frac{1}{2}\frac{\sin 2\theta}{|\alpha_3 - \alpha_2|}\left(\sqrt{|\alpha_2||\alpha_3|}\dot{\gamma} - \frac{\chi_a B_0^2}{\mu_0}\right) \tag{5.11}$$

α_2 and α_3 are both negative based on the flow-alignment observed, $\dot{\gamma}$ is positive, and assuming $\chi_a > 0$ (that is, the rod-like polymer has prolate ellipsoidal shape), $\dot{\theta} = 0$ at $\theta = 0,\ \pi/2$. The stability condition depends on the relative strengths of the shear and magnetically aligning terms. The director dynamics is obtained by integration of equation 5.11:

$$\tan\theta = \exp\left(\frac{1}{|\alpha_3 - \alpha_2|}\left[\sqrt{\alpha_2\,\alpha_3}\dot{\gamma} - \frac{\chi_a B_0^2}{\mu_0}\right] t\right). \tag{5.12}$$

This result predicts that in the vertical Couette cell the director will evolve in time to arrive at its final orientation state, ultimately aligning with the magnetic field ($\theta = 0$) unless the shear rate exceeds the critical value $\dot{\gamma}_c = \dfrac{\chi_a B_0^2}{\sqrt{\alpha_2\,\alpha_3}\,\mu_0}$, in which case the rods will then align with the flow ($\theta = \pi/2$).

5.6.2 Results: nematic LCP in vertical Couette cell

Figure 5.19 displays the spectra collected at timed intervals following removal of strong shear. The spectra display features of the time-dependent reorientation of the nematic director as the state of alignment with $\vec{B_0}$ is restored. The single broad line at zero time indicates that within the 2 s required to acquire the first spectrum, the director has already begun to orient away from the flow-oriented state and along the magnetic field direction. $\Delta\nu$ increases with time as the nematic director is oriented by the magnetic field.

The splittings were determined from the spectra and the orientation angles calculated from the splittings. θ during the relaxation is plotted as a function of time in Fig. 5.20. Also shown in the figure is the fit to the expected relaxation, the Fréedericksz transition described by equation 5.8. The fitted curve describes the data very nicely, and yields $\chi_a B_0^2/\mu_0|\alpha_3 - \alpha_2| = 0.037\ \mathrm{s}^{-1} \pm 2\%$. From this, $|\alpha_3 - \alpha_2|/\chi_a$ is calculated to be $(105 \pm 2) \times 10^7$ Pa·s. Note that this is very close to the value of $(100 \pm 7) \times 10^7$ Pa·s obtained from the dioxane splittings for relaxation of PBLG following extension (see Fig. 5.12), from which we conclude that the behaviour of the polymer nematics in the flow-aligned state and subject to only the magnetic orienting torque, is the same in the two different rheometric cells.

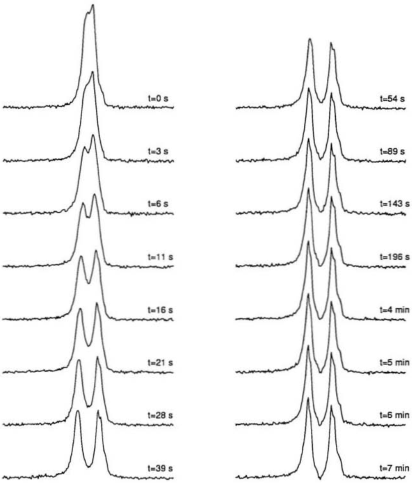

Figure 5.19: ^{2}H NMR spectra for relaxation of liquid crystal polymer following removal of 185.5 s^{-1} shear in the vertical Couette cell. The width of each spectrum is 1 kHz. Within the 2 s required to acquire the first spectrum, the director has begun to relax from its orientation along the flow direction.

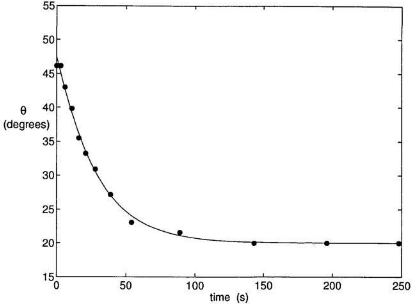

Figure 5.20: Recovery of magnetically aligned state following shear at 185.5 s^{-1} in the vertical Couette cell. The splittings were extracted from the NMR spectra of Fig. 5.19, taking $\Delta\nu_{\max} = 146.5$ Hz to be the magnetically aligned orientation and $\theta_0 = 20$ degrees, and are plotted here as a function of time. The solid line is the fit to the predicted recovery of the magnetically aligned state in the LEP model, given by Eq. 5.8. The fit yields $\chi_a B_0^2/\mu_0|\alpha_3 - \alpha_2| = 0.037\ s^{-1} \pm 2\%$.

The deuterium NMR spectra of the liquid crystal polymer following start of steady shear at $\dot{\gamma} = 0.47\ \mathrm{s}^{-1}$ in the vertical Couette cell are shown in Fig. 5.21. This value of $\dot{\gamma}$ was chosen, after some experimentation, so that the competing magnetic and flow aligning terms are of similar magnitude. For the purpose of observation this was desirable as the sample reached the flow aligning state very slowly, allowing for monitoring of director evolution. The spectra demonstrate that with time the director becomes increasingly aligned along the flow direction, and that following 7 minutes of steady shear the director has not fully aligned with the flow direction.

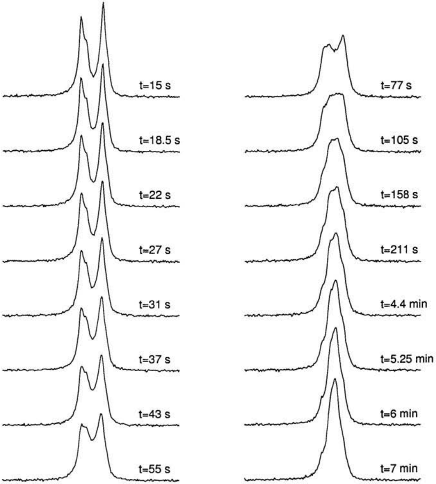

Figure 5.21: Deuterium NMR spectra of liquid crystal polymer following start of steady shear at $\dot{\gamma} = 0.47\ \mathrm{s}^{-1}$ in the vertical Couette cell. The spectral width is 1 kHz, with the corresponding times shown to the right of each spectrum.

Figure 5.22 shows the time dependence of the director orientation with respect to B_0, obtained from the quadrupolar splittings in the spectra of Fig. 5.21. The collection of spectra was automated so that the software could read from a file containing delay times, and step through the list. For the relaxation experiments, $t = 0$ was taken from the time the motor was manually shut off, and start of data collection was synchronized with this. Conversely, the startup experiments required the motor to be turned on in the software, which also begins collection of the spectra, so that the time for the first spectrum could be no less than $t = 15$ s and all times in the delay file are staggered by 15 s.

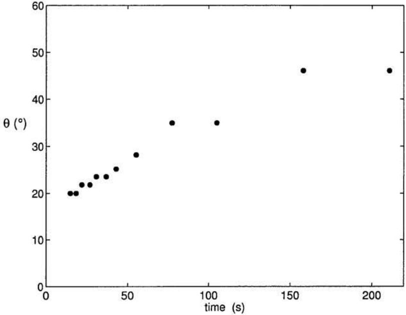

Figure 5.22: Start-up in shear: director orientation as a function of time in $\dot{\gamma} = 0.47\ \mathrm{s}^{-1}$ shear flow in the vertical Couette cell. $t = 0$ corresponds to onset of shearing.

According to Eq. 5.12 the logarithm of $\tan\theta$ is expected to be a linear function of time, with slope $\left[\sqrt{\alpha_2\,\alpha_3}\dot{\gamma} - \frac{\chi_a B_0^2}{\mu_0}\right]/|\alpha_3 - \alpha_2|$. In figure 5.23, $\tan\theta$ is plotted on a logarithmic axis versus time, and does show the linear time-dependence predicted in the Leslie-Ericksen analysis. The fit was carried out over the first ten data points, corresponding to times $t = 0$ to 105 s for which splittings could be determined from a distinct doublet rather than from the linewidth. The positive slope is 0.0082 s^{-1}. Using $\chi_a B_0^2/\mu_0|\alpha_3 - \alpha_2| = 0.037\ \mathrm{s}^{-1}$ from the fit to the relaxation data (Fig. 5.20) for this sample, it is first noted that the flow-aligning term is only very slightly dominant, as expected from the slow nature of the director reorientation. With $\dot{\gamma} = 0.47\ \mathrm{s}^{-1}$, $\sqrt{\alpha_2\,\alpha_3}/|\alpha_3 - \alpha_2|$ is calculated to be 0.096. This result implies that α_2 is 110 times larger in magnitude than α_3, which agrees well with reported observations that α_2 is usually one to two orders of magnitude larger than α_3 for flow-aligning nematics [72].

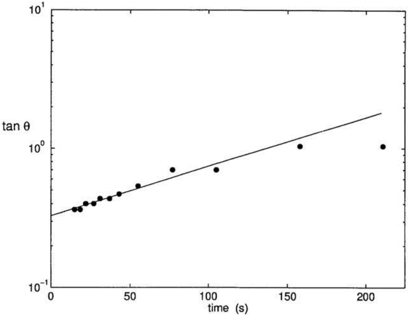

Figure 5.23: Analysis of director orientation as a function of time from onset of $\dot{\gamma} = 0.47\ \mathrm{s}^{-1}$ shear flow in the vertical Couette cell. The linear fit of $ln(\tan\theta)$ vs. t, carried out over the first ten data points corresponding to $t = 0$ to 105 s, has slope 0.0082 s^{-1}. The analysis is discussed in the text.

The shear rate dependence in the vertical Couette cell was also studied with this sample. Because the shear rate experiments were conducted without a priori knowledge of the viscosity coefficients of this PBLG preparation, it was not clear how much time was needed to reach steady state. Furthermore Eq. 5.12 predicts that for shear rates approaching $\dot{\gamma}_c$, the time to reach steady state becomes infinite. Instead, the following protocol was adopted: acquire a spectrum at exactly 60 seconds following onset of shearing, as typically one minute appeared to be sufficient to reach the flow-aligned state; then wait several minutes between experiments to restore the magnetically-aligned, resting state. The spectra are characteristic of a monotonically increasing director orientation angle, with the distinct doublet observed at very high shear rates being indicative of the flow-aligned state for the rod-like polymers.

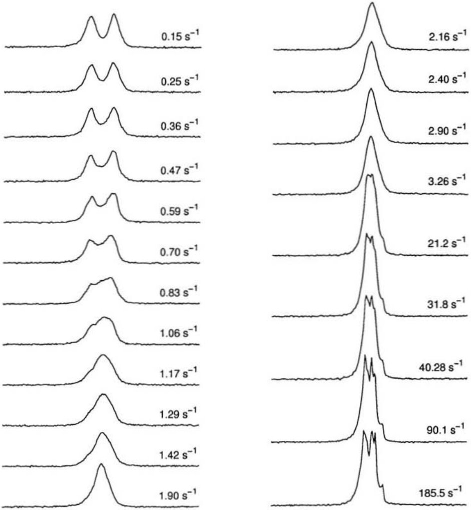

Figure 5.24: Spectra of 20% PBLG at increasing rates of shear in the vertical Couette cell. The spectral width in the displayed spectra is 1 kHz.

Figure 5.25 shows the shear rate dependence of director orientation, obtained from the quadrupolar splittings in the spectra of Fig. 5.24. In this case the logarithm of $\tan\theta$ is predicted to be a linear function of shear rate, with slope $t\sqrt{\alpha_2\,\alpha_3}/|\alpha_3-\alpha_2|$ following Eq. 5.12. In figure 5.26 $\tan\theta$ is plotted on a logarithmic axis versus time. The slope clearly decreases with increasing shear rate. If out-of-plane excursions are not considered, the results in figure 5.25 imply that the viscosity coefficients change as the sample evolves under shear. There is a break in the slope at between $\dot\gamma = 2$ and $5\ \mathrm{s}^{-1}$, and two regions for the viscosity coefficients may be identified, with the following interpretation. For the low shear data the positive slope is 1.39 s, and with fixed $t = 60$ s the slope yields 0.024 for $\sqrt{\alpha_2\,\alpha_3}/|\alpha_3-\alpha_2|$. By this result, $|\alpha_2| \simeq 1800|\alpha_3|$. This ratio is much too large based

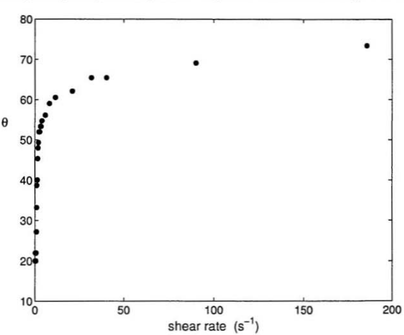

Figure 5.25: Analysis of director orientation as a function of $\dot\gamma$, in shear flow in the vertical Couette cell. The data yields two regions of orientation behaviour, which may be attributed to a change in the viscosity coefficients as the molecules become aligned with the flow, and possible development of texture.

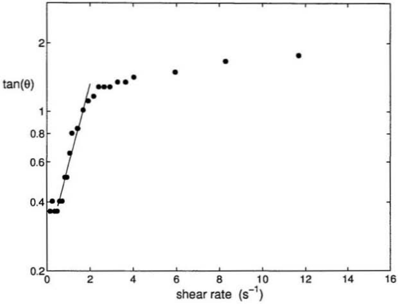

Figure 5.26: The low shear rate fit of $ln(\tan\theta)$ vs. $\dot{\gamma}$ is best shown on this axis. At low shear rates the linear behaviour observed over $\dot{\gamma} = 0.6$ s^{-1} to 1.7 s^{-1} yielded 1.39 s for the fitted slope.

on the information already obtained about α_2 and α_3; the slope is at least a factor of 10 too small. Change in the rotational viscosity affects both magnetic and flow aligning terms, and as a first analysis using $|\alpha_2| \gg |\alpha_3|$, the first term scales with $1/\sqrt{|\alpha_2|}$ while the second term goes as $1/|\alpha_2|$. Hence a decrease in the Leslie viscosity coefficient $|\alpha_2|$ causes both terms to increase, but the flow aligning term increases more slowly and its ability to align the director is reduced relative to the magnetic term. The results suggest that under shear, as the rod-like molecules become increasingly aligned with the flow, the rotational viscosity decreases. The stress delivered to the mesogens by the applied shear decreases, and flow is less able to align them.

The spectra for director reorientation in PBLG at increasing rates of shear in the vertical Couette cell are markedly different from the spectra under extension, indicating quite different processes. The suggestion is that in the planar extension geometry under competing magnetic and hydrodynamic orienting fields, the local director is in one of two states, while under shear in the Couette the local environment of the director is more complex. It is also conceivable that some mesoscale structure develops under shear, so that elastic and other effects not accounted for in the Leslie-Ericksen theory become important and the model no longer applies. In light of the large number of rheological observations which point to development and evolution of microstructure under steady shear [79, 88, 86, 87], it is plausible that the apparent reduction in viscosity results from the appearance of textures, so that director orientation varies spatially in the Couette gap. A polydomain, textured sample would contain local directors of all orientations, and the NMR spectrum would consist of a broadened, isotropic line rather than the doublet characteristic of a monodomain. Some of the spectra at intermediate shear rates do appear to be broadened significantly. Importantly, the spectra at very high rates of shear exhibiting a high degree of alignment with the flow are characteristic of a single crystal state and show no evidence of spatial inhomogeneities in the director orientation.

5.6.3 Analysis: nematic LCP in cone and plate

In the cone and plate geometry the shear plane is defined by the velocity direction X in the tangential direction and the velocity gradient direction Y across the gap. The cone used here makes an angle of 20° with the plate, so that the shear rate is related to the driving frequency by $\dot{\gamma} = 2\pi f_r/\theta_0 = 18 f_r$. The 16 mm diameter cone and plate cell is self-contained and holds 0.26 cm^3 of liquid in the gap.

The geometry of the cone and plate is best treated in spherical polar coordinates, so

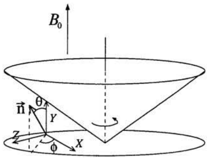

Figure 5.27: Geometry of the director reorientation in the cone and plate shear field. Velocity direction X is tangential to the rotating cone and perpendicular to the magnetic field, the velocity gradient direction Y is vertical across the gap and coincident with the magnetic field, and the third, vorticity axis is in the radial direction. The director magnitude is exaggerated and the shaded region represents the liquid crystal polymer sample. The actual angle between the cone and the plate is 20°.

the director is

$$\vec{n} = [\sin\theta\cos\phi,\ \cos\theta,\ \sin\theta\sin\phi]$$

as shown in Fig. 5.27. We thus obtain the same hydrodynamic description and the same symmetric and anti-symmetric deformation tensors as the vertical Couette cell. The magnetic body force in the field $\vec{B_0} = [0,\ B_0,\ 0]$ is

$$\vec{h} = \left[0,\ \frac{\chi_a B_0^2 \cos\theta}{\mu_0},\ 0\right] .$$

The balance of torques in the Leslie-Ericksen-Parodi model for this geometry has been solved previously by Grabowski *et al.* [24, 95]. The result for stable director orientation is

$$\tan\theta = -\frac{\chi_a B_0^2}{2|\alpha_3|\dot{\gamma}\mu_0} \pm \sqrt{\left(\frac{\chi_a B_0^2}{2\alpha_3\dot{\gamma}\mu_0}\right)^2 + \frac{\alpha_2}{\alpha_3}} . \tag{5.13}$$

Whereas in the vertical Couette shearing geometry the director orientation is a transient phenomenon, evolving until one of $\theta = 0$ or $\theta = \pi/2$ is reached, in the cone and plate geometry competing fields establish a stable director orientation at some angle in the shear (X, Y) plane, for any given shear rate. Applied to cone and plate shear flow, the LEP model predicts director alignment with azimuthal angle $\phi = 0$ and polar angle $\theta = \tan^{-1}(\sqrt{\alpha_2/\alpha_3}) \approx \pi/2$ in the shear plane (see Fig. 5.27), corresponding to director orientation very nearly along the velocity direction. Note that $\vec{B_0}$ lies in the shear plane for the cone and plate, while for the four roll mill and the vertical Couette cell, $\vec{B_0}$ lies perpendicular to the plane of extension or shear.

Turning to the time evolution for zero shear, we get

$$\frac{d\theta}{\sin\theta\cos\theta} = -\frac{\chi_a B_0^2}{\mu_0\,|\alpha_3 - \alpha_2|}dt$$

so that once again the result is

$$\tan\theta = \exp\left(-\frac{\chi_a B_0^2}{\mu_0\,|\alpha_3 - \alpha_2|}t\right) \tag{5.14}$$

for return to the magnetically aligned state.

5.6.4 Results: nematic LCP in cone and plate rheometer

Spectra were obtained at increasing rates of shear in the cone and plate for 20% PBLG of molecular weight 277K. They are shown in Fig. 5.28, with the shear rates indicated beside each spectrum.

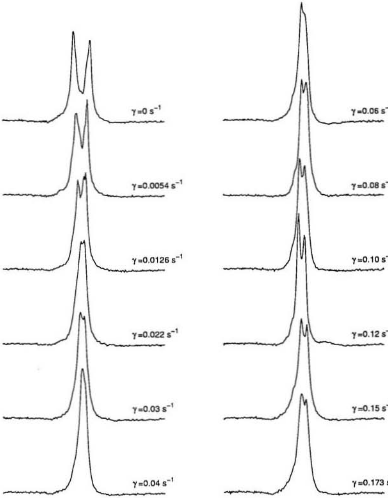

Figure 5.28: Spectra of PBLG acquired under steady shear in the 20° cone and plate. Spectra were acquired at exactly 60 s following start of shear, with 2 s acquisition time in each case. The width of each spectrum is 1 kHz.

At the smallest shear rate accessible, $\dot{\gamma} = 0.1\ \mathrm{s}^{-1}$, the splitting has already begun to decrease, indicating that the director has been perturbed from its equilibrium state by the shear flow. Throughout the shear range accessed, the spectra show no evidence of a tumbling director. Again the quadrupolar splitting $\Delta\nu$ was extracted from each spectrum and converted to the corresponding director orientation angle θ. The shear rate dependence of θ is shown as a function of $\dot{\gamma}$ in Fig. 5.29. The data fall on a curve which is qualitatively very similar to the shear rate dependence curve observed by Grabowski and Schmidt [24] for the nematic side-chain LCP, poly(siloxane), in a cone and plate rheometer. Also shown in figure 5.29 is the fit to the data of the torque-balance prediction for competing shear and magnetic torques in this geometry, according to Eq. 5.13. The fit

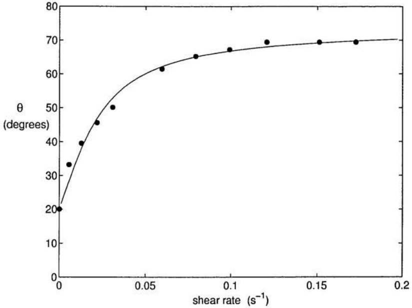

Figure 5.29: Shear rate dependence of average director orientation θ of PBLG in the cone and plate. The splittings were extracted from the NMR spectra and converted to θ as described in section 5.5.4. The solid line is the fit to the data of the predicted behaviour, Eq. 5.13.

yields $\chi_a B_0^2/(2\mu_0|\alpha_3|) = 0.117\pm4\%$ or $|\alpha_3|/\chi_a = (17\pm1)\times10^7$ Pa·s, and $\alpha_2/\alpha_3 = 13.3\pm0.5$.

The dynamics of the director orientation were studied by acquiring spectra during relaxation following strong shearing flow at $\dot{\gamma} = 0.08$ s^{-1} in the cone and plate. The resulting spectra are shown in Fig. 5.30. The NMR data for relaxation following shear in the cone and plate is shown in figure 5.31, with director orientation θ plotted versus time following removal of shear. The solid line is the fit of the dynamic Fréedericksz transition prediction (Eq. 5.8) to the NMR data, and yields $\chi_a B_0^2/\mu_0|\alpha_3 - \alpha_2| = 0.0293 \pm 6\%$ s^{-1}, or $|\alpha_3 - \alpha_2|/\chi_a = (133 \pm 8) \times 10^7$ Pa·s.

5.7 Summary of results for the Leslie-Ericksen viscosity coefficients

The data from 20% PBLG under extension and under shear in the three different rheometric cells can be compared with reference to one common parameter. For this, $|\alpha_3 - \alpha_2|/\chi_a$, expressed in terms of the undetermined χ_a, is appropriate as it was obtained for all three cells under relaxation so that it is independent of the type of deformation and the geometry of the flow field. This parameter is tabulated here for the three different cells.

Relaxation experiment	$\lvert\alpha_3 - \alpha_2\rvert/\chi_a$
four roll mill:	$(100 \pm 7) \times 10^7$ Pa·s
concentric cylinder Couette cell:	$(105 \pm 2) \times 10^7$ Pa·s
cone and plate:	$(133 \pm 8) \times 10^7$ Pa·s

This agreement is quite good, although the result from the cone and plate is not within the estimated uncertainty and this could be explained by some evaporation of solvent in the sample. A slight increase in concentration would be expected to result in an increased viscosity and the relaxation experiment should be sensitive to this. The extension rate experiments yield $|\alpha_2 + \alpha_3|/\chi_a \simeq 110 \times 10^7$ Pa·s, which is in agreement with the values of $|\alpha_3 - \alpha_2|/\chi_a$ so long as $|\alpha_2| \gg |\alpha_3|$. From the shear-rate dependence in the vertical Couette cell, $\sqrt{\alpha_2 \alpha_3}/|\alpha_3 - \alpha_2|$ is calculated to be 0.096, which gives $\alpha_2 \simeq 100\alpha_3$.

The shear rate dependence studies in the cone-and-plate yielded $|\alpha_3|/\chi_a = (17 \pm 1) \times 10^7$ Pa·s, and $\alpha_2/\alpha_3 = 13.3 \pm 0.5$. Taken literally, the shear rate dependence cone and plate data imply that $|\alpha_3 - \alpha_2|/\chi_a \simeq (210 \pm 9) \times 10^7$ Pa·s and $|\alpha_2 + \alpha_3|/\chi_a \simeq (245 \pm 11) \times 10^7$ Pa·s. The shear results are thus not in agreement with the relaxation and extension results.

There are several possible reasons for the discrepancy. Firstly, while PBLG molecules are considered to be "rigid rods" within the general class of liquid crystal polymers, *they still have some flexibility*. It is conceivable that during their reorientation they become bent or twisted, before lengthening out into rods again in the orienting field. Chu *et al.* recently witnessed dynamics which point to a coil-stretch transition in fluorescently-labeled DNA molecules in an elongational flow [97]. In the analysis of the shear-rate dependence results of section 5.6.2, the appearance of texture was tentatively put forth as the cause of broadening in the spectra and the breakdown of the agreement of the NMR data with the Leslie-Ericksen model. Another possible candidate is bending of the semi-flexible linear polymers during the reorientation. Whether linear molecules bent during reorientation are stretched out again, or some convective patterns develop and then decrease in width until the effect is no longer evident in the NMR spectrum, cannot be determined here. These two possible effects cannot be distinguished based on the NMR spectra.

The second reason relates to the existence of a distribution of residence times in the planar extensional flow field. As a crude first approach, a calculation of the residence times based on a simple time-of-flight description of fluid elements along the extension axis has been carried out in Matlab and discussed in section 5.5.3. This is instructive as it tells us that while velocity gradient in the centre of the four roll mill is reduced from what it is expected to be, the resulting residence time is very long and the planar extension around the stagnation point should still dominate the flow history. A natural extension of this work would be to model this distribution for the full two-dimensional case.

Thirdly, the analysis assumes director orientation within the plane $(\vec{v}, \vec{B}_0)$, an assumption which is well-founded from combined NMR and optical microscopy studies [90]. If out-of-plane excursions of the director are important during reorientation then a model in which they are allowed would more accurately capture the dynamics.

The fourth reason is that Frank elasticity is omitted from the Leslie-Ericksen model. The sample is treated as a single crystal so that there are no, or negligible, gradients in the director field. While spatial gradients are negligible under the strongly orienting flow and magnetic fields, there probably are larger spatial gradients where these fields just compensate each other and the stable orientation state is marginal. Under these conditions the elastic torque might be expected to become important. The Larson-Doi polydomain model [94], which does account for elastic torques, might then be more applicable, although in our experiments this condition of marginal orientation state would only apply to intermediate extension or shear rates.

Finally, we know from the geometry of the four roll mill and from our NMR velocimetry experiments that the flow is not homogeneous and that one cannot ignore the previous flow history of the molecules. Incorporation of the entire mixed shear and extensional flow field into the LE model would be extremely complicated and at this point the numerical simulations of Leal *et al.* [21] seem more likely to model successfully the flow history.

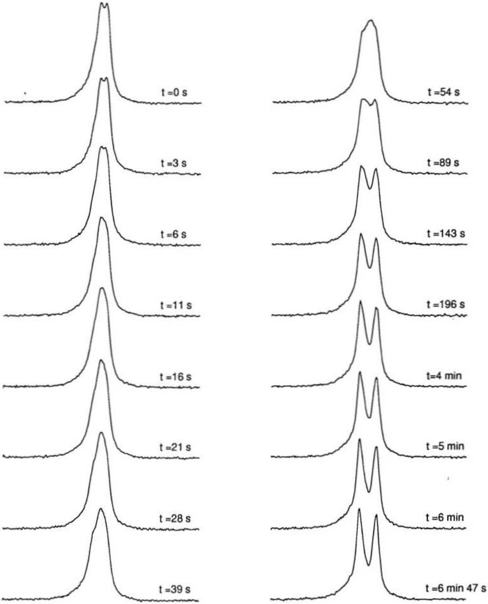

Figure 5.30: Spectra of PBLG acquired during relaxation following steady shear, applied for one minute at $\dot{\gamma} = 0.08\ \mathrm{s}^{-1}$, in the 20° cone and plate. The first spectrum, corresponding to $t = 0$, was acquired immediately upon removal of the shear. The spectral width in all of the spectra is 1 kHz.

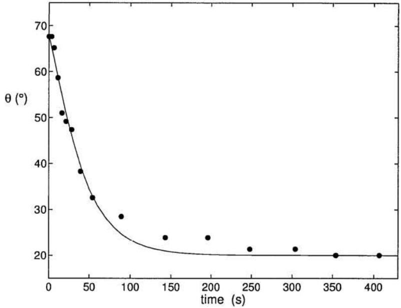

Figure 5.31: Fit of the Fréedericksz transition prediction to the NMR data for relaxation following shear at $\dot{\gamma} = 0.08\ \mathrm{s}^{-1}$ in the 20° cone and plate. The fit yields $0.0293 = \chi_a B_0^2/\mu_0(\alpha_3 - \alpha_2)$, or $(\alpha_3 - \alpha_2)/\chi_a = 133 \times 10^7$ Pa·s.

6 Concluding remarks

A magnetic resonance method for spatial localization, deuterium NMR spectroscopy sensitive to segmental or director alignment, and mechanical rheometry in cells capable of producing large rates of shear or extension in viscoelastic fluids, have been combined to study order and dynamics in entangled polymers and liquid crystal polymers under deformation.

The shear rate-dependence of S_{XX} and S_{YY} elements of the segmental alignment tensor in the polymer melt with the deuterated benzene probe were directly compared to predictions for the segmental alignment tensor in the theory of Doi and Edwards. The agreement between the NMR data and the predictions of the model was very good, and was further improved with the independent alignment approximation removed from the model and with the convected constraint release refinement added to the Doi-Edwards calculations. In particular the orientation angle χ derived from the angle dependence studies was in excellent agreement with the CCR-modified Doi-Edwards model. The angle dependence study also suggested that the deformation in the melt under shear is biaxial, and this result is also in support of the model. Where $\dot{\gamma} \gg 1/\tau_d$ and the convective relaxation mechanism is expected to become important, the S_{XX} NMR data appeared to recommend the refined Doi-Edwards model over the original. It is noted that for the shear rates accessed here the assumption $\dot{\gamma} \ll 1/\tau_R$ probably still holds, and the success of the CCR refinement in modeling the NMR data is most likely because the effects of tube stretching are not apparent here. Fluctuations in the contour length of the polymer chain would become important under yet faster flows, or in melts of higher molar mass at these values of $\dot{\gamma}$, and in this case the model would require further modification to account for these effects. The high shear S_{YY} data exhibited some anomalous behaviour which could not be explored further.

Intriguing ordering effects were obtained with the deuterated oligomer probe in the melt. The oligomer results were not in line with the expected result of highest degree of anisotropy in the direction of the velocity. The results are interpreted bearing in mind that the larger probe molecule involved returns a mesoscopic-length-scale average as opposed to bulk average segment orientation reported by a smaller probe molecule like benzene, and hence may reflect some mesoscale structure. On this basis a smectic-like ordering in the direction of the velocity gradient in the melt under high shear was proposed as a possible explanation for these results.

This work establishes unique methods and analysis using NMR as a sensitive probe of predictions of the Doi-Edwards model. The continuation of this work by another doctoral student, Ryan Cormier, has led to extension of the NMR measurements to S_{ZZ} in a vertical Couette cell, and S_{XY} (equivalent to the shear stress) obtained from a combination of S_{XX} and S_{YY}. The full alignment tensor is thus obtained, and his experiments on a 680K PDMS melt over the entire nonlinear range available are allowing for a robust test of the convected constraint-modified Doi-Edwards model.

The combination of methods has also been applied to liquid crystal polymers subjected to competing magnetic and hydrodynamic torques and analyzed in the framework of the

Leslie-Ericksen model. Planar extension in the four roll mill and shear in a concentric cylinder Couette cell and in a cone-and-plate were used to measure director reorientation in monodomain poly(γ-benzyl-L-glutamate) samples under extension and under shear. The Leslie viscosity coefficients from the extension and shear experiments were compared in section 5.7. The relaxation to the magnetically-aligned state following cessation of strong extension or shear directed perpendicular to the magnetic field is equivalent to the dynamic Fréedericksz transition. Experiments in all three rheometric cells under these conditions yielded values for rotational viscosity (expressed in terms of the undetermined diamagnetic anisotropy χ_a) which are in good agreement. The coefficients yielded by the shear experiments are not in agreement with the extension and the Fréedericksz transition results. Several possible reasons for the discrepancy have been pointed out in chapter 5. The extension experiments also addressed the question of what happens to semi-flexible polymer chains when they encounter long residence times around the stagnation point. From NMR velocimetry data it was determined that the liquid crystal polymer under strong extension modifies the flow field around the stagnation point, so that the polymers experience a velocity gradient which is diminished from the applied $\dot{\mathcal{E}}$, but have longer residence times in the vicinity of the stagnation point. The total strain in this region still dominates the flow history.

In section 5.7 it was pointed out that the NMR spectrum does not afford the ability to distinguish between the possible effects of development of texture and bending of semi-flexible molecules under shear. The issue of shear-induced texture in liquid crystal polymer solutions should be pursued via NMR. One possibility would be to use structurally sensitive probes. This would most likely require isotopic labeling of the liquid crystal polymers themselves. Such samples would be very difficult to obtain. In magnetic resonance studies, experiments which are sensitive to mesoscale structure are diffusion studies. Evidence of anisotropic diffusion via NMR has been demonstrated in thermotropic liquid crystals in the smectic phase [100] and on water molecules in the vicinity of lipid bilayers [101]. In the liquid crystal polymer systems, anisotropic diffusion studies could be carried out at different rates of shear to gain information about spatial structures, their length scale and the time scale for their possible appearance and disappearance. They might also be carried out during director reorientation along $\vec{B}_0$, in the relaxation studies, to investigate the possible existence and disappearance of domain walls.

Bibliography

[1] H.A. Barnes, J.F. Hutton, and K. Walters. *An Introduction to Rheology*. Elsevier, Amsterdam, 1989.

[2] T.G. Mason, A. Dhople, and D. Wirtz. *Macromolecules*, 31:3600, 1998.

[3] J. Xu, A. Palmer, and D. Wirtz. *Macromolecules*, 31:6486, 1998.

[4] T.C. Papanastasiou. *Applied Fluid Mechanics*. Prentice Hall, Englewood Cliffs, New Jersey, 1994.

[5] R.B. Bird and C.F. Curtiss. *Physics Today*, 37:36, January 1984.

[6] M. Doi and S. Edwards. *The Theory of Polymer Dynamics*. Oxford University Press, Oxford, 1986.

[7] R.G. Larson. *Constitutive Equations for Polymer Melts and Solutions*. Butterworths Series in Chemical Engineering, Boston, 1988.

[8] G. Marrucci. *J. Non-Newtonian Fluid Mech.*, 62:279, 1996.

[9] S. Chandrasekhar. *Liquid Crystals, 2nd Ed.* Cambridge University Press, Cambridge, 1992.

[10] J.G. Grote. Design and fabrication of nonlinear optic polymer integrated optic devices. In D.L. Wise, G.E. Wnek, D.J. Trantolo, T.M. Cooper, and J.D. Gresser, editors, *Electrical and Optical Polymer Systems*. Marcel Dekker, Inc., New York, 1998.

[11] M.G. Mogul, D.L. Wise, J.D. Gresser, D.J. Trantolo, and G.E. Wnek. Second harmonic generation and laminar structures in poly(γ-benzyl-L-glutamate) films aligned in electric fields. In D.L. Wise, G.E. Wnek, D.J. Trantolo, T.M. Cooper, and J.D. Gresser, editors, *Electrical and Optical Polymer Systems*. Marcel Dekker, Inc., New York, 1998.

[12] F.M. Leslie. *Quart. J. Appl. Math*, 19:357, 1966.

[13] F.M. Leslie. *Arch. Rat. Mech. Anal.*, 28:265, 1968.

[14] A.I. Nakatani, M.D. Poliks, and E.T. Samulski. NMR investigation of chain deformation in sheared polymer fluids. *Macromolecules*, 23:2686, 1990.

[15] C. P. Slichter. *Principles of Magnetic Resonance*. Springer-Verlag, Heidelberg, 1990.

[16] A. Abragam. *The Principles of Nuclear Magnetism*. Clarendon Press, Oxford, 1961.

[17] K. Blum. *Density Matrix Theory and Applications*. Physics of Atoms and Molecules. Plenum Press, New York, 1981.

[18] M. Mehring. *Principles of High-Resolution NMR in Solids*. Springer-Verlag, Berlin, 2nd edition, 1983.

[19] P.T. Callaghan. *Principles of Nuclear Magnetic Resonance Microscopy*. Oxford University Press, Oxford, 1991.

[20] B. Deloche and E. T. Samulski. *Macromolecules*, 14:575, 1981.

[21] J. Feng and L.G. Leal. *J. Non-Newtonian Fluid Mech.*, 72:187, 1997.

[22] M.M. Britton, P.T. Callaghan, M.L. Kilfoil, R.W. Mair, and K.M. Owens. *App. Magn. Res.*, 15:287, 1998.

[23] P. T. Callaghan and E. T. Samulski. *Macromolecules*, 30:113, 1997.

[24] D.A. Grabowski and C. Schmidt. *Macromolecules*, 27:2632, 1994.

[25] R. Kimmich and D. Hoepfel. *J. Magn. Reson.*, 72:379, 1987.

[26] D. M. Doddrell, W. M. Brooks, J. M. Bulsing, J. Field, M. G. Irving, and H. Baddeley. *J. Magn. Reson.*, 68:367, 1986.

[27] D. M. Doddrell, J. M. Bulsing, G. J. Galloway, W. M. Brooks, J. Field, M. G. Irving, and H. Baddeley. *J. Magn. Reson.*, 70:319, 1986.

[28] P. A. Bottomley, T. B. Foster, and R. D. Darrow. *J. Magn. Reson.*, 59:338, 1984.

[29] J. Frahm, K. D. Merboldt, W. Hänicke, and A. Haase. *J. Magn. Reson.*, 64:81, 1985.

[30] H. Yan, B. Chen, and J. C. Gore. *J. Magn. Reson.*, 75:83, 1987.

[31] H. Yan and J. C. Gore. *J. Magn. Reson.*, 75:427, 1987.

[32] M. S. Silver, R. I. Joseph, and D. I. Hoult. *J. Magn. Reson.*, 59:347, 1984.

[33] H. Geen, S. Wimperis, and R. Freeman. *J. Magn. Reson.*, 85:620, 1989.

[34] H. Post, D. Ratzel, and P. Brunner. West German Patent, No. P3209263.6, March 1982.

[35] W. P. Aue, S. Müller, T. A. Cross, and J. Seelig. *J. Magn. Reson.*, 56:350, 1984.

[36] J. Frahm and W. Hänicke. *J. Magn. Reson.*, 60:320, 1984.

[37] W. H. Press, B. P. Flannery, S. A. Teukolsky, and W. T. Vetterling. *Numerical Recipes: The Art of Scientific Computing.* Cambridge University Press, Cambridge, 1986.

[38] S. Müller, W. P. Aue, and J. Seelig. *J. Magn. Reson.*, 65:332, 1985.

[39] P.G. de Gennes. *J. Chem. Phys.*, 55:572, 1971.

[40] S.F. Edwards. *Proc. Phys. Soc.*, 92:9, 1967.

[41] M. Doi and S.F. Edwards. *J. Chem. Soc. Faraday Trans. II*, 74:1789, 1978.

[42] M. Doi and S.F. Edwards. *J. Chem. Soc. Faraday Trans. II*, 74:1802, 1978.

[43] M. Doi and S.F. Edwards. *J. Chem. Soc. Faraday Trans. II*, 74:1818, 1978.

[44] M. Doi and S.F. Edwards. *J. Chem. Soc. Faraday Trans. II*, 75:38, 1979.

[45] S.F. Edwards. *Polymer*, 9:140, 1977.

[46] L.R.G. Treloar. *The Physics of Rubber Elasticity, 3rd Ed.* Clarendon Press, Oxford, 1975.

[47] The MathWorks, Inc. *Matlab Version 5.3 (R11.1)*, 1999.

[48] P.T. Callaghan, M.L. Kilfoil, and E.T. Samulski. *Phys. Rev. Lett.*, 81:4524, 1998.

[49] G.A. Alvarez, A.S. Lodge, and H.-H. Cantow. *Rheol. Acta*, 24:368, 1985.

[50] H.A. Barnes and K. Walters. *Rheol. Acta*, 24:323, 1985.

[51] M. Bercea, C. Peiti, B. Dimionescu, and P. Navard. *Macromolecules*, 26:7095, 1993.

[52] H. Janeschitz-Kriegl. *Polymer Melt Rheology and Flow Birefringence*. Springer-Verlag, New York, 1983.

[53] E.T. Samulski. *Polymer*, 26:177, 1985.

[54] M Sekiya and M. Doi. *J. Phys. Soc. Jpn.*, 52:3672, 1982.

[55] R. Muller and C. Picot. 56:107, 1992.

[56] R. Muller, J.J. Pesce, and C. Picot. *Macromolecules*, 26:4356, 1993.

[57] H. Toriumi, B. Deloche, J. Herz, and E. T. Samulski. *Macromolecules*, 18:304, 1985.

[58] S. Pahl, G. Fleischer, F. Fujara, and B. Geil. *Macromolecules*, 30:1414, 1997.

[59] R.J. Plano, C.R. Safinya, E.B. Sirota, and L.J. Wenzel. *Rev. Sci. Instrum.*, 64:1309, 1993.

[60] D.W. Mead, R.G. Larson, and M. Doi. *Macromolecules*, 31:7895, 1998.

[61] G. Marrucci and G. Ianniruberto. *J. Non-Newtonian Fluid Mech.*, 82:275, 1999.

[62] E.F. Brown and W.R. Burghardt. *J. Rheol.*, 40:37, 1996.

[63] J.D. Ferry. *Viscoelastic Properties of Polymers, 3rd Ed.* John Wiley & Sons, Inc., New York, 1980.

[64] Z. Luz, R. Poupko, and E.T. Samulski. *J. Chem. Phys.*, 74:5825, 1981.

[65] M. Doi. *J. Polym. Sci. Lett.*, 19:265, 1981.

[66] M. Rubinstein and S. Panyukov. *Macromolecules*, 30:8036, 1997.

[67] G. Ianniruberto and G. Marrucci. *J. Non-Newtonian Fluid Mech.*, 79:225, 1998.

[68] G. Marrucci, F. Greco, and G. Ianniruberto. *Current Opinion in Colloid & Interface Science*, 4:283, 1999.

[69] G. Ianniruberto and G. Marrucci. *J. Non-Newtonian Fluid Mech.*, 65:241, 1996.

[70] J.F. Ericksen. *Arch. Rat. Mech. Anal.*, 9:371, 1962.

[71] W.R. Burghardt. *Macromol. Chem. Phys.*, 199:471, 1998.

[72] P.G. de Gennes. *The Physics of Liquid Crystals.* Oxford University Press, Oxford, UK, 1993.

[73] E. T. Samulski. *Science*, 234:1424, 1986.

[74] O. Parodi. *J. Physique*, 31:581, 1970.

[75] C. Robinson. *Trans. Faraday Soc.*, 52:571, 1956.

[76] P. Doty, J.H. Bradbury, and A.M. Holtzer. *J. A. C. S.*, 78:947, 1956.

[77] M. Panar and W.D. Phillips. *J. Am. Chem. Soc.*, 90:3880, 1968.

[78] R.W. Duke and D.B. Dupré. *Macromolecules*, 7:374, 1974.

[79] G. Kiss and R.S. Porter. *J. Polym. Sci., Polym. Symp.*, 65:193, 1978.

[80] K.R. Amundsen. Electric and magnetic field effects on polymeric systems exhibiting long-range orientational order. In D.L. Wise, G.E. Wnek, D.J. Trantolo, T.M. Cooper, and J.D. Gresser, editors, *Electrical and Optical Polymer Systems.* Marcel Dekker, Inc., New York, 1998.

[81] H. Block. *Ploy(γ-benzyl-L-glutamate) and Other Glutamic Acid Containing Polymers.* Gordon and Breach Science Publishers, New York, 1983.

[82] M.D. Poliks, Y.W. Park, and E.T. Samulski. *Mol. Cryst. Liq. Cryst.*, 153:321, 1987.

[83] Z. Bu, P.S. Russo, D.L. Tipton, and I.I. Negulescu. *Macromolecules*, 27:6871, 1994.

[84] V. Freédericksz and V. Tsvetkov. *Phy. Z. Soviet Union*, 6:490, 1934.

[85] N.S. Murthy, E.T. Samulski, and J.R. Knox. *Macromolecules*, 19:941, 1986.

[86] V.M. Ugaz, D.K. Cinander, and W.R. Burghardt. *J. Rheol.*, 42:379, 1998.

[87] L. Noirez and A. Lapp. *Phys. Rev. E*, 53:6115, 1996.

[88] N.X. Yan, M.M. Labes, S.G. Baek, and J.J. Magda. *Macromolecules*, 27:2784, 1994.

[89] N. Schwenk, C. Boeffel, and H.W. Spiess. *Liq. Crystals*, 12:735, 1992.

[90] N. Schwenk and H.W. Spiess. *J. Phys. II (Fr.)*, 3:865, 1993.

[91] E. Guyon, R. Meyer, and J. Salan. *Mol. Cryst. Liq. Cryst.*, 54:261, 1979.

[92] F. Lonberg, S. Fraden, A.J. Hurd, and R.B. Meyer. *Phys. Rev. Lett.*, 52:1903, 1984.

[93] M. Simões, A.J. Palangana, A.A. Arroteia, and P.R. Vilarim. *Phys. Rev. E*, 6304:1707, 2001.

[94] R.G. Larson and M.Doi. *J. Rheol.*, 35:539, 1991.

[95] H. Siebert, D.A. Grabowski, and C. Schmidt. *Rheol. Acta*, 36:618, 1997.

[96] P.T. Callaghan. *Rep. Prog. Phys.*, 62:599, 1999.

[97] T.T. Perkins, D.E. Smith, and S. Chu. *Science*, 276:2016, 1997.

[98] R.W. Duke, D.B. DuPré, and E.T. Samulski. *Macromolecules*, 19:941, 1986.

[99] R.D. Orwell and R.L. Vold. *J. Am. Chem. Soc.*, 93:5335, 1971.

[100] R. Blinc, M. Burgar, M. Luzar, J. Pirs, I. Zupancic, and S. Zumer. *Phys. Rev. Lett.*, 33:1192, 1974.

[101] P. T. Callaghan, M. A. LeGros, and D. N. Pindar. *J. Chem. Phys.*, 79:6372, 1983.

Acknowledgements

Many people have helped me during my doctoral program and their efforts are sincerely appreciated. I especially wish to thank: Professor Paul Callaghan who has such enthusiasm and fine appreciation for physics, and who is always challenging and encouraging. It has been a great pleasure working with him. Dr. Michael Morrow whose experimental expertise, insight and support I have benefitted from greatly. And Dr. John deBruyn of my doctoral committee for many interesting discussions, and for his guidance and advice throughout my time at Memorial. I also thank Dr. John Whitehead for helpful discussions as a member of my doctoral committee.

I have had the pleasure of working with many talented colleagues, fellow graduate students and post doctoral fellows, and I hope we cross paths again many times. I also want to thank the secretaries for help with administrative matters, the computer support and mechanical workshop staff for their technical expertise and patience, and all members of the Memorial University and Massey University physics departments for making both places such enjoyable environments in which to study.

I am grateful to my friends and family, especially Gerry and Donna, Fraser, and my parents, for all their continued support.